

A study of star formation in nearby starburst galaxies

A thesis
submitted for the degree of
DOCTOR OF PHILOSOPHY

In
The Faculty of Science
Bangalore University, Bangalore

By
Swara Ravindranath



Indian Institute of Astrophysics
Bangalore - 560034
India

June 1999

Declaration

I hereby declare that this thesis is the result of the investigations carried out by me at the Indian Institute of Astrophysics, Bangalore under the supervision of Prof. T. P. Prabhu. This thesis has not been submitted for the award of any degree, diploma, associateship, fellowship, etc. of any university or institute.

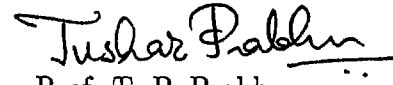
Swara.R.

Swara Ravindranath
(Candidate)

Bangalore 560034
1999

Certificate

This is to certify that the thesis entitled "A study of star formation in nearby starburst galaxies" submitted to the Bangalore University by Ms. Swara Ravindranath for the award of the degree of Doctor of Philosophy in the faculty of Science, is based on the results of the investigations carried out by her under my supervision and guidance, at the Indian Institute of Astrophysics. This thesis has not been submitted for the award of any degree, diploma, associateship, fellowship, etc. of any university or institute.


Prof. T. P. Prabhu
(Supervisor)

Bangalore 560034
1999

Acknowledgements

It is a pleasure to thank my thesis supervisor, Prof. T. P. Prabhu for all the encouragement and guidance throughout the course of this work. I thank Prof. Ramanath Cowsik, Director of the Indian Institute of Astrophysics, for providing all the facilities required for pursuing this study.

I would like to thank the Chairman of the Physics department, Bangalore University, Prof. A.R. Hanumanthappa, the former Chairmen and the faculty of the Bangalore University for their help during registration, conduction of the Pre-PhD examination and other formalities.

I would like to thank the Board of Graduate Studies (IIA), for the encouragement and support to attend the Summer school on “Starbursts – triggers, nature and evolution” held at Les Houches, France, in 1996, and the conference on “The evolution of galaxies on cosmological timescales” held at Tenerife, Spain, in 1998. I was greatly benefitted from both these trips which gave me an opportunity to interact with senior researchers in the field and discuss my work and related topics.

I am grateful to all the observing staff, electronics and computer personnel, and staff of the mechanical and electrical sections at the Vainu Bappu Observatory, Kavalur, for their help and co-operation during observations with the 2.34-m telescope. Their enthusiasm and good nature have always made the stay at VBO very enjoyable.

I thank the IIA library staff, and the Librarian Ms. A. Vageswari for providing all the assistance required in making the books and journals available for reference. I thank the computer personnel, Mr. A.V. Ananth, Mr. J.S. Nathan, and Mr. K.N. Kutty for all the help offered when I encountered problems with the computers. I also thank the staff of the binding section, Mr. Kanagaraj and Mr. Thyagaraja for preparing the bound copies of the thesis.

I thank Dr. L.C. Ho for providing the nuclear spectrum of NGC 972 prior to publication and for the interesting discussions. I thank Dr. Y.D. Mayya for providing the NIR observations of NGC 972, and the useful discussions we had while writing up the paper. I would like to thank Dr. C. Leitherer for clearing my doubts regarding the Starburst99 models.

I would like to thank all my colleagues at IIA for their help, encouragement and valuable discussions.

Abstract

A starburst galaxy is defined as a galaxy whose luminosity is dominated by an intense episode of star formation, and is characterized by a very high star formation rate which cannot be sustained over its lifetime. To explain their very high Far-Infrared luminosities (10^{10} to $10^{12} L_{\odot}$), star formation rates of $\sim 10\text{--}100 M_{\odot} \text{ yr}^{-1}$ would be required and at such a high rate the molecular gas in the galaxy would be exhausted in less than 1/10 of the Hubble time. Hence the starburst phase must be a transient phenomena in galaxies. Since gas is efficiently converted to stars in starbursts, and massive stars return most of the processed material back into the ISM through stellar winds and supernovae in a short time, they are mainly responsible for the metal-enrichment of the Universe. Thus, starbursts being the most extreme cases of massive star formation, they are very important for understanding the formation and chemodynamical evolution of galaxies.

Starburst phenomenon has been found to be very dominant at high redshifts (which implies large lookback times) and most of the ground-based large telescopes and space-telescopes have observational programmes devoted to the study of star-forming galaxies at intermediate and high redshifts. These observations essentially sample the integrated properties of the star-forming regions. In order to understand and interpret the integrated spectra, colors and luminosities in terms of the IMF, SFR and ages of the ionizing clusters, it is very important to study the nearby starbursts in detail.

The work presented in this thesis aims at studying the physical properties of the nebular gas and the stellar populations in a sample of nearby starburst galaxies. The observational technique includes broad-band BVR and narrow-band H_{α} imaging, and optical-NIR spectroscopy. All the observations required for the present study were obtained using the 2.34-m Vainu Bappu Telescope at the Vainu Bappu Observatory in Kavalur, India. The distribution of ionized gas in the galaxies were analysed based on the H_{α} emission morphology and the distribution of dust was traced using the B/R color maps. The star formation rates for the star-forming regions have been derived from the H_{α} luminosities. The ages of the young stellar populations have been determined based on the evolutionary

synthesis models.

A general introduction to the field is presented in Chapter 1 and the observations and reduction techniques are described in Chapter 2. A case study of the massive star formation in the IR bright galaxy NGC 972 is presented in Chapter 3. The H-alpha image shows active star formation in the circumnuclear regions and the disk of this galaxy while the color map reveals the complex dust distribution. The results from aperture photometry are presented for the individual HII regions and using evolutionary synthesis models we estimate that the current episode of star formation is less than 6.5 Myr old. Based on the H_α fluxes we derive and the spectroscopic emission line ratios, we confirm the starburst nature of the nucleus of NGC 972. Nuclear starbursts and circumnuclear star formation are usually triggered by galaxy-galaxy interactions or are associated with strong bars. However, NGC 972 is an isolated galaxy and the optical images do not show any evidence for a bar. This prompted an investigation of the NIR morphology of this galaxy, since the NIR images sample the underlying stellar populations (low-mass stars and their evolved stages) better. The K -band image did show a weak bar-like structure within the circumnuclear ring of star-forming regions. From the information available in the literature, we found that the molecular gas content in this galaxy is very high. Based on the evidence that the nucleus of NGC 972 is undergoing a starburst with strength comparable to that in the prototype starburst M82, the presence of active circumnuclear star formation and large molecular content, we propose that the activity in NGC 972 is likely to have been triggered by a merger with a gas-rich companion.

A study of the statistical properties of HII regions in the galaxy NGC 1365 was carried out and the results are discussed in Chapter 4. We obtain a power law slope of $\alpha = -2.29 \pm 0.11$ for the HII region luminosity function which is consistent with that found for galaxies of similar Hubble type. We find that the size distribution can be well-fitted by an exponential law. From the steep slopes of the HII region luminosity function and the small characteristic diameters derived from the size distribution for NGC 1365 and other early-type galaxies in the literature, it appears that some dynamical phenomena are responsible for inhibiting the formation of “supergiant” HII regions in these galaxies. The ultraviolet

photons from massive stars can ionize a finite volume of gas and this region of completely ionized gas is referred to as the “Strömgren sphere”. Such an HII region is ionization-bounded and the H_α luminosity scales as the cube of the Strömgren radius. A simple linear least square fit to the luminosity versus radius of the HII regions in logarithmic units for NGC 1365, yields a slope close to 3 at low luminosities, while the slope tends to get steeper at higher luminosities. The sizes of the luminous HII regions which contain more number of massive stars are limited by the amount of material available for ionizing by UV photons. Thus it appears that the low luminosity HII regions are ionization bounded while the high luminosity HII regions are density bounded.

Optical–NIR spectroscopy of a sample of starburst nuclei were carried out with an aim to study the physical properties of the photoionized gas and to estimate the ages of the young stellar populations present in these nuclei (Chapter 5). We determined the electron densities, ionization parameters, and the nebular oxygen abundances using diagnostic emission line ratios. We then compared the properties of starburst nuclei with that of HII nuclei and disk HII regions. We find that the electron densities are high and the excitation levels are also slightly higher in starbursts. The low-ionization lines are enhanced in starbursts compared to disk HII regions and we find that the photoionization models which include the effects of dust can account for the enhancement of these lines in the spectra. For a few nuclei where we could determine the radiation softness parameter, we find that the temperatures of ionizing stars decrease with increasing metallicities and is less than 40,000 K. This would place the upper mass limit of the IMF in these regions at $M_u \leq 25 M_\odot$. We have derived the star formation rates from the H_α luminosities. The presence of evolved massive stars in the red supergiant (RSG) phase was identified through the large equivalent widths of the Ca II triplet lines in the NIR. From the observed H_α luminosity, H_α equivalent widths and Ca II triplet line equivalent widths, it appears that the nuclear starbursts have a composite population consisting of young massive stars which are less than 3 Myr old, co-existing with an evolved RSG population. We use diagnostic diagrams involving Ca II absorption line and H_α emission line equivalent widths to infer ages of 6–8 Myr for the evolved population.

Contents

1	Introduction	5
1.1	Star formation in galaxies	5
1.1.1	Star formation rates and efficiencies	7
1.1.2	The initial mass function	9
1.2	Starburst galaxies and their properties	10
1.2.1	Spectral energy distributions of starbursts	11
1.2.2	Molecular gas content and gas depletion timescales	13
1.2.3	Blue compact dwarf galaxies and Luminous IR galaxies	14
1.3	Triggering of starburst activity	16
1.3.1	Role of galaxy interactions and mergers	16
1.3.2	Role of bars in mass transfer	18
1.4	The Starburst–AGN connection	19
1.5	Starbursts and galaxy evolution	21
1.6	Thesis outline	22
1.6.1	Motivation	23
1.6.2	Methodology	23
2	The sample selection, observations and data reduction	31
2.1	Introduction	31
2.2	Sample selection	31
2.3	Observational details	34

2.3.1	<i>BVR</i> and H α imaging	35
2.3.2	Optical and near–infrared spectroscopy	40
2.4	Reduction of imaging data	44
2.4.1	Basic steps in reduction	44
2.4.2	Aperture photometry	44
2.4.3	Photometric calibration	45
2.5	Reduction of spectroscopic data	47
2.5.1	Extraction of spectrum	47
2.5.2	Wavelength calibration	47
2.5.3	Flux calibration	48
2.5.4	Estimation of continuum	49
2.5.5	Measurement of equivalent widths and fluxes	49
2.6	Distribution of dust and ionized gas in galaxies	50
2.7	Summary	59
3	Massive star formation in the Infra-red bright galaxy NGC 972	62
3.1	Introduction	62
3.2	Observations and Reductions	65
3.2.1	Optical <i>BVR</i> and H α imaging	65
3.2.2	Near Infrared <i>JHK</i> imaging	67
3.3	Optical–NIR morphology of NGC 972	70
3.3.1	Spiral structure and dust distribution	70
3.3.2	Distribution of the ionized gas	72
3.4	Discussion	76
3.4.1	Revision of the morphological type of NGC 972	76
3.4.2	Star formation history	78
3.4.3	Emission line diagnostics and the nature of activity	83
3.4.4	Evidence for starburst activity and possible triggering mechanisms	87
3.5	Conclusions	90

4	Properties of the HII regions in NGC 1365 – The luminosity function and size distribution	96
4.1	Introduction	96
4.2	The HII region catalogue for NGC 1365	99
4.2.1	Observations and reductions	99
4.2.2	Measurement of H_α fluxes and HII region diameters	100
4.3	Properties of the HII regions	103
4.3.1	Absolute magnitudes and H_α equivalent widths	103
4.3.2	The HII region luminosity function	105
4.3.3	Size distribution of HII regions	106
4.4	Discussion	108
4.5	Conclusions	110
5	The nebular properties and stellar populations of starburst nuclei	119
5.1	Introduction	119
5.2	Sample selection, observations and reductions	122
5.3	Emission line spectra – electron densities, ionization parameter, internal reddening and oxygen abundances	126
5.3.1	Electron densities	129
5.3.2	Ionization parameter	130
5.3.3	Oxygen abundances	131
5.3.4	Temperatures of ionizing stars	132
5.3.5	Internal reddening in nuclear regions	133
5.4	Stellar populations in the nuclear regions – the implications for star formation scenarios	135
5.4.1	H_α luminosities and equivalent widths	136
5.4.2	Ca T absorption equivalent widths	140
5.5	Properties of the photoionized gas in starburst regions	141
5.5.1	A comparison of starburst nuclei and HII nuclei	141

5.5.2	Diagnostic emission line ratios - the enhancement of low ionization lines	142
5.5.3	The nature of the ionizing stars	145
5.6	Star formation properties in nuclear regions	145
5.7	Age determination of starbursts using Ca II triplet line equivalent widths .	146
5.8	Conclusion	151
6	Summary and prospects	154
6.1	Overview of results	154
6.1.1	Properties of HII regions	154
6.1.2	Effects of dust in star-forming regions	155
6.1.3	Star formation rates in starbursts	156
6.1.4	Stellar populations in starbursts and their ages	156
6.1.5	Triggers of star formation	157
6.2	Suggestions for future study	157
6.2.1	IMF in starburst regions	157
6.2.2	Determination of SFRs	158
6.2.3	Triggers of nuclear activity	159
	List of publications	161

Chapter 1

Introduction

1.1 Star formation in galaxies

Galaxies are the largest assembly of stars and form the building blocks of the large-scale structure in the Universe. The formation of galaxies and the origin of their diverse morphological types are not yet well-understood and are among the most challenging problems in cosmology. The Hubble classification of galaxies based on their morphologies, from ellipticals to spirals, is essentially a decreasing sequence of the spheroid-to-disk ratio. However, the Hubble sequence is also characterized by an increase in the gas and dust content, ionized gas and star formation activity as we proceed from elliptical galaxies to early-type spirals (Sa) and then to late-type spirals (Sc). Elliptical galaxies, SO galaxies, and bulges of spirals constitute the gas-poor spheroidal systems which are composed of old, evolved stars and low-mass stars. These systems are dominated by random motions of the stars, giving them their spheroidal appearances, in contrast to the disk systems which are flattened and rotation-supported. The spiral disks are made up of gas and dust, and among the spiral galaxies the gaseous disk becomes increasingly dominant compared to the bulge component for the late-type galaxies.

The properties of galaxies along the Hubble sequence can be understood based on their star formation histories as suggested by Sandage (1986), Kennicutt (1983), and Gallagher *et al.* (1984). Accordingly, the formation of elliptical galaxies would have been a rapid

process, in which almost all the gas was converted to stars efficiently, on a short timescale of $\approx 10^8$ years. The spiral galaxies would have formed their bulges similarly in a rapid collapse, but with lesser efficiency, whereby the remaining gas settled into the disk. The late-type spirals would have formed bulges with very less efficiency and have retained a large amount of the gas in them. Since these have remained as gas-rich systems, they show active global star formation in the present epoch. Thus, the Hubble sequence is a reflection of the birthrate of stars in galaxies, which is the ratio of the present rate of star formation to the average past star formation rate. The formation and evolution of galaxies may be influenced by a number of factors, like the initial conditions in the protogalactic cloud, the environmental effects, merger rates and feedback processes from star formation through winds and stellar explosions. Both observations and theory indicate that star formation holds the key to understanding galaxy formation.

Stars are born within dense clouds of molecular gas which are mostly distributed in the spiral arms of galaxies. The new born stars make themselves visible after they have dispersed a part of the placental cloud material, and have photoionized the gas in their vicinity. Star formation is also initiated in the nuclear and circumnuclear regions of a galaxy (within 1–2 kiloparsecs from the center) if considerable amount of molecular gas is accumulated in these regions. Recently, there has been evidence for star formation activity even in elliptical galaxies which were believed to be gas-poor systems. The molecular gas in these galaxies are probably acquired through galaxy–galaxy interactions.

Stars with masses greater than ten solar masses emit copious amounts of ultraviolet radiation which is capable of ionizing the surrounding hydrogen gas. The resulting photoionized nebulae are referred to as “HII regions” and owing to their high luminosities, they serve to identify regions of massive star formation in our Galaxy as well as in external galaxies. The photoionizations in the HII regions are followed by recombinations, whereby the electrons are recaptured by the hydrogen ions. The H_α line of the Balmer series is the strongest recombination line in the optical region. Thus the presence of strong H_α emission is an indication of massive star formation and the H_α luminosity is a measure of the number of ionizing stars embedded within the HII regions.

Massive star formation in galaxies is also revealed by their high UV continuum luminosity which is nearly flat in the wavelength range 1250–2500 Å, the Lyman and Balmer breaks in the UV–optical continuum, and emission features like the Lyman- α (1216 Å) line. The other tracers of massive star formation include the optical emission line spectra, high far–infrared fluxes and high gas content. We discuss each of these tracers in detail in the sections that follow. We emphasize on the H α recombination line, since a major part of the work presented in this thesis relies on the use of this line as a tracer of massive star formation.

Star formation in galaxies proceeds on various scales and spans a large range in mass and luminosity. Normal HII regions like the Orion nebula have H α luminosities of $\approx 10^{37}$ erg s $^{-1}$ and are ionized by a single star or a few massive stars. More luminous HII regions such as W49 and NGC 3603 in our Galaxy, have H α luminosities of $\approx 10^{39}$ erg s $^{-1}$ and are ionized by small OB associations or clusters of early–type stars. Starburst regions or “supergiant” HII regions have H α luminosities in the range 10^{40} to 10^{42} erg s $^{-1}$, and must be photoionized by large OB associations containing more than 1000 massive stars. Thus, starbursts are the sites where most of the massive stars are formed in the Universe. The nearest example of a starburst region is the 30 Doradus region in the Large Magellanic Cloud.

Star formation in galaxies can be described by the star formation rate (SFR), the star formation efficiency (SFE) and the initial mass function (IMF).

1.1.1 Star formation rates and efficiencies

The SFR is the rate at which the molecular gas gets transformed to stars, and depends on the gas density. The total SFR for a normal galaxy like the Milky Way is about 6 M $_{\odot}$ yr $^{-1}$. The diagnostics of star formation rate include integrated colors and spectra, ultraviolet continuum fluxes, emission line fluxes and far infrared luminosities (Kennicutt 1992, 1998). The utility of integrated colors and spectra towards an estimation of SFR, based on evolutionary synthesis modelling is derived from the idea that the spectrum of

a galaxy of any Hubble type is dominated by the ratio of early to late-type stars. By matching the colors and spectra with that from the models, one can estimate the ratio of the current SFR to average past SFR. In regions of active star-formation, the SFR directly scales with the UV luminosity and hence the UV continuum in the range of wavelengths from 1300–2500 Å can be used to derive SFRs (Buat *et al* 1989; Leitherer & Heckman 1995). Since the nebular recombination lines effectively re-emit the ionizing luminosities of massive stars shortward of the Lyman limit, they provide a direct and sensitive measure of the SFRs. The relation between the recombination line luminosities and the SFR are computed based on model stellar clusters with some initial mass function, whose fluxes are integrated shortward of the Lyman limit to obtain the ionizing luminosities (Kennicutt 1983, Gallagher *et al* 1984, Kennicutt *et al* 1994). This method essentially provides only the information on SFRs for the high mass end ($M \geq 10M_{\odot}$). The most extensively used tracer has been the H_{α} recombination line, but with the developments in near-infrared observations, Br γ measurements are also becoming available to derive SFRs. The absorption cross section of the dust in star-forming regions is strongly peaked in the UV, and hence dust absorbs a significant fraction of the bolometric luminosity of a galaxy, which is then re-emitted in the infrared at ≈ 10 – $300 \mu\text{m}$. This FIR emission also serves as an SFR diagnostic (Kennicutt, 1998). The star forming properties of galaxies are strongly correlated with the nature of the host galaxy and Kennicutt (1983) show that the SFR per unit luminosity is a strongly increasing function of the Hubble type, increasing from close to zero in E/S0 galaxies, to several solar masses per year for Sc-Irr galaxies.

The efficiency of star formation is defined as the fraction of the molecular gas mass that is transformed into stars. SFE for normal galaxies ranges from ≈ 1 – 10% . The star formation efficiencies are measured using L_{IR}/L_{CO} , which is the ratio of the luminosity of young, massive stars presumed to power the far-infrared luminosity to the CO ($J=1-0$) luminosity that measures the mass of molecular gas. This ratio gives the conversion rate of molecular gas to stars and its inverse gives the lifetime for the process. On the average, a star forming spiral galaxy converts 5% of its interstellar gas to stars every 0.1 Gyr, and hence the average gas depletion timescale is ~ 2 – 2.5 Gyr.

1.1.2 The initial mass function

The interpretation of the star formation properties of a galaxy depend crucially on the stellar mass distribution or the initial mass function (IMF). The IMF is a distribution function that describes the number of stars formed per unit time in a fixed volume, per unit mass interval or logarithmic mass interval. Salpeter (1955) made the first systematic measurements of the IMF in the solar neighbourhood, and found that it could be well-approximated by a power-law of the form;

$$f(m)dm = Am^{-\gamma} \quad (1.1)$$

with, $\gamma = 2.35$. This function is usually normalized to unity when it is integrated over the entire stellar mass spectrum between the upper and lower mass limits, thereby making it a probability distribution. Thus, the IMF is characterized by the mass limits and the slope. However, the mass limits are very difficult to determine and remain uncertain as yet. In the very young clusters, the luminosity is dominated by high mass stars and this causes the low mass stars to be undersampled in any statistical study. On the contrary, in the case of older clusters (beyond a few Myr), the information about high mass stars is lost, due to the fact that massive stars evolve much faster and have lifetimes of this order. The low mass limits considered in most of the works on IMF lie in the range $0.07\text{--}0.1 M_{\odot}$, and the upper mass cutoffs are usually around $30\text{--}120 M_{\odot}$. Much has been debated about the universality of the Salpeter IMF with slope $\gamma = 2.35$ (Scalo, 1986). From the theoretical understanding of star formation, it is natural to expect the IMF to depend on various factors related to the initial conditions of the cloud from which the stars are forming, like the cloud temperature, metallicities and so on. Most of the data available as of now, for our Galaxy and a few nearby galaxies, are consistent with a global Salpeter IMF (Scalo 1998, Elmegreen, 1999). However, there is evidence for a radically different IMF in the case of starbursts and infrared luminous galaxies. Rieke *et al* (1980, 1993) have shown that enormous masses in young stars, would be required to explain the ionizing luminosities in these regions, if one uses a Salpeter IMF. An IMF which is biased towards high mass stars, or a “top-heavy” IMF as it is referred to, seems to offer better

agreement with the observations. In such cases, the low mass limit lies at about $3 M_{\odot}$ without much change in the high mass limit and the slope. More observations involving a large sample of starburst regions and measurements that are really sensitive to the IMF, would be required to confirm the possibility of a different IMF in the case of starbursts which form the extreme cases of massive star formation.

1.2 Starburst galaxies and their properties

A starburst galaxy is defined as a galaxy whose luminosity is dominated by an intense episode of star formation, and is characterized by a very high star formation rate which cannot be sustained over its lifetime. The idea of starbursts was first invoked in order to explain the very high infrared luminosities $\approx 10^{10}$ to $10^{12} L_{\odot}$, found in many galaxies (Rieke *et al*, 1980). The idea that intense bursts of massive star formation can be triggered during galaxy interactions was first suggested by Larson & Tinsley (1978), to explain the blue colors of interacting and peculiar galaxies. The term “Starburst” was coined by Weedman *et al* (1981) to describe the nucleus of NGC 7714, which showed extreme blue color and strong, narrow emission lines. They could explain satisfactorily the properties of this nucleus at all wavelengths by invoking an intense burst of massive star formation.

Star-forming regions have large amounts of dust associated with them, and the Far Infrared (FIR) emission is mainly due to the thermal emission from dust that is heated by the radiation from young, massive stars. Starburst galaxies emit a major part of their luminosity in the FIR wavelengths. The emitting region is less than ≈ 1 to 2 kiloparsec in size, while the FIR output is 10–1000 times that from a normal, quiescent galaxy like the Milky Way. To explain such high luminosities, star formation rates of ~ 10 – $100 M_{\odot} \text{ yr}^{-1}$ would be required, and at such a high rate the molecular gas in the galaxy would get exhausted in less than 1/10 of the Hubble time. Thus the starburst phase must be a transient phenomenon in galaxies.

Most samples of starburst nuclei have been identified from the Markarian catalogue, based on their ultraviolet excess (Balzano, 1983) and from the IRAS survey based on

their high FIR luminosities (Neugebauer *et al*, 1984). Ever since the class of starburst galaxies was established, this phenomenon has become one of the most active area of research mainly because, apart from being the most extreme case of massive star formation starbursts are also important for understanding the formation and chemodynamical evolution of galaxies. The rapid advance in this feild is summarized in the review articles on starbursts by Jog (1995) and Moorwood (1996).

1.2.1 Spectral energy distributions of starbursts

The spectral energy distributions (SEDs) of galaxies provide information on the various stellar populations and physical processes which contribute to their bolometric luminosities. In starburst galaxies, the SEDs recieve a major contribution from the massive star population at all wavelengths.

The continuum emission

The radio emission from starburst galaxies is mainly due to the free-free emission from the photoionized gas and the synchrotron radiation produced as a result of the interaction of electrons with the magnetic feilds in supernova remnants. The radio spectrum is typically a power-law of index ~ 0.7 (Rodriguez-Pascual *et al*, 1993). Starburst galaxies are distinguished by a prominent Far-Infrared (FIR) peak at around $60\text{--}100\mu\text{m}$ which is due to the thermal emission from dust heated mainly by hot massive stars. The typical temperature that can be attributed to this emission is ~ 45 K. However, the peak is much broader than what is expected for a single blackbody, since there are different components in the emission, arising from different sources, like — cold dust associated with molecular clouds, dust heated by the interstellar radiation field, and the dust in HII regions which is heated by the ionizing as well as non-ionizing UV photons. In normal galaxies most of the FIR radiation is emitted by cooler dust, beyond $100\mu\text{m}$ and the entire FIR emission is only a small fraction of the total bolometric luminosity. Galaxies which host an AGN have an additional component at $25\mu\text{m}$ band due to much hotter dust. Since dust gets

heated to different degrees in normal galaxies, starbursts and AGNs, their emissions peak at different FIR bands. Thus, the $60\mu\text{m}$ peak luminosities and warm $F_{60\mu\text{m}}/F_{100\mu\text{m}}$ colors serve as a good indicator of starburst activity. Also, Devereux (1989) suggests that O and B stars are the underlying energy sources that power the $10\mu\text{m}$ luminosity in a majority of spiral galaxies which are associated with high ($\geq 6 \times 10^8 L_{\odot}$) central $10\mu\text{m}$ luminosities.

Stellar evolutionary models predict that stars with masses in the range 20–60 M_{\odot} evolve to red supergiants after about 4 Myr. Thus, young star-forming regions which are older than 4 Myr should show evidence for the presence of red supergiants. These stars would contribute to the K -band ($2.2\mu\text{m}$) luminosities at the Near-Infrared (NIR) wavelengths. The NIR colors like $(J - K)$ and $(H - K)$ serve as good diagnostics of such a young population (Kotilainen *et al* 1996; Devereux 1989).

Starbursts generally have strong UV to visual continua which is much bluer compared to normal galaxies, since their light is dominated by massive stars at these wavelengths. In “dusty” starbursts and Ultraluminous Infrared galaxies, heavy extinction of the continuum is caused by the dust associated with the star-forming regions. Schmitt *et al* (1997) classified their sample of starburst galaxies based on the extinction and found that the starbursts with higher extinction had weak UV continua and their FIR emissions were higher, which is consistent with the idea that the FIR luminosities are dominated by the thermal emission from dust heated by the UV radiation. Gordon, Calzetti and Witt (1997) find that the UV continuum of starbursts lack the 2175 \AA bump and show a far-UV rise instead. They attribute this to the difference in the grain properties in starbursts, compared to galaxies like our Milky Way. The L_{IR}/L_B ratio represents the ratio of the current massive star formation to the average past star formation, and high values of this ratio (> 1) is indicative of a dominant young starburst.

The X-ray emission in starburst galaxies exhibit a power-law spectrum of index ~ -1.5 between 0.5 and 100 keV. Some of the sources which contribute at these wavelengths include massive binaries, supernova remnants, starburst driven winds and Compton scattering of relativistic electrons by FIR photons (Rephaeli *et al*, 1995).

Spectral line features

Coming to the spectral line features, the spectra at UV, optical and NIR wavelengths are dominated by nebular emission lines and absorption lines of massive stars. The Balmer recombination lines of hydrogen, like H_α and H_β are among the strongest nebular emission lines in the optical and serve as tools to quantify the star formation rates. The Br γ recombination line in the near-IR is also very strong, and can be used to derive the SFR. This line has the advantage that the wavelength-dependent extinction is much lesser at this wavelength compared to the Balmer lines in the optical. The other emission lines include collisionally excited lines from various species like N, O, S, etc in different ionization states. Some of the important absorption lines include the broad Si IV λ 1398 Å and C IV λ 1550 Å features in the UV which are associated with mass outflow from O stars (Weedman *et al*, 1981). In the near-infrared, the presence of an evolved population of massive stars which are in the red supergiant phase is revealed by the Ca II triplet absorption lines at $\lambda\lambda$ 8498, 8542, and 8662 Å. Apart from the stellar lines, there are dust features in the infrared which include the strong silicate absorption feature at 9.7 μm and other broad emission features which are produced by the transient heating of polycyclic aromatic hydrocarbons (Moorwood 1996; and references therein).

1.2.2 Molecular gas content and gas depletion timescales

Since stars are formed from molecular clouds, the occurrence of starbursts depends crucially on the amount of molecular gas available. The CO observations of a sample of nearby starburst galaxies whose SFRs are comparable to the prototype starburst galaxies M82 and NGC 253, show a high concentration of molecular gas in the central regions. The total mass of molecular gas contained within the central 1.2–2.8 kpc diameter, ranges from 10^8 to $10^9 M_\odot$ (Young & Devereux, 1991; Devereux *et al*, 1994). From the CO velocity dispersions, it is found that this mass of molecular gas in some cases is a significant fraction of the total dynamical mass in that region. Jogee (1998) has carried out high resolution study of the molecular gas properties in the inner few kiloparsecs of ten starburst

and non-starburst galaxies, based on interferometric CO (J=1-0) observations. The CO measurements showed that both starbursts and non-starbursts host massive concentration of molecular hydrogen in the inner kpcs. But the high SFRs in starbursts is mainly because they have piled up the gas into a more centrally concentrated configuration, resulting in molecular gas surface densities which are larger by a factor of 3–4 compared to non-starbursts. The peak gas surface densities reach 1000 to 3500 $M_{\odot} \text{ pc}^{-2}$ in starbursts.

The L_{IR}/M_{gas} ratio is an indicator of the star formation efficiency and serves as a tool to identify starbursts. For normal, non-active spiral galaxies this ratio is about 5, while for moderate starbursts it is about 20. However, in the case of ultraluminous infrared galaxies, this ratio can be as high as 200 (Sanders *et al* 1988). From the total molecular gas mass and the luminosity generated by the current starburst episode, it is possible to estimate the gas depletion timescales. For the above range of L_{IR}/M_{gas} values, the timescales of gas consumption would range from 10^8 years for moderate starbursts to shorter timescales of $\sim 10^7$ years for the most luminous IRAS galaxies.

1.2.3 Blue compact dwarf galaxies and Luminous IR galaxies

Blue compact dwarf galaxies (BCDGs) are low-luminosity ($M_B \geq -18$) objects undergoing intense bursts of star formation lasting for less than 10^7 years and separated by long quiescent periods of several billion years. Thus BCDGs form the low-luminosity end of starburst galaxies. These objects are metal-deficient with respect to the solar neighbourhood with $Z_{\odot}/50 \leq Z \leq Z_{\odot}/3$, which implies that they are quite young from the point of view of chemical evolution. BCDGs therefore are the best candidates for studying star formation in nearly primordial environments or conditions prevailing at the time of galaxy formation (Thuan *et al*, 1995, Thuan 1991). The BCDG abundance peaks at $\sim 1/10$ the solar value and IZw18 is the most metal-poor BCDG known so far, with $Z = Z_{\odot}/50$. About 95% of the BCDGs do show an underlying population in deep images, but the two galaxies namely IZw18 and SBS 0335–052 ($Z = Z_{\odot}/41$) which are the most metal poor BCDGs do not show evidence for an underlying population. These two galaxies

seem to be undergoing their first burst of star formation and be considered as primeval galaxies. Most of the massive starburst galaxies show indications of galaxy interactions and mergers. However, a majority of the BCDGs are isolated and hence the star formation is not triggered by interactions. High resolution HI maps show clumpy structures and distinct HI clouds in the vicinity of BCDGs, and this indicates that cloud collisions, shocks and gas inflows could play a major role in triggering the intense star formation episodes (Lequeux & Viallefond 1980; Viallefond & Thuan 1983, Brinks 1997).

The Infra-Red Astronomical Satellite (IRAS) detected a large number of galaxies which emit most of their bolometric luminosities at Far Infra-Red (FIR) wavelengths. Galaxies with $L_{IR} > 10^{11} L_{\odot}$ were classified as Luminous IR galaxies (LIGs), and those with $L_{IR} > 10^{12} L_{\odot}$ were classified as Ultraluminous IR galaxies (ULIGs) (Sanders &, 1996) The ULIGs have the highest FIR luminosities and nearly all of these objects appear to be in advanced stages of galaxy mergers, which are powered by a mixture of circumnuclear starbursts and AGNs. Optical images of ULIGs show that more than 95% of them are merger systems (Sanders *et al* 1988). Heckman *et al* (1987) and Armus *et al* (1989, 1990) carried out long slit optical spectroscopy and H_{α} imaging of LIGs and found that most of these galaxies have loop structures, bubbles and filament-like structures which they interpret as a result of a starburst-driven superwind. The visible spectrum of LIGs show features due to young massive stars, intermediate stars and wolf-rayet stars, indicating recent episodes of star formation. Over the range of luminosities, $L_{IR} = 10^{11} - 10^{12} L_{\odot}$, there is a dramatic increase in the frequency of interacting systems which are extremely gas-rich, with starburst activity dominating at the lower end of this range and AGNs at the higher end. But at $L_{IR} > 10^{12} L_{\odot}$ it is difficult to distinguish whether AGNs or starbursts are the dominant sources, because these systems are enshrouded by huge amounts of dust. Examples of some of the well-studied LIGs include, NGC 4038/4039 (the antennae), NGC 7252 (atoms-for-peace galaxy), IRAS 19254–7245 (the super-antennae) and Arp 220.

1.3 Triggering of starburst activity

As discussed in the previous section, the occurrence of nuclear and circumnuclear starbursts require huge amounts of molecular gas to be accumulated in these regions. In starbursts occurring at the centers of galaxies, it is found that the molecular surface densities and the star formation rates are very high. In a differentially rotating disk, the material at the outer stable orbits have larger specific angular momentum or angular momentum per unit mass, which increases with radial distance. Hence, the infall of gas from the outer orbits to the inner orbits would require an outward transport of angular momentum. One of the main problems in the study of starbursts is to understand the mass-transfer from the outer regions to the inner few kiloparsecs and the mechanisms which actually trigger the starburst activity. The current view is that a major fraction of the gas is acquired during galaxy interactions and mergers, and then driven to the central regions by stellar bars. The formation, evolution and destruction of bars have been extensively studied in the recent years, through numerical simulations using improved hydrodynamic codes (Friedli & Benz 1993,1995; Athanassoula 1992,1994; Combes 1994).

1.3.1 Role of galaxy interactions and mergers

Observations show that interacting galaxies have higher star formation rates compared to non-interacting galaxies (Larson & Tinsley, 1978; Lonsdale *et al*, 1984; Hummel *et al*, 1990). The efficiency of galaxy interactions in triggering starbursts is now rather well-understood through multiwavelength observations (Hummel *et al*, 1990; Joseph & Wright, 1985; Kennicutt *et al*, 1987; Xu & Sulentic, 1991) and numerical simulations. A closely interacting system of galaxies is likely to merge due to the effect of dynamical friction, and the most spectacular starbursts appear at the merger phase of the galaxies. Most of the ultraluminous IRAS galaxies which are powered by starbursts appear to be mergers or strongly interacting galaxies, as revealed by the tidal tails, bridges and double nuclei seen in their optical morphology (Sanders *et al*, 1988; Melnick & Mirabel, 1990; Majewski *et al*, 1993). Galaxy interactions severely affect the behaviour and kinematics

of the dissipational component (the gas) in galaxies. During an interaction, the HI gas disk which is present in the outer parts of the spiral galaxies gets perturbed and the gas is stripped off from the galaxies, resulting in the formation of tails and bridges between them. Observations of molecular gas masses upto $10^{11} M_{\odot}$ in ULFIRs (Sanders *et al*, 1991) indicate that at some stage of the gas inflow most of it gets transformed from atomic to molecular form. From a survey of more than 100 nearby spirals, Braine & Combes (1992, 1993) find that interacting galaxies have 4 times more CO emission than non-interacting galaxies. The gas acquired by a galaxy in its outer parts, through an interaction, can be brought into the central regions in two ways – by strong gravitational and viscous torques introduced by the interaction itself, or by inducing non-axisymmetric perturbations like spiral arms or bars. Numerical simulations have shown that gravitational torques and bars are very efficient in driving large amounts of gas from the outer regions to the inner parts of galaxies (Barnes & Hernquist 1992; Combes *et al*, 1990).

The main effect of the interactions is to introduce non-axisymmetric forces through the disks thereby generating strong gravity torques which drive the gas radially inward. Bars are also generated which play an important role in the central regions. In a non-axisymmetric potential, there are two families of orbits that exist, one aligned along the bar, and another perpendicular to it. At each Lindblad resonance, the families of orbits get interchanged, thereby changing the direction of the torques exerted on the gas inflow. Due to perturbation of the gas in the outer orbits or cloud collisions, the gas streams in elliptical trajectories towards the inner regions. Inside the corotation resonance, the torques are such that the gas is driven towards the inner Lindblad resonance (ILR). In the absence of a central mass concentration, the gas tends to accumulate at the ILR. In the presence of an inner and outer ILR, the gas tends to get trapped between the two ILRs under the influence of two torques acting in the opposite directions. Instabilities arising in the gas accumulated at the ILRs via cloud-cloud collisions can lead to star formation through fragmentation of the gas ring, followed by gravitational collapse of the fragments. If a central mass concentration (a black hole or dense stellar cluster) is present, the torque exerted on the gas pulls it further inwards and it can fuel a nuclear starburst. Jog & Das

(1992) have carried out a detailed analysis of the physical mechanisms that can trigger a burst of massive star formation in the central regions of interacting galaxies. They argue that the cloud–cloud mechanism can result in an overall disruption rather than compression of the clouds to form stars. Also, if cloud collisions are the main triggering mechanism, then the SFR and the ratio of IR luminosity per unit cloud mass should be larger for the smaller mass clouds, due to their higher collision frequency. Hence, Jog & Das consider a mechanism whereby they follow evolution of the interstellar medium in a galaxy which is undergoing an encounter. The interaction causes giant molecular gas clouds from the disk to tumble into the central regions, where they undergo radiative shock compressions due to the pre-existing average high pressure of the central intercloud medium. The compression continues until the crossing time is larger than the growth time of the gravitational instabilities in the shocked outer shell of the giant molecular cloud. The outer shell then fragments and leads to a burst of massive star formation. Though considerable work has been done in the study of mass transfer in galaxies showing nuclear activity, very few of these really address the mechanism that triggers the activity. The self-regulatory and self-propagating nature of starbursts is still a very active area of current research (Elmegreen 1992).

1.3.2 Role of bars in mass transfer

Stellar bars can arise spontaneously in self-gravitating disks as self-sustaining structures, or just transient structures which are generated by tidal interactions (Combes & Elmegreen, 1993; Gerin *et al.*, 1990). Within the corotation resonance, the presence of a bar can cause large scale shocks, whereby the gas loses much of its angular momentum and flows along the leading edge of the bar and dust lanes, towards the nuclear regions. As mentioned in the earlier section, an interaction between disk galaxies also drives gas towards the center by creating a bar or oval distortion. Thus, the gravitational torques produced by bars provide the primary mechanism for mass transfer in galaxies from the outer parts of the disks to central ~ 1 kpc (which corresponds to the location of ILRs).

However, the evidence for dense stellar clusters at the very center of galaxies, or nuclear starbursts, require that the gas be brought further into the few parsecs radii. One mechanism that has been suggested for transport of gas from the ILRs into the nucleus, is that of nested bars or ‘bars within bars’ (Shlosman et al 1989,1990). The secondary bars can be gaseous bars formed from the material accumulated by the primary bar, or maybe a stellar bar, and the bar ends lie at the ILR. Such secondary bars have been observed in the optical/NIR images as well as seen in numerical simulations (Freidli *et al*, 1996; Woznaik *et al*, 1995; Knapen & Beckman, 1994; Combes, 1994). However, it is a matter of debate as to whether bars alone would be sufficient to drive the gas to the inner few parsecs, or other mechanisms like cloud–cloud collisions would be more important at small radii.

1.4 The Starburst–AGN connection

There has been mounting evidence in recent times for the co-existence of starburst and AGN activity in the centers of galaxies. Previously, it was believed that the FIR luminosities of luminous IR galaxies are powered by dust–enshrouded AGNs. However, Smith *et al* (1998) observed a sample of 40 most luminous members of the IRAS bright galaxy sample, and found that the FIR luminosities of these galaxies can be explained by starburst models and that the milliarcsecond scale structures seen in the VLBI images are likely to be complexes of radio supernovae. A few nearby galaxies which show composite nature (Starburst and AGN) includes NGC 1068, NGC 1365, NGC 4303, NGC 4945, NGC 7469, and circinus galaxy. In most of these cases, there is an active Seyfert 2 nucleus and starburst activity in the circumnuclear region.

The standard model for AGNs, considers that most of the continuum luminosity arises from an accretion disc surrounding a supermassive black hole. The optical emission line spectrum of AGNs consists of broad, permitted lines and narrow, permitted and forbidden lines. The broad lines originate from the high velocity clouds ($v \approx 5000 - 10,000 \text{ km s}^{-1}$), which lie close to the accretion disc. Surrounding the broad line region, is the dusty molecular torus. The low velocity clouds ($v \approx 800 - 1000 \text{ km s}^{-1}$), which are responsible

for the narrow lines, are located beyond the molecular torus. Among the AGNs found in nearby spiral galaxies, there are two classes namely Seyfert 1 and Seyfert 2 nuclei. The emission line spectrum of Seyfert 1 nuclei show broad permitted lines and narrow forbidden lines, while the Seyfert 2 nuclei show only narrow permitted and forbidden lines in their spectra. Adopting the standard model for AGNs, the unified models for Seyferts tries to explain the differences seen in these two classes, as a result of the orientation at which these nuclei are viewed. According to the unified model, Seyfert 2 galaxies are seen edge on and the broad line clouds are obscured by the dusty torus as a result of which the broad lines are absent in their spectra. Spectro-polarimetric observations of the two classes gave further support to this view, since broad emission lines appear in the polarised light of Seyfert 2s, which is the light scattered off the dusty torus. Also, the UV continuum of Seyfert 2s is enhanced when viewed in polarised light, confirming that the UV source is actually hidden by the torus (see Antonucci, 1993). However, some of the observed properties of AGNs cannot be satisfactorily explained by the unified model and can be better accommodated with some contribution from starburst activity. The issues which point towards an association between AGN and starburst activity include, the formation of BLR clouds, the relatively low polarizations seen for the UV continuum in contrast to that seen for the broad lines, the enhanced star formation activity and CO emission in Seyfert 2 galaxies, the presence of red supergiants and circumnuclear starbursts preferably in Seyfert 2s, etc. The actual role played by starbursts in AGN activity is still an active area of research, and there are two views that exist - 1) the AGN activity represents different phases in the evolution of a starburst in very dense environments which does not require the formation of a black hole at all (Terelevich & Melnick 1985), and 2) A symbiosis of AGN and circumnuclear starbursts, whereby the young stellar clusters provide the gas to fuel the accretion disc around the supermassive black hole (Perry & Dyson 1985, Perry 1993). Although the details about the role of starbursts is still not clear, there is fairly strong evidence that starburst activity contributes to some of the observed properties of AGNs, in particular the Seyfert 2 galaxies.

1.5 Starbursts and galaxy evolution

Starbursts and galaxy merger-induced activity play a major role in galaxy formation and evolution. The role of starbursts in galaxy evolution was realized through the discovery of a large fraction of blue galaxies in clusters at redshifts of $\sim z \approx 0.4$ (Butcher & Oemler, 1978), IRAS 60 μm source counts, distribution of star forming galaxies from redshift surveys of optically selected galaxies and discovery of an excess population of sub mJy radio sources associated with blue galaxies. These various observations implied an evolution of star forming galaxies out to redshifts of $z = 1$, through interactions and mergers. As discussed in the previous sections, it is now well understood that galaxy interactions/mergers can trigger intense episodes of star formation. But it remains to be seen whether this process extends to much higher redshifts upto an epoch of galaxy formation. At this epoch, the star formation rates would have been very high, about $1000 M_{\odot} \text{ yr}^{-1}$, which implies that the bulk of stars would have formed in starbursts. Ultraluminous galaxies like Arp 220 show evidence for massive star clusters, and also many of the circumnuclear starburst rings contain “super-star clusters” whose properties seem to suggest that they are globular clusters in formation (Ho & Filippenko 1996, Maoz *et al* 1996, Meurer *et al* 1995). The identification of these systems offer much support to the idea that ellipticals are formed from mergers of spiral galaxies, since the main objections to this view had been the inability to explain the abundance of globular cluster systems in elliptical galaxy haloes. Since gas is efficiently converted to stars in starbursts, and massive stars return most of the processed material back into the ISM through stellar winds and supernovae in a short time, they are mainly responsible for the metal-enrichment of the Universe (Madau *et al* 1998).

If the precursors of present day spheroidals, specially the ellipticals and bulges of spiral galaxies are the outcome of major starbursts, it should be possible to identify them by certain tracers like, their relatively flat, featureless UV to blue continuum arising from massive stars, the Lyman and 4000 \AA breaks, and emission features like L_{α} (1216 \AA), [OII](3727 \AA), [OIII](5007 \AA) and H_{α} lines from the photoionized gas. Most of the searches

for primeval galaxies have relied on the L_α emission line and the Lyman break, because for redshifts corresponding to the epoch of galaxy formation, only these features would be shifted to the optical wavelengths while the optical features would have shifted to the NIR wavelengths. However, the number of primeval galaxies found in these searches is much less than what was expected, and this is probably due to the heavy-extinction suffered by the UV radiation (Thompson & Djorgovski 1995, Thompson, Djorgovski & Trauger, 1995). The corresponding re-processed radiation from dust in the FIR would be shifted to sub-millimeter wavelengths and currently searches at these wavelengths are being initiated. Star-forming galaxies at high redshifts can also be identified through multi-color optical imaging which is sensitive to the Lyman break (Adelberger & Steidel, 1997; Steidel *et al*, 1996). Studies based on multicolor imaging using the HST have revealed galaxies with redshifts in the range $3 < z < 3.5$. The QSO absorption line systems arising from galaxies and intergalactic clouds along the line of sight to distant QSOs offer a useful tool to investigate the nature of high redshift galaxies and protogalactic clouds (Heckman 1993, Lanzetta 1993, Petitjean 1997).

Almost all the studies of high redshift galaxies have shown that there exists a considerable fraction of Lyman- α emitting galaxies with high star formation rates at these redshifts. Although the epoch of galaxy formation remains uncertain, it is now clear that starbursts would have had a major role in the formation and evolution of galaxies.

1.6 Thesis outline

The understanding of galaxy formation and evolution is one of the most important, as yet unsolved problems in astrophysics. With the advent of large 10-m class telescopes and space-based telescopes, massive young star clusters are being observed at large look-back times and there is more observational work devoted to studies of star forming galaxies at intermediate and high redshifts. However, in order to understand and interpret the integrated spectra, colors, and luminosities in terms of the IMF, SFR and ages of the ionizing clusters, it is very important to study the properties of star-forming regions in

nearby galaxies.

1.6.1 Motivation

The present work was aimed at studying the properties of star-forming complexes in starburst galaxies, with a view to understand the nature of star formation and the star formation rates. It is well-known that star formation takes place on various scales in mass and luminosity, which are represented by the normal HII regions, giant HII regions, and HII nuclei, with nuclear and circumnuclear starbursts being the extreme cases. We were interested in comparing the SFRs and IMFs of star forming regions under different environments. The project undertaken was intended to address the following aspects;

- the distribution of ionized gas and dust,
- physical conditions in the photoionized gas in nuclear and circumnuclear starburst regions,
- the star formation law – whether instantaneous burst or continuous star formation,
- star formation rates and ages of the young star clusters.

1.6.2 Methodology

In order to study the distribution of ionized gas in galaxies, we used H_α images which essentially trace the sites of recent star formation. Since the dust extinction effects are more severe at shorter wavelengths, the $(B - R)$ color images are useful to study the dust morphology. The physical conditions in the photoionized gas are studied spectroscopically, using diagnostic emission line ratios. Since the H_α recombination line luminosity essentially depends on the ionizing UV luminosity, this has been used to derive the star formation rates and numbers of ionizing stars. To understand whether the star formation scenario is represented by an instantaneous burst or continuous star formation, and to estimate the ages of starburst episodes, we have to rely on evolutionary population

synthesis models. These models use the stellar atmosphere grids and stellar evolutionary codes, to predict the various properties of a young stellar cluster as it evolves in time. The properties like colors, luminosities, equivalent widths, number of ionizing stars, mechanical energy output, etc, are predicted for different IMFs and for different metallicities. The IMFs considered may have different upper and lower mass limits, or different slopes. The metallicities considered range from less than solar metallicities, to few times the solar metallicity. We have used the synthesis models from Mayya (1995, 1997) and the Starburst99 models of Leitherer et al (1999) for this study. These models consider two scenarios of star formation, namely, instantaneous burst (IB) and continuous star formation (CSF). We compare the observed luminosities, colors, and equivalent widths with the predictions made by the models, to obtain consistent ages of the star forming regions and to understand which scenario is acceptable.

In Chapter 2, we present the details of observations and data reduction procedure. We have carried out optical broad band BVR imaging and narrow-band H_α imaging of a sample of starburst galaxies. Spectroscopy of the nuclear regions in the optical and NIR wavelengths were also carried out. The detailed observation log, and method adopted for measurements of the observables, are described.

In Chapter 3, we discuss the star formation in the IR bright galaxy NGC 972. We have carried out a detailed analysis of this galaxy, and derived the SFRs and ages of the star forming regions. The existence of a circumnuclear ring in this galaxy prompted us to obtain NIR images to look for the presence of a bar. We discuss the results from NIR imaging and discuss the need for a revised morphology for this galaxy and the evidence for a merger event.

In Chapter 4, we present the statistical properties of HII regions in the galaxy NGC 1365. We discuss the HII region luminosity function, size distribution and their implications. We also discuss the correlations between the various properties of the HII regions.

In Chapter 5, the results obtained from a spectroscopic study of the starburst nuclei is presented. The physical properties of the ionized gas has been derived from the emission line ratios, and the temperatures of the ionizing stars have been obtained. The star

formation rates have been derived for the nuclear regions, and we use the information on the molecular gas content from literature, to discuss the star formation. The ages of the starburst episodes have been obtained based on evolutionary models, and we find evidence for two bursts of star formation in the nuclear regions.

In Chapter 6, we summarize the main results from this work, and discuss the scope and future prospects of this work.

Bibliography

- [1] Adelberger, K.L., & Steidel, C.C., 1997, ASP conf. series, vol 114, 47
- [2] Antonucci, R., 1993, ARAA, 31, 473
- [3] Armus, L., Heckman, T.M., & Miley, G.K., 1989, ApJ, 347, 727
- [4] Armus, L., Heckman, T.M., & Miley, G.K., 1990, ApJ, 364, 471
- [5] Athanassoula, E., 1992, MNRAS, 259, 345
- [6] Athanassoula, E., 1994, in “*Mass-transfer induced activity in galaxies*”, ed. I. Shlosman, Cambridge Univ. press, 143
- [7] Balzano, V.A., 1983, ApJ, 268, 602
- [8] Barnes, J.E., & Hernquist, L., 1992, ARAA., 30, 705
- [9] Braine, J., & Combes, F., 1992, A&A, 264, 433
- [10] Braine, J., & Combes, F., 1993, A&A, 269, 7
- [11] Brinks, E., 1997, Rev. Mexi. de Astronomia y Astrofisica, 6, 14
- [12] Buat, V., *et al.*, 1989, A&A, 223, 42
- [13] Butcher, H., & Oemler, A., 1978, ApJ, 219, 18
- [14] Combes, F., & Elmegreen, B.G., 1993, A&A, 271, 391
- [15] Combes, F., Dupraz, C., & Gerin, M., 1990, in “*Dynamics and interactions of galaxies*”, Heidelberg Conf., ed. R. Wielen, 205

- [16] Combes, F., 1994, in “*Mass-transfer induced activity in galaxies*”, ed. I. Shlosman, Cambridge Univ. press, 170
- [17] Devereux, N.A., 1989, ApJ, 346, 126
- [18] Devereux, N.A., Taniguchi, Y., Sanders, D.B., Nakai, N., & Young, J. S., 1994, AJ, 107, 2006
- [19] Elmegreen, B.G., 1999, in “*Unsolved problems in Stellar Evolution*”, Ed. M. Livio, Cambridge Univ. Press, (in press)
- [20] Elmegreen, B.G., 1992, in “Star formation in stellar systems”, eds. G. Tenorio-Tagle, M. Prieto, & F. Sanchez, Cambridge Univ. Press, 383
- [21] Friedli, D., & Benz, W., 1993, A&A, 268, 65
- [22] Friedli, D., & Benz, W., 1995, A&A, 301, 649
- [23] Friedli, D., *et al.*, 1996, A&AS, 118, 461
- [24] Gallagher, J.S., Hunter, D.A., & Tutukov, A.V., 1984, ApJ, 284, 544
- [25] Gerin, M., Combes, F., & Athanassoula, E., 1990, A&A, 239, 37
- [26] Gordon, K.D., Calzetti, D., Witt, A.N., 1997, ApJ, 487, 625
- [27] Heckman, T.M., Armus, L., & Miley, G.K., 1987, AJ, 93, 276
- [28] Heckman, T.M., 1993, in “*The environment and evolution of galaxies*”, eds. Shull, J.M., & Thronson, H.A., Kluwer Academic publishers, 155
- [29] Ho, L.C., & Filippenko, A.V., 1996, ApJ.lett, 466, L83
- [30] Hummel, E., van der Hulst, J.M., Kennicutt, R.C., & Keel, W.C., 1990, A&A, 236, 333
- [31] Jog, C.J., & Das, M., 1992, ApJ, 400, 476
- [32] Jog, C.J., 1995, BASI, 23, 135

- [33] Jogee, S. 1998, Ph.D. Thesis, Yale University
- [34] Joseph, R.D., & Wright, G.S., 1985, MNRAS, 214, 87
- [35] Kennicutt, R.C., 1983, ApJ, 272, 54
- [36] Kennicutt, R.C., Keel, W.C., van der Hulst, J.M., *et al*, 1987, AJ, 93, 1011
- [37] Kennicutt, R.C., 1992, in “*Star formation in stellar systems*” eds., G. Tenorio-Tagle, M. Prieto, & F. Sanchez, Cambridge Univ. press, 191.
- [38] Kennicutt, R.C., Tamblyn, P., Congdon, C.W., 1994, ApJ, 435,22
- [39] Kennicutt, R.C., 1998, ARAA, 36, 189
- [40] Knapen, J.H., & Beckman, J.E., 1994, in “*Mass-transfer induced activity in galaxies*”, ed. Shlosman, I., Cambridge Univ. Press, p.100
- [41] Kotilainen, J.K., *et al.*, 1996, A&A, 313, 771
- [42] Lanzetta, K.M., 1993, in “*The environment and evolution of galaxies*”, eds. Shull, J.M., & Thronson, H.A., Kluwer Academic publishers, 237
- [43] Larson, R.B., & Tinsley, B.M., 1978, ApJ, 219, 46
- [44] Leitherer, C., & Heckman, T.M., 1995, ApJS, 96, 9
- [45] Leitherer, C., *et al.*, 1999, to appear in ApJS (astro-ph/9902334)
- [46] Lequeux, J., & Viallefond, F., 1980, A&A, 91, 269
- [47] Lonsdale, C.J., Persson, S.E., & Matthews, K., 1984, ApJ, 287, 95
- [48] Madau, P., Pozzetti, L., Dickinson, M., 1998, ApJ, 498, 106
- [49] Majewski, S.R., *et al*, 1993, ApJ, 402, 125
- [50] Maoz, D., *et al.*, 1996, AJ, 111, 2248
- [51] Mayya, Y.D., & Prabhu, T.P., 1995, AJ, 109, 2503

- [52] Mayya, Y.D., 1997, ApJ.lett, 482, L149
- [53] Melnick, J., & Mirabel, I.F., 1990, A&A, 231, L19
- [54] Meurer, G.R., *et al.*, 1995, AJ, 110, 2665
- [55] Moorwood, A.F.M., 1996, Space Science Reviews, 77, 303
- [56] Neugebauer, G., *et al.*, 1984, ApJ lett., 278, L1
- [57] Perry, J.J., & Dyson, J.E., 1985, MNRAS, 235, 665
- [58] Perry, J.J., 1993, in “*Central activity in Galaxies – From observational data to astrophysical diagnostics*”, eds. Sandquist, A.A & T.P. Ray, Springer-Verlag, 25
- [59] Petitjean, P., 1997, in “*Young galaxies and QSO absorption-line systems*”, eds. Viegas, S.M., Gruenwald, R., de Carvalho, R.R., ASP conference Series, vol. 114, 11
- [60] Rieke, G.H., Lebofsky, M.J., Thompson, R.I., Low, F.J., & Tokunaga, A.T., 1980, ApJ, 238, 24
- [61] Rieke, G.H., Loken, K., Reike, M.J., & Tamblyn, P., 1993, ApJ, 412, 99
- [62] Rodriguez-Pascual, P.M., Mas-Hesse, J.M., Sanz Fernandez de Cordoba, L., Mirabel, I.F., makino, F., *et al.*, 1993, ApSS, 205, 113
- [63] Rephaeli, Y., Gruber, D., & Persic, M., 1995, A&A, 300, 91
- [64] Salpeter, E.E., 1955, ApJ, 121, 161
- [65] Sandage, A., 1986, A&A, 161, 89
- [66] Sanders, D.B., *et al.*, 1988, ApJ, 325, 74
- [67] Sanders, D.B., Scoville, N.Z., Soifer, B.T., 1991, ApJ, 370, 158
- [68] Sanders, D.B., & Mirabel, I.F., 1996, ARAA, 34, 749
- [69] Scalo, J.M., 1986, Fundamentals of cosmic physics, 11,1
- [70] Scalo, J.M., 1998, ASP conf. series, vol. 142, 201

- [71] Schmitt, H.R., Kinney, A.L., Calzetti, D., Storchi-Bergmann, T., 1997, AJ, 114, 592
- [72] Shlosman, I., Frank, J., & Begelman, M.C., 1989, Nature, 338, 45
- [73] Shlosman, I., Begelman, M.C., & Frank, J., 1990, Nature, 345, 679
- [74] Smith, H.E., Lonsdale, C.J., Lonsdale, C.J., 1998, ApJ, 492, 137
- [75] Soifer, B.T., Houck, J.R., & Neugebauer, G., 1987, ARAA, 25, 187
- [76] Steidel, C.C., Giavalisco, M., Pettini, M., Dickinson, M., & Adelberger, K.L., 1996, ApJ, 462, L17
- [77] Terelevich, R., & Melnick, J., 1985, MNRAS, 213, 841
- [78] Thompson, D., & Djorgovski, S.G., 1995, AJ, 110, 982
- [79] Thompson, D., Djorgovski, S.G., Trauger, J., 1995, AJ, 110, 963
- [80] Thuan, T.X., 1991, in "Massive stars in starbursts", eds. C. Leitherer, N.R. Walborn, T.M. Heckman, & C.A. Norman, STScI symp. series 5, 183.
- [81] Thuan, T.X., Izotov, Y.I., & Lipovetsky, V.A., 1995, in "*The interplay between massive star formation, the ISM and Galaxy Evolution*" eds., Kunth, D., Guiderdoni, B., Heydari-Malayeri, M., & Thuan, T.X., 383.
- [82] Viallefond, F., & Thuan, T.X., 1983, ApJ, 269, 444
- [83] Woznaik. H., Friedli, D., Martinet, L., Martin, P., & Bratschi, P., 1995, A&A Suppl. Series, 111, 115
- [84] Weedman, D.W., Feldman, F.R., Balzano, V.A., Ramsey, L.W., Sramek, R.A., & Wu, C.-C., 1981, ApJ, 248, 105
- [85] Xu, C., & Sulentic, J.W., 1991, ApJ, 374, 407
- [86] Young, J.S., & Devereux, N.A., 1991, ApJ, 373, 414

Chapter 2

The sample selection, observations and data reduction

2.1 Introduction

Star-forming regions in galaxies are composed of young stars, gas and dust. These various components emit large number of photons at different wavelengths across the electromagnetic spectrum, and thereby provide signatures of current star formation activity. The present work aims at using the various observables at optical wavelengths to understand massive star formation properties in a sample of nearby spiral galaxies.

Optical imaging was done to identify the sites of massive star formation, and to obtain the broadband colors, H_α fluxes and equivalent widths. These observables provide information about the star formation rates and the star formation histories of these regions. Optical–NIR spectroscopy of starburst nuclei was performed to study the physical conditions in the photoionized gas and the stellar populations in these regions.

2.2 Sample selection

The present study has made use of imaging and spectroscopic data, aimed at investigating various aspects of star formation in galaxies. The imaging data were intended for a study

of the global star formation properties of galaxies like— the morphology of the ionized gas, HII region luminosity function, HII region diameters, and to obtain the magnitudes and colors by performing photometry of the HII regions. Further, we were interested in comparing the properties of the circumnuclear HII regions with that of disk HII regions. For this, one requires a sample of nearby spiral galaxies (at distances of about 10 megaparsecs) which subtend large angular diameters, so that the individual HII regions can be identified and aperture photometry can be performed on them. The sample galaxies were mainly chosen from three sources:

1. Sersic & Pastoriza (1965) — This is a compilation of galaxies which show evidence for circumnuclear hotspots, usually within few hundred parsecs from the nucleus, or have amorphous nuclei. It is known that most of these galaxies harbour an AGN or starburst nucleus.
2. Devereux (1987) — This is a list of starburst galaxies based on the $10\mu\text{m}$ emission. It includes all nearby non-Seyfert1 galaxies at distances $15 < D(\text{Mpc}) < 40$, with central $10\mu\text{m}$ luminosities $\geq 6 \times 10^8 L_{\odot}$, declinations $> -20^{\circ}$, right ascensions between 22 and 16 hours, and Galactic latitudes $\geq 20^{\circ}$.
3. Young *et al.*, (1989) — A compilation of infra-red bright galaxies, with declinations $\geq -20^{\circ}$ and $B_T \leq 12$. We considered a subset from this list, with $D_{25} \geq 3$ arcmin and $L_{IR}/L_B \geq 0.5$.

The final list of objects which were chosen for imaging studies is given in Table 2.1.

The spectroscopic data were intended to study starburst nuclei and compare them with other active nuclei and HII nuclei. We used the sample of starburst galaxies given by Devereux (1989), along with a few other well-known starbursts for spectroscopic observations. The list of objects that were used for the spectroscopic study is given in Table 5.1 of chapter 5.

Table 2.1

Global parameters of the observed galaxies

Galaxy name	Type	R.A.(J2000)	Dec(J2000)	$\log D_{25}$	B_T	V_o km s ⁻¹	Distance Mpc	Scale (1" in pc)
N470	Sbc(s)II.3	01 19 45.6	+03 24 37	1.45	12.53	2374	31.65	153.4
N972	Sbpec	02 34 13.3	+29 18 42	1.52	12.27	1543	20.57	99.72
N1365	SB(s)I-I-II	03 33 36.6	-36 08 17.0	2.05	10.32	1640	18.2	88
N1569	SmIV	04 30 50.3	+64 50 47	1.56	11.86	-89	1.18	5.74
N1808	Sbcpec	05 07 42.8	-37 30 51	1.81	10.76	1005	13.40	64.96
N2273	SBa(r)	06 50 08.6	+60 50 45	1.43	13.10	1840	24.53	118.92
N2750	SABc	09 05 48.1	+25 26 09	1.34	12.38	2674	35.65	172.83
N2782	Sa(s)pec	09 14 05.5	+40 06 52	1.54	12.30	2562	34.16	165.60
N2903	SAB(rs)bc	09 32 09.7	21 30 02	2.10	9.68	556	6.3	30.54
N3310	Sbc(r)pec	10 38 46.1	+53 30 08	1.49	11.15	980	13.06	63.314
N3504	SBb(s)I-II	11 03 10.8	+27 58 25	1.43	11.67	1539	20.52	99.48
N4102	Sb(r)II	12 06 23.4	+52 42 41	1.48	11.99	837	11.16	54.10
N4984	Sa(s)	13 08 57.2	-15 30 58	1.44	12.25	1206	16.08	77.95

The sample was chosen such that the galaxies could be conveniently observed from the Vainu Bappu Observatory, which is located at a latitude of 12.5°N , during the observing season from October–April. However, most of the imaging nights during 1995–1997 were non-photometric and hence it was impossible to perform a flux calibration of the images. We have therefore used these images to discuss the emission line morphology which traces the distribution of ionized gas (see section 2.6).

In the case of NGC 972 and NGC 1365, we obtained good quality data and these galaxies were studied in detail (see chapters 3 and 4). The spectroscopic data obtained during 1997–1998, were obtained under fairly stable sky conditions and hence could be flux calibrated. The inferences drawn from the spectra are mostly based on ratios of emission line intensities which are close in wavelengths and on equivalent widths, and are not much affected by the calibration inaccuracies. However, the emission line fluxes and luminosities derived for individual lines will suffer large errors if the spectrophotometric calibrations are not accurate. We compared the H_α fluxes obtained in the present work, with other published work and find that the measurements are in good agreement. Near-IR images of NGC 972 were obtained at the 2.1-m telescope of the Observatorio Astronomico Nacional at San Pedro Martir, Baja California and the details of the observations and reductions are presented in Chapter 3.

2.3 Observational details

All observations required for the present study were obtained using the 2.34-m Vainu Bappu Telescope (VBT), at the Vainu Bappu Observatory, Kavalur (India). The data were acquired on a Tektronix CCD chip of 1024×1024 format. The CCD camera and the controller unit were procured from Photometrics Ltd. A CCD is characterized by its “gain” which gives the number of electrons corresponding to one count and the “readout noise” which is the minimum irreducible noise associated with the system. The CCD used for this study during the period 1995–1997 (CCD1) has a gain of 5.9 electrons per ADU and readout noise of 7.2 electrons while the CCD used during the period April 1997–

1998 (CCD2) had a gain of 8.9 electrons/ADU and a readout noise of 10 electrons.

2.3.1 *BVR* and H_α imaging

Broad band *BVR* and H_α imaging were carried out at the prime focus of the VBT. The details of the filter system used are given in Table 2.2.

Table 2.2

<i>Description of filters</i>	
Filter	$\lambda/\Delta\lambda$
<i>B</i>	4400/1050
<i>V</i>	5425/1050
<i>R</i>	6550/1300
H_α	6581/100

The image scale at the detector plane is determined by the F -ratio (F/D), which is the ratio of the effective focal length of the telescope to the diameter of the primary mirror. The image scale offered by the $F/3$ beam at the prime focus of the VBT is $0.''6 \text{ pixel}^{-1}$, and the entire CCD covers a field of $10' \times 10'$ on the sky.

In all CCD systems, a minimum positive voltage is applied to prevent negative signals. In other words, even a ‘no-signal’ condition will always correspond to some positive offset or bias signal. The minimum voltage amounts to some digital counts in the output images, and this bias level needs to be subtracted from the object frames. In order to estimate this bias level, we took five to six bias frames (zero exposure time with shutter closed) and used a median of these frames as the master bias frame. The bias level was found to be stable throughout the night as well as for different nights.

CCDs do not have uniform response to light across their surfaces. The pixel-to-pixel variations in sensitivity arise due to physical differences between the pixels as a result of the fabrication processes and due to optical attenuation effects such as microscopic dust particles on the surface of the CCD (McLean, 1989). These variations may be only few per

cent of the mean sensitivity, but they must be removed because such variations result in a noisy image at a level corresponding to few per cent of the sky brightness. The sensitivity of the CCD also depends on the wavelength of observation. To estimate these sensitivity variations ‘flat-field’ frames are usually taken in different filters, using an illuminated white screen on the dome as a flat-field source. This helps in uniformly illuminating the CCD and hence the pixel-to-pixel sensitivity can be accurately calibrated. Vignetting due to the telescope and instrument apertures, on the other hand, can be estimated only by observing a distant object and sky images are most convenient. We have used good signal-to-noise twilight sky flats to calibrate for both vignetting and pixel-to-pixel sensitivity variations. We obtained five to six flat-field frames in each filter using twilight sky, on each of the observing nights.

Signals are produced in CCDs even at room temperature due to the thermal energy of free electrons. This current which results from the random motion of electrons is called the ‘dark current’ and can be minimised by cooling the detector. The dark current levels which still remain, can be determined by long exposures with the CCD shutter kept closed. These exposures are done in the night with exposure times similar to that used for the object frames. We found that the dark current level in our CCD is very low and amounts to only a few electrons.

The exposure times for the sample galaxies in the broadbands usually ranged from 300 to 900 seconds, while longer exposures of 1200s to 1800s were used for the narrow band $H\alpha$ filter. After each galaxy observation, a spectrophotometric standard whose declination is roughly close to that of the galaxy, was observed for the purpose of calibration. The detailed log of observations is given in Table 2.3. The seeing values given in the table refer to the full-width at half maximum of a stellar profile from the galaxy image frame.

The images observed in the broad bands need a calibration to the standard magnitude system. The “dipper asterism” region in the open cluster M67 has been the most commonly used CCD standard-star field for photometric calibration because it contains a large number of moderately bright, well separated stars with color indices ranging from $B - V = -0.1$ to 1.4, all within a few square arcminutes.

Table 2.3

Observation log for imaging data

Galaxy name	Date of obs.	Filter	Exposure time (seconds)	airmass	seeing (arcsec)	Standard star
N972	051196	<i>B</i>	300	1.04	2.4	PG0310+149
	061196	<i>B</i>	900	1.04	2.3	
	051196	<i>V</i>	300	1.04	2.3	
	061196	<i>V</i>	600	1.04	2.5	
	051196	<i>R</i>	600	1.07	2.3	
	061196	<i>R</i>	300	1.05	1.8	
	051196	H_{α}	900	1.19	2.1	
	051196	H_{α}	600	1.24	2.1	
	061196	H_{α}	1200	1.06	2.1	
N1365	290198	<i>B</i>	900	1.51	2.9	LTT1788
	300198	<i>B</i>	900	1.53	2.6	
	290198	<i>V</i>	600	1.54	2.7	
	300198	<i>V</i>	600	1.56	2.7	
	290198	<i>R</i>	600	1.57	2.8	
	300198	<i>R</i>	600	1.60	2.8	
	290198	H_{α}	1200	1.62	2.8	
	300198	H_{α}	900	1.67	2.9	
N1569	310198	<i>V</i>	600	1.75	2.6	
	310198	<i>R</i>	300	1.78	2.7	
	310198	H_{α}	300	1.81	2.7	
	310198	H_{α}	600	1.84	2.8	

Table 2.3 (*continued*)
Observation log for imaging data

Galaxy name	Date of obs.	Filter	Exposure time (seconds)	airmass	seeing (arcsec)	Standard star
N1808	240196	<i>B</i>	300	1.69	3.1	LTT2415
	051196	<i>B</i>	900	1.68		
	240196	<i>V</i>	300	1.73	2.9	
	051196	<i>V</i>	600	1.78		
	240196	<i>R</i>	120	1.78	2.3	
	051196	<i>R</i>	300	1.81		
	240196	<i>Hα</i>	600	1.88	2.7	
	051196	<i>Hα</i>	900	1.60		
	N2750	290198	<i>B</i>	1200	1.03	2.3
310198		<i>B</i>	1200	1.05	2.1	
290198		<i>V</i>	600	1.02	2.1	
310198		<i>V</i>	900	1.02	2.6	
290198		<i>R</i>	600	1.02	2.4	
310198		<i>R</i>	600	1.05	2.8	
290198		<i>Hα</i>	1200	1.03	2.6	
310198		<i>Hα</i>	1200	1.08	2.7	
N2782		060297	<i>B</i>	1200	1.14	2.5
	070297	<i>B</i>	1200	1.20	3.0	
	060297	<i>V</i>	900	1.15	3.2	
	070297	<i>V</i>	900	1.28	3.1	
	060297	<i>R</i>	900	1.18	2.8	
	070297	<i>R</i>	900	1.23	2.9	
	060297	<i>Hα</i>	1200	1.13	2.1	
	070297	<i>Hα</i>	1200	1.16	2.4	

Table 2.3 (continued)
Observation log for imaging data

Galaxy name	Date of obs.	Filter	Exposure time (seconds)	airmass	seeing (arcsec)	Standard star
N2903	240196	<i>B</i>	600	1.01		PG0939+0262
	190396	<i>B</i>	900	1.05		Feige34
	070297	<i>B</i>	900	1.01	3.8	Feige34
	240196	<i>V</i>	600	1.02		
	190396	<i>V</i>	600	1.08		
	070297	<i>V</i>	900	1.01	3.9	
	240196	<i>R</i>	300	1.04		
	190396	<i>R</i>	600	1.11		
	070297	<i>R</i>	600	1.01	3.8	
	240196	<i>Hα</i>	600	1.06		
	190396	<i>Hα</i>	900	1.02		
	070297	<i>Hα</i>	900	1.02	3.2	
	N3310	060297	<i>B</i>	600	1.33	2.3
070297		<i>B</i>	900	1.35	3.4	
310198		<i>B</i>	600	1.43	2.2	
060297		<i>V</i>	600	1.34	3.1	
070297		<i>V</i>	900	1.33	3.1	
310198		<i>V</i>	300	1.46	2.2	
060297		<i>R</i>	600	1.35	2.9	
070297		<i>R</i>	900	1.34	3.2	
310198		<i>R</i>	300	1.51	2.4	
060297		<i>Hα</i>	600	1.32	2.0	
070297		<i>Hα</i>	900	1.32	2.9	
310198		<i>Hα</i>	600	1.56	2.4	

The accurate photometry for the stars in this field is available extensively in the literature (Schlid 1983, Chevalier & Ilovaisky 1991, Gilliland *et al* 1991, Mayya 1991, Bhat *et al* 1992, Anupama *et al* 1994). We observed the “dipper asterism” region on most of the nights, as M67 is available during most part of the observing season at VBO.

2.3.2 Optical and near–infrared spectroscopy

Spectroscopic observations of the sample galaxies was done at the Cassegrain focus of the VBT, using the Opto-Mechanics Research (OMR) spectrograph. The spectra were obtained using a 600 line mm^{-1} grating blazed at λ 7500Å, yielding a spectral coverage of about 3000 Å on the Tektronix CCD of 1024×1024 format and a spectral resolution of 5.2Å. The blue spectra covering the wavelength range from λ 4500 to 7200 Å were obtained by choosing a central wavelength at λ 5700Å. The red spectra from \sim 6400 to 9100 Å which covers the Near–IR features, were obtained by choosing a central wavelength of λ 7700 Å. The contamination from overlapping blue spectra of the second order was removed using suitable filters. The f/13 beam provides an image scale of 6.78 " mm^{-1} at the cassegrain focus of the VBT. The spectrograph camera introduces a reduction factor of 6.6, and hence the final image scale at the detector is about 1.06 " pixel^{-1} . The spectra were obtained by using a long slit of \sim 2.5', across the nucleus of the galaxy along the North–South direction. The slit width was kept at 300 μm for all observations which corresponds to a projected slit width of two pixels on the detector plane. As in the case of imaging observations, about 4–5 bias frames were taken at different times throughout the night during spectroscopic observations. Flat–field frames were obtained by using the in-built flat–field source available within the spectrograph. After each object spectrum, the comparison spectrum was taken using the Fe–Ar arc lamp for the blue region and Fe–Ne arc lamp for the red region. The spectrophotometric standards were observed after each galaxy spectrum, at similar hour angles whenever possible. The exposures were typically 1800s to 2700s for the galaxy spectra and about 900s to 1200s for standard star spectra. The log of spectroscopic observations is given in Table 2.4.

Table 2.4
Observation log for Spectroscopic data

Galaxy name	Date of obs.	Wavelength range	Exposure time (seconds)	airmass	Standard star
N470	311297	4500-7200	2400	1.05	Feige25
	020198	6400-9100	2400	1.05	
N972	301297	4400-7100	2700	1.04	HD19445
	301297	4400-7100	2400	1.05	
	311297	4500-7200	1800	1.12	Feige25
	020198	6400-9100	1800	1.06	
	020198	6400-9100	2400	1.10	
	030198	6400-9100	2400	1.04	
	230298	6400-9100	2700	1.33	Hiltner600
N1808	301297	4400-7100	2400	1.60	LTT2415
	301297	4400-7100	244	1.76	
	020198	6400-9100	1800	1.70	
	020198	6400-9100	1800	1.90	
	030198	6400-9100	2400	1.62	
	220298	6400-9100	2700	1.57	
N2273	301297	4400-7100	2400	1.59	Hiltner600
	311297	4500-7200	2400	1.52	
	311297	4500-7200	2400	1.53	
	010198	6400-9100	1800	1.51	
	010198	6400-9100	1800	1.50	
	030198	6400-9100	2400	1.57	
	220298	6400-9100	2700	1.55	
	230298	6400-9100	2700	1.51	
	240298	6400-9100	2400	1.54	

Table 2.4 (*continued*)
Observation log for Spectroscopic data

Galaxy name	Date of obs.	Wavelength range	Exposure time (seconds)	airmass	Standard star
N2750	311297	4500-7200	2400	1.02	Hiltner600
	311297	4500-7200	2400	1.06	
	010198	6400-9100	2400	1.04	
	230298	6400-9100	2700	1.04	
	240298	6400-9100	2700	1.02	
	170498	4300-7000	2400	1.19	
	N2782	301297	4400-7100	2400	
301297		4400-7100	2400	1.16	
020198		6400-9100	2400	1.13	
220298		6400-9100	2700	1.13	
230298		6400-9100	2700	1.13	
180498		4400-7100	2700	1.13	
190498		6400-9100	2700	1.13	
040598		6400-9100	2400	1.14	
040598		6400-9100	1800	1.13	
N3310		190397	4500-7200	2700	1.33
	311297	4500-7200	1800	1.34	
	220298	6400-9100	2400	1.33	
	230298	6400-9100	2400	1.35	
	190498	6400-9100	2700	1.32	
	040598	6400-9100	2400	1.34	
	050598	6400-9100	2700	1.32	

Table 2.4 (continued)*Observation log for Spectroscopic data*

Galaxy name	Date of obs.	Wavelength range	Exposure time (seconds)	airmass	Standard star
N3504	190597	4500-7100	2400	1.06	Feige66
	170498	4300-7000	2400	1.08	
	190498	6400-9100	2700	1.04	Feige34
	040598	6400-9100	2400	1.12	
N4102	190397	4600-7100	2700	1.32	Hz44
	170498	4300-7100	2700	1.35	
	180498	4400-7200	2700	1.44	
	190498	6400-9100	2700	1.32	
	050598	6400-9100	2400	1.33	
N4984	170498	4300-7100	2400	1.41	Feige34
	040598	6400-9100	2400	1.22	

2.4 Reduction of imaging data

The reduction procedure adopted for astronomical data aims at filtering out the signal which is due to the astronomical source alone, by removing the contributions due to any other sources. Some of these contributions like the bias counts are additive, while others like the sensitivity variations from pixel to pixel are multiplicative. These effects have to be corrected for, before the source counts are estimated. The data reduction was done using the Image Analysis and Reduction Facility (IRAF) software package.

2.4.1 Basic steps in reduction

The preliminary steps involved in the data reduction are outlined below. A master bias which was obtained by averaging many bias frames was subtracted from the flat-field and object frames (galaxy images and standard star images). The dark current in the CCD was negligible and hence dark current subtraction was not performed. The individual flat-fields in different filters were first normalized; and the normalized flats in a particular filter were then median combined to prepare the master flat for that filter. The object frames were then divided by the master flats prepared for the corresponding filters. Since the exposure times for the galaxy images are fairly long, many cosmic ray events get registered on the CCD and these amount to counts several times greater than the sky background noise. In some cases, when multiple exposures were available in a given filter, the cosmic rays were removed through median filtering. In other cases, the cosmic rays were eliminated using an interactive procedure *cosmicrays* available in the reduction software. The sky background was estimated from a corner of the object frame, which is relatively free of light contamination from the stars and galaxies.

2.4.2 Aperture photometry

Photometry refers to actually measuring the number of photons from an astronomical source and characterizing its brightness. The brightness is measured in “magnitudes”, and is the radiant flux expressed on a logarithmic scale. We performed aperture photometry,

using a circular aperture of a particular radius which encloses the source, and the number of counts within this aperture was determined. An annular ring of much larger radius and width of about 5 pixels was used to estimate the background counts. The background counts were subtracted from the counts measured within the aperture to get the actual counts from the source of interest. These counts were converted into an instrumental magnitude using the expression $-2.5 \times \log_{10}(\text{counts in electrons/s})$. Aperture photometry of the standard stars, and of the HII regions identified on the galaxy images, were done using the *phot* task available under APPHOT package of the IRAF software. Photometry was done using apertures of different sizes, and the final aperture was chosen based on the aperture growth curve, by seeing for what sizes the magnitude differences remain constant.

2.4.3 Photometric calibration

Once the instrumental magnitudes are obtained, they must be calibrated against ‘standard’ systems like those available from photoelectric photometry, so that data from different sources can be intercompared. The light loss through the Earth’s atmosphere per unit airmass, or the atmospheric extinction is first accounted for, by using the expression;

$$b_o = b_i - k_b X_b \quad (2.1)$$

$$v_o = v_i - k_v X_v \quad (2.2)$$

$$r_o = r_i - k_r X_r \quad (2.3)$$

where, the subscript ‘*i*’ denotes instrumental magnitudes and the subscript ‘*o*’ denotes magnitudes corrected for atmospheric extinction. k_b, k_v, k_r are the extinction coefficients and X_b, X_v, X_r are the airmass in *B, V*, and *R* filters respectively. We used the extinction coefficients determined by Mayya (1992). The airmass was calculated using;

$$X = [\sin(\phi)\sin(\delta) + \cos(\phi)\cos(\delta)\cos(H)]^{-1} \quad (2.4)$$

where, ϕ, δ and H are the latitude of the observatory, declination of the object and hour angle at which the image was taken. The magnitudes which have been corrected for atmo-

spheric extinction are transformed to the standard ‘Johnson–Cousin’ BVR magnitudes through a set of equations given below;

$$V - v_o = \alpha_v + \beta_v(b - v)_o \quad (2.5)$$

$$B - V = \alpha_{b-v} + \beta_{b-v}(b - v)_o \quad (2.6)$$

$$V - R = \alpha_{v-r} + \beta_{v-r}(v - r)_o \quad (2.7)$$

where, $(b - v)_o = b_o - v_o$, and $(v - r)_o = v_o - r_o$. V , $B - V$, and $V - R$ refer to magnitude and colors in the standard system. For a well-calibrated standard star field, like the dipper asterism region of M67, the righthand side of the above equations is known, and the instrumental magnitudes for these stars can be used to obtain the transformation coefficients α and β . The coefficient α is the zeropoint and is the magnitude corresponding to 1 count/s for a star of zero color-term, above the Earth’s atmosphere. The coefficient β is the color term which relates the CCD + filter system used in this study, to the standard system. The transformation coefficients obtained for the two CCDs used in the present work, are tabulated in Table 2.5.

Table 2.5

Calibration transformation coefficients obtained for different observing runs

Period of Obs.	Quantity	α	β	Std.error	comments
1996–97	$B - V$	-0.656 ± 0.028	1.437 ± 0.033	0.0078	CCD1,
	$V - R$	-0.310 ± 0.002	1.029 ± 0.017	0.012	old filters
	V	21.710 ± 0.143	0.307 ± 0.244	0.025	
1997–1998	$B - V$	-1.190 ± 0.013	0.957 ± 0.006	0.016	CCD2,
	$V - R$	-0.290 ± 0.009	1.032 ± 0.009	0.016	new filters
	V	21.954 ± 0.012	0.064 ± 0.014	0.018	
1998	$B - V$	-1.102 ± 0.013	0.965 ± 0.007	0.012	CCD2,
	$V - R$	-0.190 ± 0.007	1.042 ± 0.011	0.008	new filters
	V	21.517 ± 0.020	0.031 ± 0.019	0.035	

The variations in the zeropoint from night to night were corrected for, by observing standard star fields from Landolt (1992). In some cases, a few stars from M67 itself, were used to estimate the zeropoints. On several nights, the zeropoints were found to differ by as much as 0.3 magnitudes. Since most of the data were obtained with non-photometric sky, we have not used these observations for estimating the magnitudes and colors. Most of the galaxy images were therefore used to study only the morphological properties, and are discussed in section 2.6. NGC 972 and NGC 1365 could be observed on photometric nights and were studied in more detail (chapters 3 and 4).

2.5 Reduction of spectroscopic data

The preliminary steps involved in the reduction of spectroscopic data are much the same as in the case of imaging data. The first steps in reduction involve subtracting a master bias from the object spectra (galaxy and standard star), which is then divided by a normalized flat-field to correct for pixel to pixel variations.

2.5.1 Extraction of spectrum

The extraction of spectra involves specifying the location or center of the object on the slit, the aperture size which would sample the region of interest along the spatial extent of the object, and then tracing the curvature of the object spectrum along the dispersion axis. The task *apall* in the SPECRED package available in IRAF, allows to perform these operations easily. The one-dimensional spectra were extracted by adding up 6 pixels along the spatial axis. The background was estimated through a spline fit to the counts in two sky apertures located on either side and much beyond the extraction aperture.

2.5.2 Wavelength calibration

In order to obtain the wavelength calibration (the relationship between the pixel number and wavelength), the comparison arc spectra were extracted using the same apertures

as used for the object spectra. The lines in the comparison spectra were assigned the laboratory wavelengths by using the *identify* task, aided by the linelist available in the NOAO library. The dispersion correction is determined from the wavelength calibrated arc spectrum by fitting a Legendre polynomial of order 2 or 3. The object spectrum obtained using the *apall* task is in counts versus pixels. This was wavelength calibrated using the task *dispcor* with the corresponding arc spectrum as reference. The resulting spectrum is now in counts versus wavelength.

2.5.3 Flux calibration

The galaxy spectra were then flux calibrated by deriving the counts to flux units conversion using the spectra of spectrophotometric standards. The NOAO database has calibration files which contain the magnitudes of the standard stars integrated over many wavelength bins or bandpasses. Each bin is about 50\AA and spans the whole range of optical wavelengths. The magnitudes in the database are converted to flux units, using the formula

$$F_{\lambda} = F_{\lambda_0} \times 10^{-0.4m} \quad (2.8)$$

where, F_{λ_0} is the flux of a zero magnitude star. The task *standard* was used to integrate the observed standard spectra over the calibration bandpasses. The counts integrated over these bandpasses are then compared with the standard fluxes within these bandpasses to derive the relation between them. The standard star calibration measurements were then used to determine the system sensitivity as a function of wavelength. When the observing conditions are poor, and the spectra are obtained under variable transparency (during periods of thin, passing clouds), the entire sensitivity curve varies by a constant factor. Hence the relative fluxes of the program star can be calibrated accurately even when the skies are not photometric.

2.5.4 Estimation of continuum

We performed a continuum-fit only for the NIR spectra. The main lines of interest in this region are the Calcium triplet lines, and this region is severely affected by absorption bands of TiO and other metal lines. This makes it very difficult to define a proper continuum level. Thus, in order to be consistent with earlier studies, we chose to do a continuum-fit using the same method adopted by other authors (Diaz, Terelevich & Terelevich 1989; Terelevich, Diaz & Terelevich 1990). Diaz, Terelevich & Terelevich found that the continuum is remarkably flat between $\lambda 8440\text{\AA}$ and $\lambda 8800\text{\AA}$ for a large sample of stellar spectra covering a wide range in surface gravity and metallicity. They define a pseudo-continuum by performing a linear fit to the median value of two chosen side-bands, centered at $\lambda 8455\text{\AA}$ and $\lambda 8850\text{\AA}$, with a width of 15\AA . We fit a spline of order one to the mean counts in these two sidebands to obtain the continuum. For the emission lines, we have used the flux on either side of the line to estimate the local continuum.

2.5.5 Measurement of equivalent widths and fluxes

The equivalent width of an emission line is defined as the ratio of the flux in the line to the flux in the continuum. In the case of an absorption line, it is defined by the area of a rectangle whose area is equivalent to the area covered by the absorption line profile.

We have measured the equivalent widths and fluxes of the emission lines using two methods available in the task *splot*. One method involves marking the two edges of the line at the continuum, and integrating the flux within the area under the line profile. The other method involves fitting the line profile with a gaussian defined by a constant continuum level, and the full-width at half maximum about the central wavelength. Both these methods give very similar values for the fluxes and equivalent widths, except if the line profile is highly asymmetric. In all the spectra the H_α and $[\text{NII}]\lambda\lambda 6548,6583$ emissions are blended, and in some cases the $[\text{SII}]\lambda\lambda 6717,6731$ lines are also blended. The lines were de-blended using the option available in *splot*. The lines were fitted with multiple gaussians and the contributions due to each line was estimated. This requires

the continuum level, centre of the different lines, and sigma of the gaussian profile, to be given as input. While fitting individual gaussian, we gave weightage to the left wing or right wing depending on the asymmetry in the line profile so as to best sample all the flux within the profile. In the case of the Calcium triplet absorption lines, the equivalent widths were measured with respect to the pseudo-continuum described in the previous section. In this case a gaussian profile was fitted to the line by providing the central wavelength and sigma.

The equivalent widths and fluxes measured for the sample of starburst galaxies was then used to understand the physical properties and star formation histories in these regions. The detailed discussion of the results is presented in chapter 5.

2.6 Distribution of dust and ionized gas in galaxies

H_α images of galaxies have been one of the main tools to study the distribution of ionized gas in them. The images taken with the H_α filter samples the red continuum in addition to the H_α recombination line emission. We estimated and subtracted this continuum contribution from the H_α images by adopting the procedure given by Waller (1990), to obtain the pure emission line image. Deep H_α images of star-forming galaxies often reveal loops, shells and filament-like structures extending much beyond the boundaries of the HII regions. Tenorio-Tagle & Bodenheimer (1988) refer to ionized gas shells with radii greater than 300 parsecs, as supershells. The filaments and supershells may have sizes of a few kiloparsecs. Some of the filaments and loops are parts of the shell structures, or blown-out bubbles, while some of the filaments may arise as a result of outflows from star-forming regions.

The star-forming regions in galaxies are associated with large amounts of dust which cause severe extinction of radiation emitted by these regions. The presence of dust is revealed by the lowering of the H_α/H_β ratios, compared to the theoretical values, and this is often referred to as the Balmer decrement. Further evidence for dust is brought out by the increased far-infrared emissions. The effect of dust is wavelength-dependent, with

the short wavelength radiation experiencing more extinction than the longer wavelengths. The B band image samples the young stars and ionized gas and also experiences the effects of dust extinction, while the R band samples the underlying stellar population and is relatively free of dust effects. Thus, the B/R color map can be used to reveal the dust morphology in galaxies. However, the red colors in such an image cannot be always attributed to dust, since a fairly red stellar population is also revealed in a color map.

The structures seen in the dust and ionized gas morphology often show the influence of massive stars on the interstellar medium (ISM), and may extend to fairly large distances. In fact, they indicate that the ISM is disturbed by the energetics associated with OB star formation through stellar winds and supernovae. The ionized shells, and filaments act as the feedback mechanism by which the massive stars interact with the ISM, and even produce conditions that can help in the triggering of a second generation of star formation. Apart from the ionized gas associated with the regions of star formation like, the HII regions, and shells, etc, there is often a diffuse ionized component that is distributed throughout the body of the galaxy. This diffuse component and the ionized filaments are most probably ionized by the UV photons leaking from the star-forming regions and hence are useful for estimating the amount of ionizing flux which escapes from HII regions.

The distribution of dust and ionized gas in the individual galaxies observed as a part of this study, is discussed below:

NGC 972:

This is an IR bright galaxy whose complicated dust distribution gives it a very peculiar morphology. The broad band images of this galaxy shows a very dominant continuum while the H_α emission line images reveal the active star formation in the nucleus, circumnuclear regions and disk of this galaxy. The H_α photographic image of this galaxy was presented by Hodge & Kennicutt (1987), but with CCD images of better quality, we have been able to study the star formation in this galaxy in more detail. Based on our data and the spectroscopic information available in the literature (Ho *et al* 1997), we have

concluded that NGC 972 hosts a starburst nucleus (Ravindranath & Prabhu 1998). We have also obtained the NIR images for NGC 972, and a weak bar has been detected in the K-band (Mayya, Ravindranath & Carrasco, 1998). The H_α image and the B/R , NIR color maps are given in Chapter 3.

NGC 1365:

The barred galaxy NGC 1365 is an actively star-forming galaxy as is revealed by the large numbers of HII regions distributed along its spiral arms. This galaxy has been studied

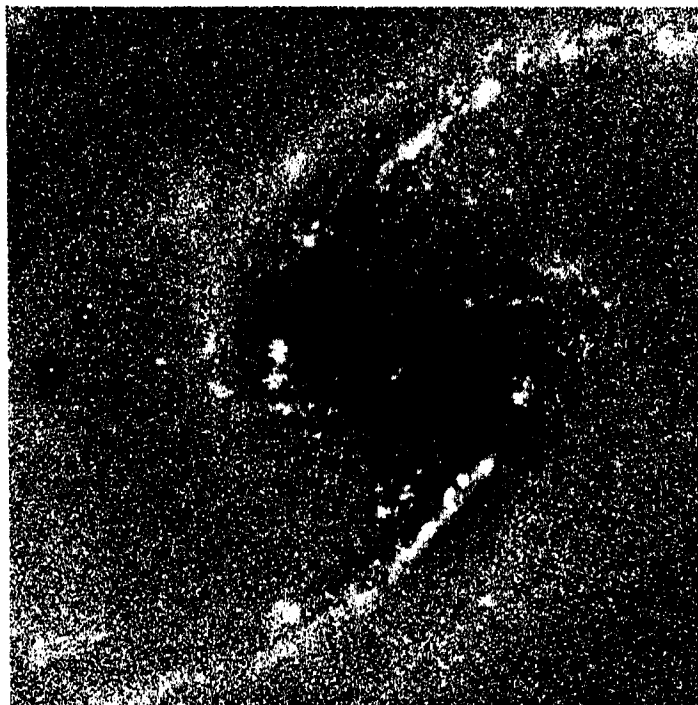


Figure 2.1: The B/R color image of NGC 1365. The field shown here covers $8' \times 8'$. North is up and east is left. The blue regions are lighter while the red regions appear darker.

in great detail through spectroscopic observations and its kinematics have been probed using HI data. As a part of this thesis work we have identified 44 HII regions in addition to the 54 HII regions used by Roy & Walsh for their spectroscopic study, and used all the 98 HII regions to study their statistical properties (Ravindranath & Prabhu 1999). The

details of our analysis and the H_α image of NGC 1365 are presented in Chapter 4. Figure 2.1 shows the B/R color map of NGC 1365. The dust is located at the inner side of the spiral arms, while the HII regions preferably occupy the outer edge along the arms. The dust morphology along the bars is interesting, since it essentially traces the gas flow along the bar, right into the nuclear region to fuel the active Seyfert nucleus of NGC 1365.

NGC 1569:

NGC 1569 is extraordinary for its intense star formation activity, which is spread across the whole of this dwarf galaxy. The ISM in this galaxy is disturbed by the influence of its massive stars as is revealed by the ionized structures emanating from its star forming regions. The H_α image of NGC 1569 is shown in figure 2.2. The galaxy is surrounded by

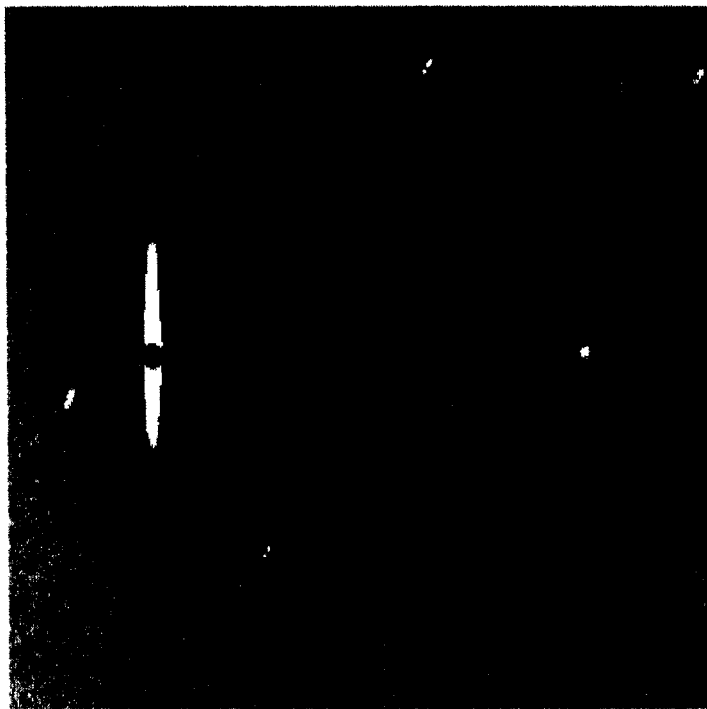


Figure 2.2: The H_α image of NGC 1569. The disruptive effect of the massive stars on the ISM are responsible for the filaments and loops. The residuals of stars arise due to difference in the PSFs of the continuum and emission line images. North is to the left and east is to the top.

filaments which extend to large distances, like 3.6 kiloparsecs from the galaxy. Hunter *et al* (1993) suggested that these large filaments could be formed due to supershells fragmenting above the galactic disks. This view was supported by Heckman *et al* (1995) through X-ray and optical observations. Hunter & Gallagher (1997) carried out a spectroscopic study of the ionized filaments to confirm the source of ionization, through the use of diagnostic emission line ratios. They conclude that the ionization of the filaments is mainly due to photoionization by massive stars. In most galaxies, about 25% of the ionizing photons escape from the HII regions, but in the case of highly disrupted galaxies like NGC 1569, a much larger fraction of ionizing photons can escape.

NGC 1808:

NGC 1808 is well-known for the composite nature of its nucleus and the radial dust filaments emanating from the nucleus. The H_{α} image (figure 2.3) shows a chain of HII regions along the major axis of the galaxy. There are weaker HII regions located in a ring

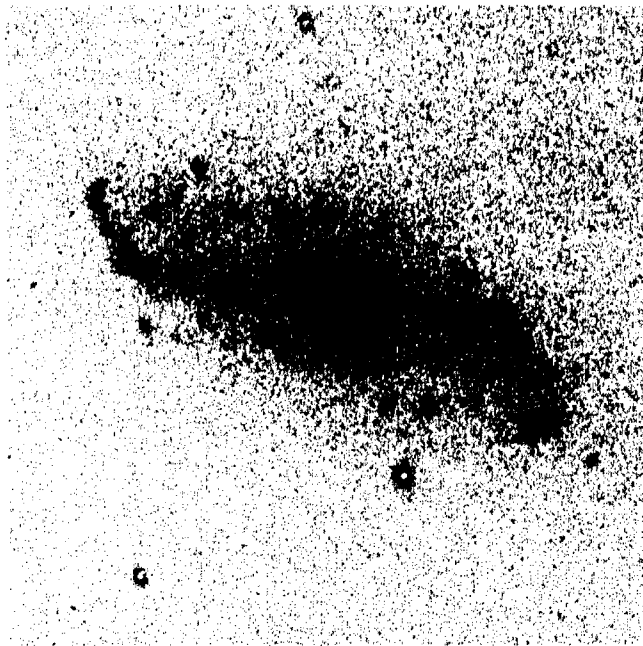


Figure 2.3: The H_{α} image of NGC 1808. The HII regions are predominantly arranged along a bar-like structure, parallel to the major axis. North is to the right and east is to the bottom.

along the north-west and south-east directions. The circumnuclear region has several hotspots and in the B/R color map (figure 2.4) two of the hotspots appear blue. The color map reveals radial dust filaments which extend upto kiloparsec distances. The dust filaments form a cone which obstructs the radiation from the spiral arm lying behind it. This plume of dust could be a result of supernovae that have occurred in the central regions, since the radio images of the nucleus reveals a number of compact supernova remnants.

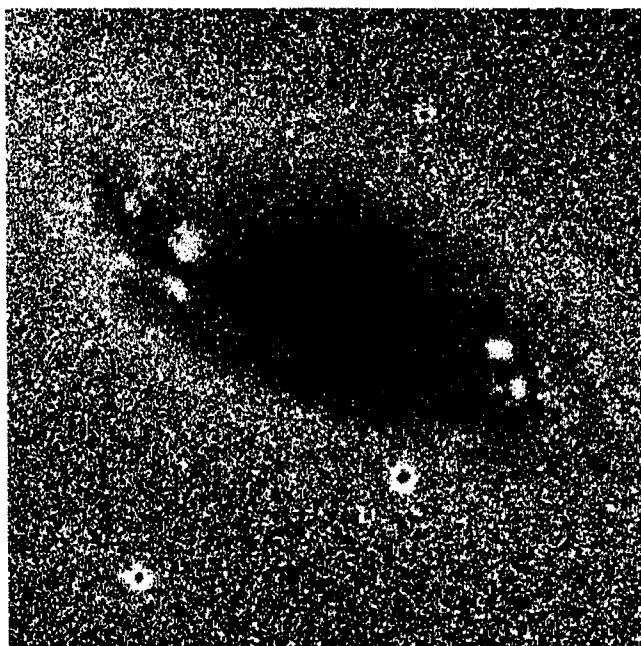


Figure 2.4: The color image of NGC 1808. The prominent feature is the radial filaments of dust which arise from the central starburst. Blue regions appear lighter while the red regions appear darker. Orientation is similar to figure 2.3.

NGC 2750:

There is very little information about NGC 2750 in the literature. It appears in the spectroscopic study of Ho *et al* (1997), and in the starburst galaxy sample defined by Devereux (1989). A study of the molecular gas in starburst nuclei by Devereux *et al* (1994) shows that there is about $10^9 M_{\odot}$ of molecular gas within the central 1.3 kpc

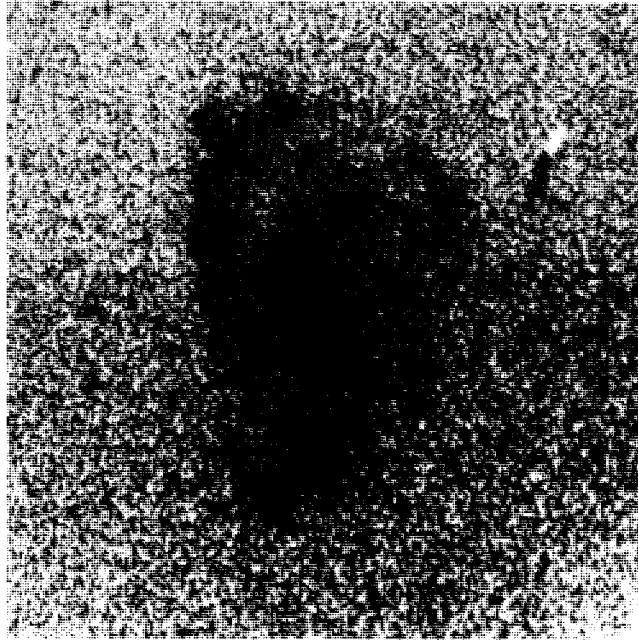


Figure 2.5: The H_α image of NGC 2750. North is to the left and east is to the bottom.

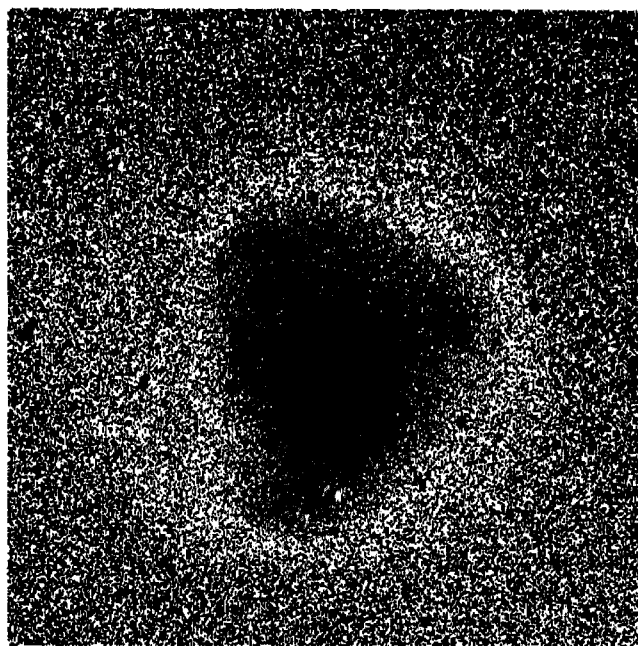


Figure 2.6: The B/R color image of NGC 2750. orientation is similar to figure 2.5. Blue regions appear lighter while the red regions appear darker.

radius of this galaxy. The H_α image of NGC 2750 is shown in figure 2.5 and the B/R color map is shown in figure 2.6. The H_α images show ionized gas distributed throughout the disk of the galaxy. There is a very prominent H_α complex at the end of the spiral arm on the east. The dust distribution shows a red ring around the nucleus, but the color map does not show any complex dust morphology in the disk.

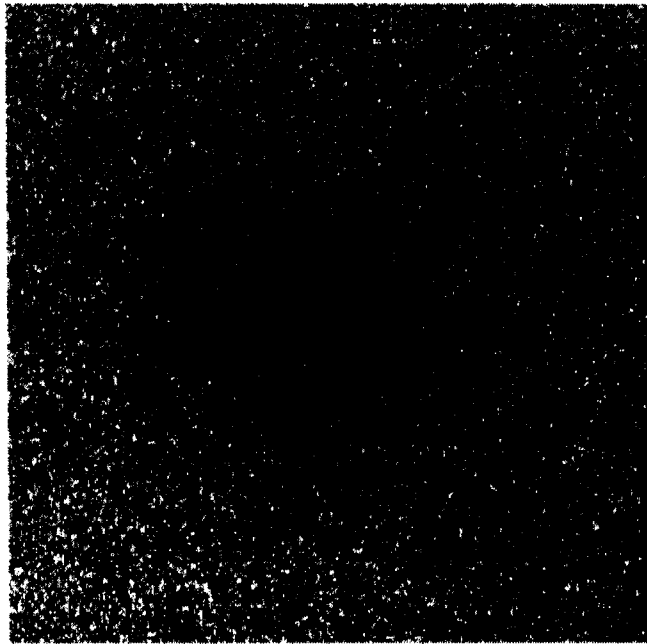


Figure 2.7: The H_α image of NGC 2782. North is to the left and east is to the top. The arc can be seen in the north-west direction.

NGC 2782:

NGC 2782 has been classified as a nuclear starburst galaxy based on the optical emission line spectrum (Balzano 1983, Kinney *et al* 1984, Kennicutt *et al* 1989, Boer *et al*, 1992). The galaxy shows a high surface density of molecular gas, $\approx 1000\text{--}2000 M_\odot \text{pc}^2$ in its center (Jogee 1998, Devereux *et al*, 1994). The broadband optical images show a prominent stellar tail extending to the east, while the color images show four to five arcs or ripples. All these features support that the galaxy has undergone a merger or is in the late stage of interaction (Smith 1994). The H_α image presented in figure 2.7, shows that the central

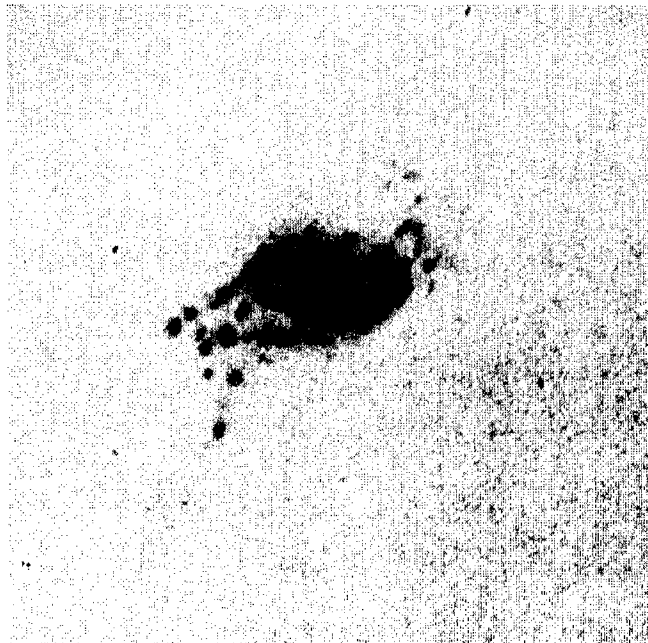


Figure 2.8: The H_{α} image of NGC 3310. The arrow is seen emanating from the central region and extending in the north-west direction. North is towards the left, and east is to the top.

source is very strong in H_{α} emission, and there is an arc in the northwestern direction. The arc is composed of three well-defined emission knots.

NGC 3310:

NGC 3310 is a well-known starburst galaxy and has often been considered as an archetyp-ical starburst, like M82. At radii very close to the center, the galaxy exhibits very tight wound spiral structures and circumnuclear star formation. The H_{α} emission line image (figure 2.8), shows a large number of HII regions. However, the most prominent feature of this galaxy is the “bow and arrow” structure, with the arrow pointing radially outward from the nucleus in the north-west direction and the bow formed by an arc on the western side. These structures have been interpreted as the remnants of a colliding galaxy (Balick & Heckman, 1981). The B/R color map is shown in figure 2.9.

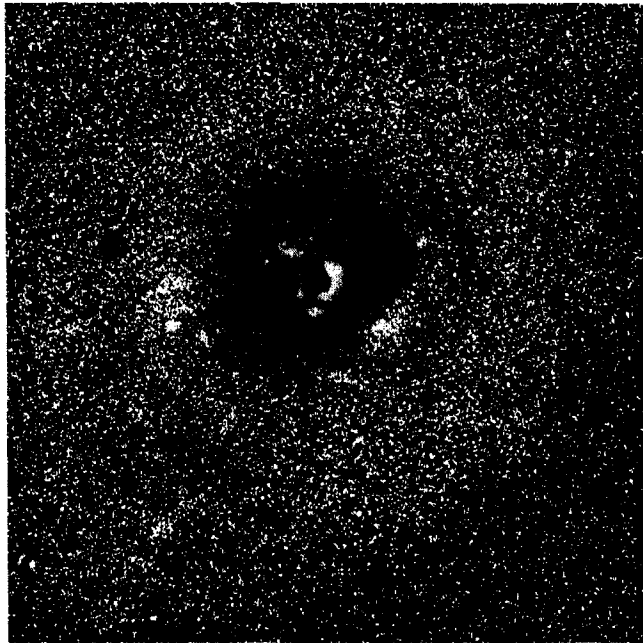


Figure 2.9: The B/R color image of NGC 3310. Red regions appear dark and blue regions appear light. North is to the left and east is upwards.

2.7 Summary

In this chapter we have provided a description of the sample selected for the present study. The observational details have been discussed and the log is presented for both imaging and spectroscopic observations. The basic reduction steps involved in obtaining the observables, namely magnitudes and colors of star-forming regions, have been described. The determination of the photometric zeropoints and transformation of the magnitudes and colors to the standard photometric system is discussed. The processes involved in obtaining the emission line fluxes and equivalent widths of the H_α emission line from the imaging data will be discussed in chapters 3 and 4. The procedure involved in extraction of one-dimensional spectra, wavelength calibration and flux calibration are also explained. Finally, the measurement of fluxes and equivalent widths from spectroscopic data are discussed followed by brief notes on the emission line morphology and color maps of a few sample galaxies.

Bibliography

- [1] Anupama, G.C., *et al*, 1994, A&AS, 103, 315
- [2] Balzano, V.A., 1983, ApJ, 268, 602
- [3] Balick, B., & Heckman, T.M., 1981, A&A, 96, 271
- [4] Bhat, P.N., *et al*, 1992, JAA, 13, 293
- [5] Boer, B., Schultz, H., & Keel, W.C., 1992, A&A, 260, 67
- [6] Chevalier, C., & Ilovaisky, S.A., 1991, A&AS, 90, 225
- [7] Devereux, N.A., 1989, ApJ, 346, 126
- [8] Devereux, N.A., *et al*, 1994, AJ, 107, 2006
- [9] Diaz, A.I., Terlevich, E., & Terlevich, R., 1989, MNRAS, 239, 325
- [10] Forbes, D.A., Boisson, C., & ward, M.J., 1992, MNRAS, 259, 293
- [11] Gilliland, R.L., *et al*, 1991, AJ, 101, 541
- [12] Heckman, T., *et al*, 1995, ApJ, 448, 98
- [13] Hodge, P.W., & Kennicutt, R.C., 1983, AJ, 88, 296
- [14] Hunter, D.A., Hawley, W.N., & Gallagher, J.S., 1993, AJ, 106, 1797
- [15] Hunter, D.A., & Gallagher, J.S., 1997, ApJ, 475, 65
- [16] Jogee, S., 1998, Ph.D thesis, Yale University

- [17] Kennicutt, R.C., Keel, W.C., Blaha, C.A., 1989, AJ, 97, 1022
- [18] Kinney, A.L., *et al*, 1984, PASP, 96, 398
- [19] Landolt, A.U., 1992, AJ, 104, 340
- [20] Mayya, Y.D., 1991, JA&A, 12, 319
- [21] Mayya, Y.D., Ravindranath, S., & Carrasco, L., 1998, AJ, 116, 1671
- [22] McLean, I.S., 1989, "*Electronic and computer-aided astronomy*", Ellis Horwood, Chichester
- [23] Phillips, A.C., 1993, AJ, 105, 486
- [24] Ravindranath, S., & Prabhu, T.P., 1998, AJ, 115, 2320
- [25] Ravindranath, S., & Prabhu, T.P., 1999, *to appear in the proceedings of the conference "Galaxy Evolution on Cosmological timescales"*
- [26] Schild, R.E., 1983, PASP, 95, 1021
- [27] Sersic, J.L., & Pastoriza, M., 1965, PASP, 77, 287
- [28] Smith, B.J., 1994, AJ, 107, 1695
- [29] Tenorio-Tagle, G., & Bodenheimer, P., 1988, ARA&A, 26, 145
- [30] Terlevich, E., Diaz, A.I., & Terlevich, R., 1990, MNRAS, 242, 271
- [31] Young, J.S., *et al*, 1989, ApJS, 70, 699
- [32] Waller, W.H., 1990, PASP, 102, 1217

Chapter 3

Massive star formation in the Infra-red bright galaxy NGC 972

3.1 Introduction

The northern galaxy NGC 972, also known as UGC 02045 is remarkable for its chaotic dust distribution in the main body, which makes it similar in appearance to the prototype starburst galaxy M82. de Vaucouleurs *et al.* (1991, hereafter RC3) classify it as morphological type Sab and in the Revised Shapely Ames Catalogue by Sandage & Tammann (1987), it has been classified as Sb pec. However, Krienke & Hodge (1974) had found the galaxy to be sharing many properties of I0 type galaxies and accordingly the galaxy was given an I0 classification in the Second Reference Catalogue of Bright Galaxies (de Vaucouleurs, de Vaucouleurs & Corwin 1976). NGC 972 has often been listed in the class of M82 type galaxies (Andreasyan & Khachikyan, 1980; Burbidge, Burbidge & Prendergast, 1965). The bright main body of the galaxy exhibits very complicated dust patterns and the deep optical images reveal the outer regions with much fainter and smooth light distribution. Interestingly the presence of these dust lanes has played a major role in its classification both as Sb and I0 — the dusty trailing arm supporting its Sb classification, and the chaotic appearance caused by dust placing it in the class of I0 galaxies. This

highlights the limitation of the qualitative classification schemes based solely on the optical morphologies, especially for the dust-rich galaxies such as NGC 972. Recent advances in observational techniques and theoretical modeling of galaxy dynamics allow the use of many more properties than just optical morphology to establish the true classification of galaxies. From the observational side, NIR imaging allows us to have a dust-free view of the underlying morphological components of galaxies. Such observations have already helped discover new components such as nuclear spirals and bars in galaxies, whose optical appearance did not suggest the existence of those components (Zaritsky, Rix & Rieke 1993; Knapen et al. 1995). From RC3, the heliocentric and GSR -relative systemic velocities are 1543 and 1640 km s⁻¹ respectively, giving an estimated distance of 21.9 Mpc for the galaxy (using $H_0 = 75$ km s⁻¹ Mpc⁻¹). At this distance 1 arcsec corresponds to 105 pc.

Condon & Broderick (1988), Young *et al.* (1989) and Spinoglio & Malkan (1989) give a good compilation of the radio and infrared properties of NGC 972. Interesting correlations of the IRAS 40 - 120 μ m luminosity with the molecular gas mass and H α luminosity for spiral galaxies support the view that a major contribution to the FIR luminosity is the thermal emission from dust heated by massive stars. Hence, the $L(40 - 120\mu m)$ luminosities are used to quantify massive star formation rates. NGC 972 belongs to the list of early-type spiral galaxies with the highest far infrared luminosities ($L(40 - 120\mu m) \geq 10^{10} L_{\odot}$) compiled by Devereux & Hameed (1997). Like most of the galaxies belonging to this list NGC 972 reveals huge complexes of HII regions in the H α images, which are hidden from view in the continuum images due to the dominant stellar bulge. Condon & Broderick use the far-infrared to radio flux density parameter (U) and the infrared spectral index α_{IR} to identify the energy source. They conclude that the radio and infrared emission seen in NGC 972 is powered by a starburst. The L_{IR}/L_B ratio is 2.02 and $\log L(40 - 120\mu m) = 10.43 L_{\odot}$ and these high values support the starburst nature of NGC 972, since they imply the presence of a recent burst of formation of massive stars.

The total blue magnitude (B_T) corrected for Galactic and internal absorption, is 11.46 (Tully, 1988) and the corresponding blue luminosity in solar units is given by $\log L_B =$

10.27. Previous studies involving a photometric investigation of NGC 972, show that half of the light of this galaxy is concentrated within a radius of 35 arcsec (Andreasyan & Khachikyan, 1980). Vennick & Richter (1994) analysed the B band surface brightness profile and found that the brightness distribution can be approximated by two exponentials and the change in the profile towards the outer regions indicates the presence of a halo component. Hodge & Kennicutt (1983) mention the identification of 13 HII regions in NGC 972 while presenting their atlas of HII regions in galaxies. Spectroscopic studies of NGC 972 have been carried out by Andreasyan & Khachikyan (1980), Taniguchi (1986) and Ho *et al.* (1995) with a view to establish the nature of the nuclear activity. All these studies have emphasized the presence of a strong continuum and an emission line spectrum typical of gaseous nebulae. Since the H_α + $[NII]$ emission lines are strong throughout the main body of the galaxy, Burbidge, Burbidge & Prendergast (1965; BBP65) used these intense emission lines to obtain the rotation curve of NGC 972. They estimate a mass of $9 \times 10^9 M_\odot$ interior to 36 arcsec (≈ 4 kpc) and the total mass of the galaxy is estimated to be $1.3 \times 10^{10} M_\odot$ (BBP65; Roberts 1969). The mass of neutral hydrogen within the galaxy is $1.05 \times 10^9 M_\odot$ (Tully, 1988).

In this chapter, we present the results of optical–NIR broad band ($BVRJHK$) and H_α emission line imaging study of NGC 972, with an aim to understand the morphology, photometric properties, and evolution of the star-forming regions using evolutionary synthesis models (Ravindranath & Prabhu, 1998; Mayya, Ravindranath & Carrasco, 1998). A brief description of the observations and reductions is provided in section 3.2 and the results are presented in section 3.3, followed by discussions in section 3.4. Based on the H_α fluxes we obtained and other information available in the literature, we discuss the nature of the ionizing source which powers the nuclear emission line spectrum of NGC 972, emphasizing its similarities with other classical starburst galaxies. We also discuss the possible mechanisms that could have triggered the nuclear starburst and circumnuclear star formation activity.

3.2 Observations and Reductions

3.2.1 Optical BVR and H_α imaging

Broad band BVR images and narrow band $H_\alpha(100 \text{ \AA})$ images were obtained on 5 and 6 November 1996 using the 2.34m Vainu Bappu Telescope equipped with a 1024×1024 pixels Tektronix CCD. The image scale at the prime focus corresponds to 0.6 arcsec per pixel, and the CCD covers a field of $10 \text{ arcmin} \times 10 \text{ arcmin}$ on the sky. Exposure times and other observational details are summarized in Table 3.1. The Landolt standard star field PG 0231+051 (Landolt, 1992) was observed for local atmospheric extinction correction. The spectrophotometric standard star PG 0310+149 from Massey *et al.* (1988) was observed in the R band as well as the H_α band for flux calibration.

Table 3.1
Summary of observations

Telescope:	2.34m VBT		
CCD array:	1024×1024 Tektronix CCD		
Image scale:	0.6"/pixel		
Date of observation:	5 & 6 November 1996		
Seeing:	1.8", 2.0"		
Date	Filter	$\lambda/\delta\lambda(\text{\AA})$	Exposure time (s)
5 Nov 96	B	4400/1050	300
5 Nov 96	V	5425/1050	300
5 Nov 96	R	6550/1300	600
5 Nov 96	H_α	6581/100	1500
6 Nov 96	B	4400/1050	900
6 Nov 96	V	5425/1050	600
6 Nov 96	R	6550/1300	900
6 Nov 96	H_α	6581/100	1200

Bias subtraction and flat-fielding were done using the standard package *ccdred* under IRAF¹ image reduction software. After cosmic ray removal the frames were aligned through a geometrical mapping using the *geotran* and *geomap* tasks available in the reduction software. The transformed star positions agreed to within 0.3 pixels as judged from the coordinates of common stars in different frames.

The H_α images contain a significant amount of the red continuum that passes through the 100 Å passband of the H_α filter. The subtraction of the continuum contribution to the H_α band was done by following the method described by Waller (1990). The sky level was estimated from the R and H_α images and subtracted. The scaling factor between R and H_α bands was determined using the foreground stars in the field of the galaxy. Aperture photometry of the individual HII regions identified on the pure emission-line image, was done using the *apphot* package in IRAF. After sky subtraction from the broad band and H_α frames, the underlying galaxy background was estimated by defining rectangular apertures on either side of the circular apertures enclosing the individual HII regions. The mean background value from the rectangular apertures adjacent to the HII region of interest was subtracted from the counts within the HII region aperture. The non-uniformity of the galaxy background can introduce considerable errors in the photometry, particularly for the HII regions lying near the bulge of the galaxy. Also, the circular apertures chosen for the individual HII regions sample only the core of the emission region even though the actual emission extends beyond our apertures. We used similar apertures for most of the HII regions, typically 3–4 arcsec. Hence some of the large HII regions may be undersampled and the H_α fluxes given in this work are only the lower limits. The results of aperture photometry are given in Table 3.2. Photometry of the galaxy was also performed using the same apertures given in Longo & de Vaucouleurs (1983). We find that our photometric errors are about 0.008 mag in V and 0.04 mag in $(B - V)$.

¹IRAF is distributed by National Optical Astronomy Observatories

3.2.2 Near Infrared *JHK* imaging

Near infrared observations were carried out using the CAMILA instrument (Cruz-Gonzalez et al. 1994) at the 2.1-m telescope of the *Observatorio Astronómico Nacional* at San Pedro Martir, Baja California. The CAMILA instrument uses a NICMOS 3 detector of 256×256 pixel format. The instrument was used in the imaging mode with the focal reducer configuration $f/4.5$ in all our observations. This results in a spatial resolution of $0.''85/\text{pixel}$ and a total field of view of $3.'6 \times 3.'6$.

The imaging observations were carried out on the night of 13 September 1997 using the broad band filters J, H, K' . Each observation consisted of a sequence of object and sky exposures, with the integration time of an individual exposure limited by the sky counts, which was kept well below the non-linear regime of the detector. The net exposure times on the object were 12, 6 and 5 minutes for J, H and K' bands respectively. Roughly equal amounts of time were spent on the sky fields. Photometric calibration to the standard JHK system was performed using the UKIRT standard star FS 7 (Casali & Hawarden 1992). The sky conditions were photometric and the sky magnitudes were roughly 15.9, 14.2 and 11.5 magnitude arcsec^{-2} in J, H , and K bands respectively. The seeing FWHM was typically $2.''0$.

The image processing involved subtraction of the bias and sky frames, division by flat field frames, registration of the images to a common co-ordinate system and then stacking all the images in a filter. Bias subtraction was carried out as part of the data acquisition. The sky frames in each filter were prepared by combining all the sky frames using the median operation. Flat field frames were taken during twilight period. A master flat field frame for each filter was constructed by stacking several night-sky subtracted twilight frames in corresponding filters. The flat fielding operation involved dividing the sky subtracted images of the object by normalized master flats. The resulting images were aligned to a common co-ordinate system using the common stars in the frames and then combined using the median operation. The resulting combined images were aligned to the image from the Digitized Sky Survey (DSS), through a geometrical mapping using the

GEOTRAN and GEOMAP tasks available in the reduction software. The transformed star positions in the images agreed to within 0.2 arcsec as judged from the coordinates of common stars. The results of surface photometric analysis in JHK bands, the color profiles, scale lengths and central optical depths were published in Mayya, Ravindranath & Carrasco (1998).

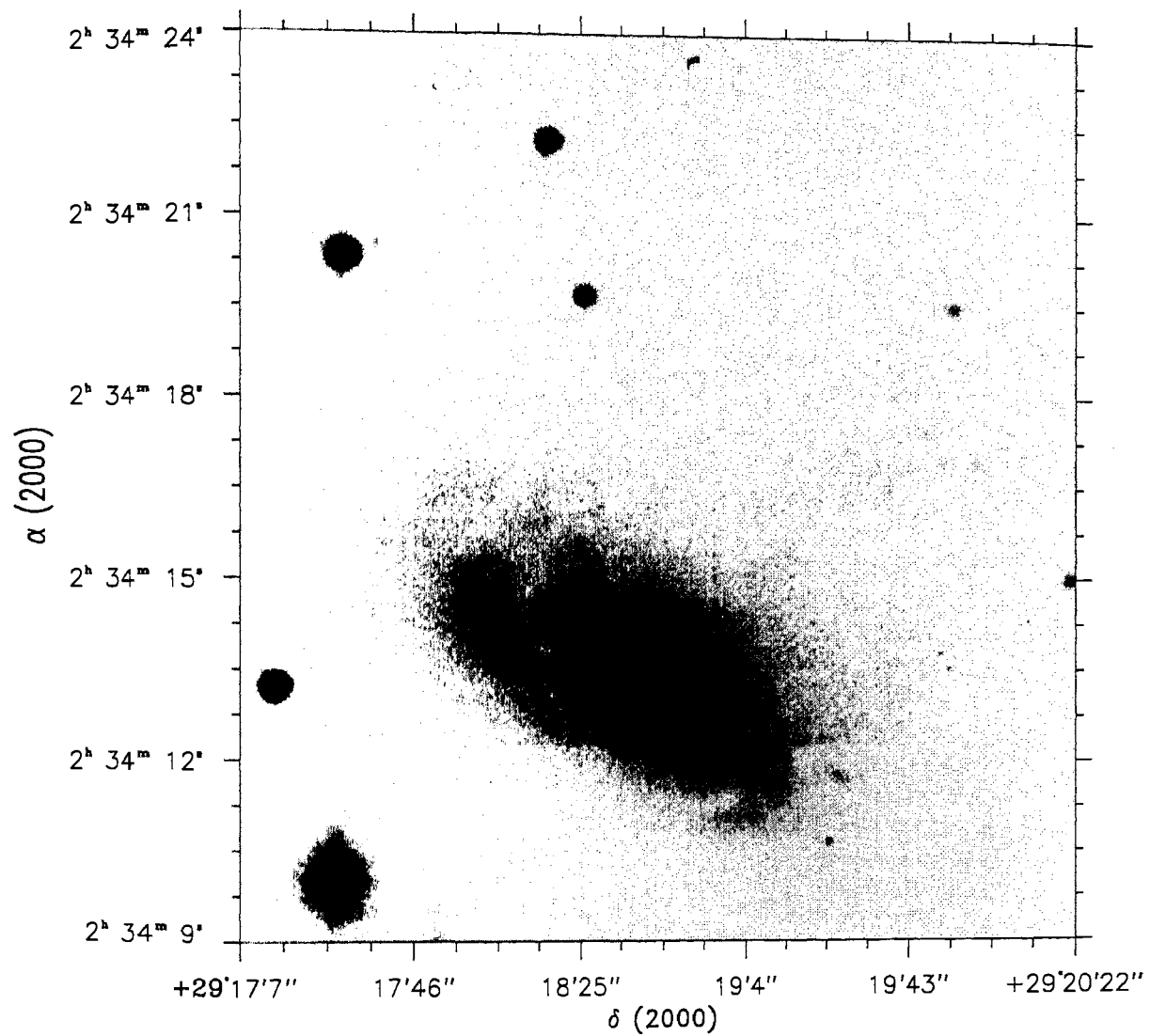


Figure 3.1: Broadband B image, revealing the peculiar morphology of NGC 972. North is to the right and east is to the top. The total field is $3'.25 \times 3'.25$

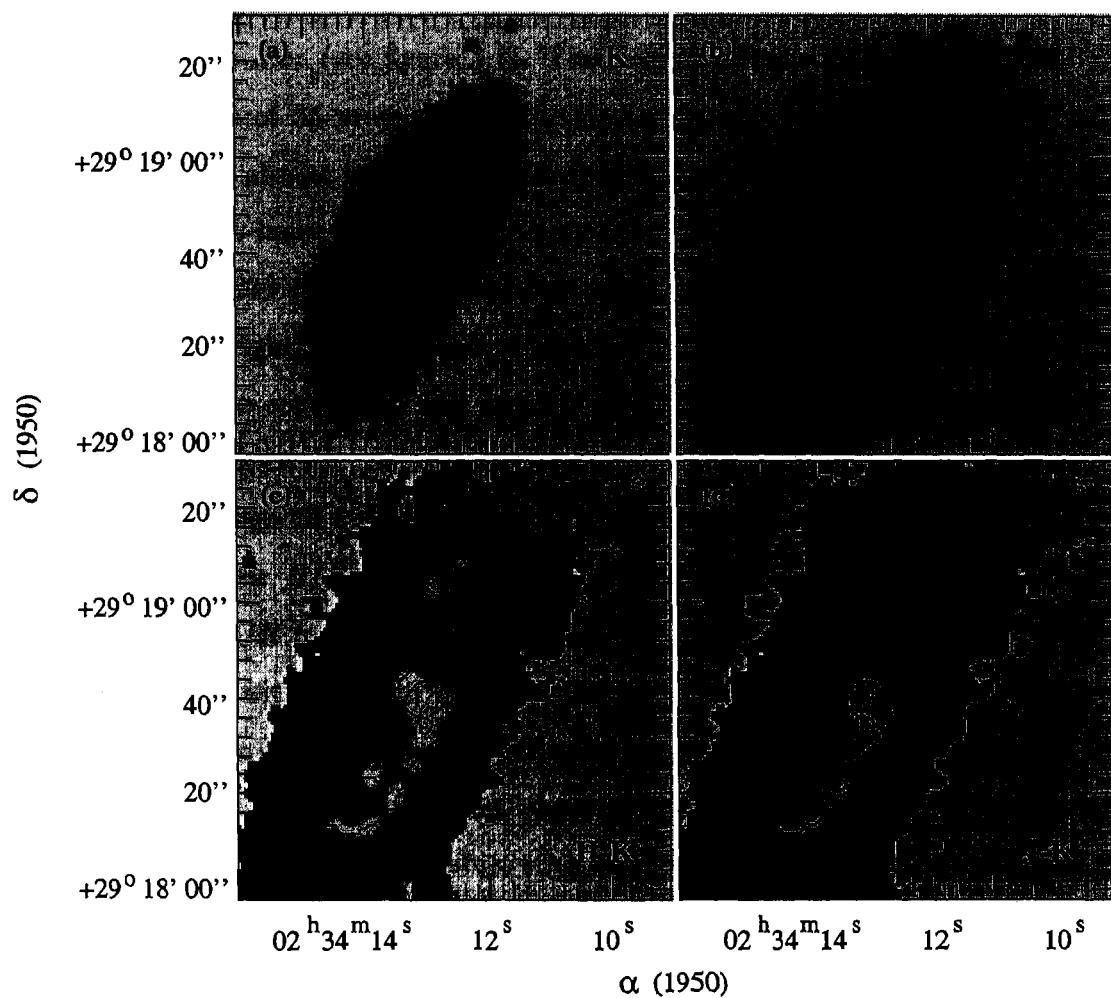


Figure 3.2: Grey scale images of NGC972 in (a) K -band (b) B -band (c) $H - K$ color and (d) $J - K$ color (brighter grey scales correspond to redder colors). Contours of $B - K$ color are superimposed on the color maps and represent the position of the optically seen dust lane.

3.3 Optical–NIR morphology of NGC 972

3.3.1 Spiral structure and dust distribution

On the broad band BVR images, NGC 972 exhibits a very peculiar morphology with complex dust distribution (see figure 3.1). The images reveal a bright nucleus and main body up to a radius of 35 arcsec. Beyond this radius, the outer regions of the galaxy exhibit a fainter and almost featureless light distribution. The inner regions are traversed by a number of dust lanes and this enormous amount of dust, distributed in a random fashion gives NGC 972 the appearance of an irregular galaxy. The broad band images also show a very bright knot located at about 12 arcsec north of the nucleus, which emits strongly in the continuum and appears as bright as the nucleus itself. Since the B image which samples the young hot stars and ionized gas, is more severely affected by the obscuring effects of dust compared to the R image which samples the underlying stellar population, the B/R color maps can be used to emphasize the anomalous dust distribution. The B/R map is shown in figure 3.3. The nucleus is surrounded by dust which forms a ring with a radius of about 630 pc. This is very similar in appearance to the circumnuclear dust ring seen in the color map of NGC 7552 (Forbes *et al.* 1994; fig 5.). On the far side of the nucleus, short plumes of dust are faintly visible in the original image, emanating from the dust ring, towards the north-east direction. Vertical dust filaments and plumes emanating from actively star-forming regions are common in galaxies, and more evident for galaxies with high inclinations. The dust plumes of NGC 972 are not as prominent as in the case of NGC 1808 (Phillips, 1993), and it is not clear if they are off-planar structures.

Two prominent dark lanes which lie along the north-west arm and the south-east arm, roughly trace the spiral structure of the galaxy. These two arms clearly delineate the bright inner region and the faint outer region. Even though the dust appears to be very chaotic on the nearside, the two prominent arms close into a ring on the farther side.

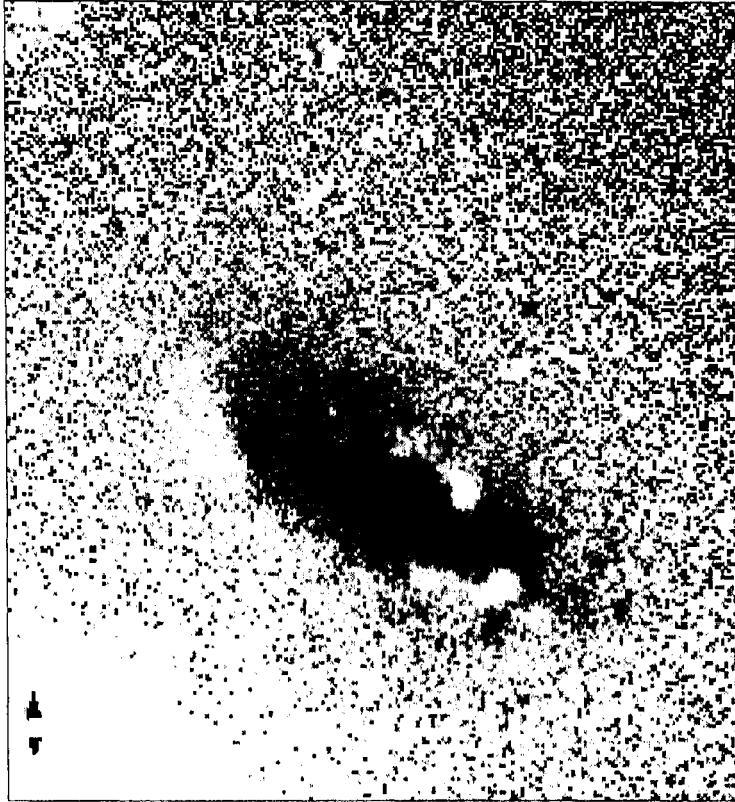


Figure 3.3: B/R color map, emphasizing the complex dust distribution in the main body of NGC 972. North is to the right and east is to the top. The total field is 2.5×2.5 . The red regions appear dark and blue regions appear light.

Comparing with the H_{α} images, it is found that this outer ring encloses all the star-forming knots. Also, it is clear that the dust distribution within this region is closely associated with the distribution of HII regions. The inner dust ring which surrounds the nucleus causes severe obscuration of the circumnuclear HII regions. The bright knot seen north of the nucleus on broad band images, appears quite blue in the color map. From the dust distribution it appears that the southwest side of NGC 972 is the nearside.

The galaxy has a smooth distribution of intensity in the NIR bands as compared to the optical bands. The dust lanes, which are prominent in the B band image are absent

in the K band image. The northwest spiral arm is easily traceable and continuous in all the three NIR bands and coincides in position with that in the B -band. However the southeast stellar arm, which is expected to lie on the leading side of the dusty arm, cannot be traced even on NIR images (see figure 3.2). Instead, a linear spur can be traced on the NIR images on the inner side of the dust lane. The spur lies roughly parallel to the major axis of the galaxy and runs $\approx 5''$ south of the nucleus into the northwest side. The nucleus and the optically prominent HII region on the northwest can both be traced in the NIR bands, with the nucleus relatively brighter than the HII region. A bulge is not apparent on the NIR images. A short bar-like extension along the north-south direction can be seen.

Images in the K -band are least affected by dust and hence are best suited to study the intrinsic components, such as bulge, disk and the spiral arms of galaxies. On the other-hand the B -band images are heavily affected by the dust and hence structural differences between B and K bands can be used to map the distribution of dust. Difference in stellar populations can also lead to structural differences between B and K bands (de Jong 1996). However in dusty galaxies such as NGC 972, the major contribution to the observed structures on color images comes from the non-uniform distribution of dust, rather than the stellar population gradients. Thus it can be assumed that the structures seen in $B - K$ color image of NGC 972, to first order, represent the dust distribution. The $B - K$ contours are shown in figure 3.2 (c) and (d), overlaid on the $H - K$ and $J - K$ greyscale images.

3.3.2 Distribution of the ionized gas

$H\alpha$ imaging effectively traces the distribution of gas photoionized by young OB stars and thereby the sites of recent massive star formation. The continuum subtracted emission line image is shown on a greyscale in figure 3.4.

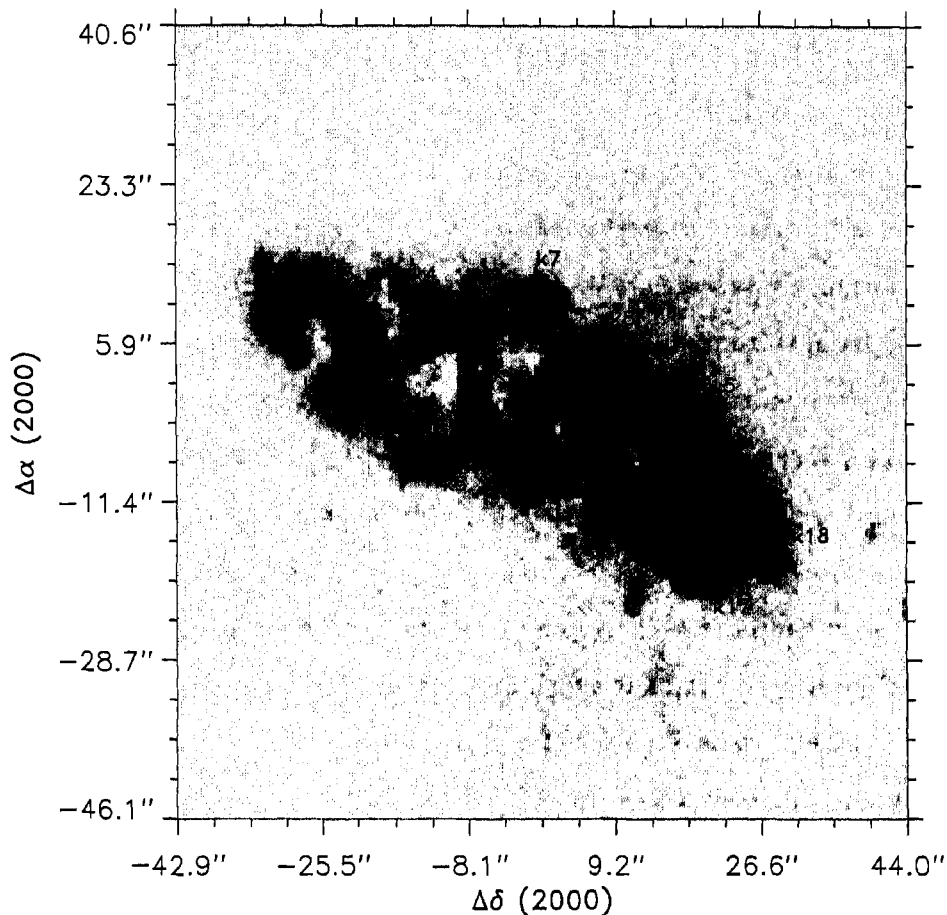


Figure 3.4: Continuum subtracted H_{α} image of NGC 972 reveals the distribution of star-forming regions. The HII regions for which photometry has been performed are marked. The unmarked HII region at the extreme south has not been used in the analysis, since it is too faint in the continuum images. The total field shown here is $1.4' \times 1.4'$. The axes are marked in arcseconds with reference to the nucleus.

Current star formation in NGC 972 is evident from this image which reveals a number of bright, star-forming knots in the nuclear, circumnuclear and disk regions. All the H_{α} knots are confined within a radius of 3.4 kpc. In the continuum image the star-forming regions are hidden from view by the bright stellar bulge as in the case of most early-type galaxies like NGC 3504, NGC 1022, NGC 2782 and NGC 7552 (Devereux & Hameed, 1997). When the dominant contribution from the stellar bulge is subtracted, the star

formation activity becomes evident. The H_α knots in the circumnuclear region form a partial ring of radius 630 pc, with a break south-east of the nucleus. There are five H_α knots (indicated in figure 3.4 as k9, k11, k12, k13, k14) which form the partial ring around the nucleus (k10) while the remaining knots belong to the disk. A comparison of the broad-band images and emission-line image shows that the regions which are bright in the continuum are spatially separated from the regions that are bright in the emission-line image. There is a very prominent HII region in the continuum subtracted H_α image that lies around 16 arcsec north of the nucleus, and is close to the brightest continuum knot seen in broad band images. This giant HII region (labeled k15 in figure 3.4) has extended emission and appears as luminous as the nucleus on the emission-line image, much like the “Jumbo” HII region of NGC 3310 (Balick & Heckman, 1981). We have identified 19 HII regions and performed aperture photometry on them as described in section 3.2. The H_α + $[NII]$ fluxes and equivalent widths given in Table 3.2 have been calculated using the expressions for line fluxes and equivalent widths given by Waller (1990).

The equatorial coordinates for 12 stars seen in our images were obtained from the HST guide star catalogue. Using this information, astrometry was done for the HII regions. The coordinates of the HII regions for J2000 epoch are given in Table 3.4. Knowing the position angle and inclination of the galaxy from RC3, a deprojection of the co-ordinates was done in order to visualize the distribution of HII regions in the plane of the galaxy. It is seen that the circumnuclear knots are contained within an elliptical ring whose major axis is aligned perpendicular to the line of nodes of the galaxy. The deprojected semi-major axis of the circumnuclear ring comes to about one kiloparsec. Though the distribution of the knots is chaotic, it is possible to trace out two spiral arms formed by the disk HII regions.

A comparison of the H_α image with the K band image shows that the star formation extends almost over the entire stellar disk as traced by the outermost K band isophote. Current star formation is active along the northwest spiral arm. HII region population can be traced along the southeast dusty arm as well. Significantly, these HII regions lie on the convex side of the dusty arm, as is expected for a trailing density wave. The

K-band isophotes in the central regions have an oval shape and is elongated along the line connecting the beginning of the spiral arms. This suggests the presence of a weak bar in the galaxy, which seems to end just inside the circumnuclear ring. There is significant amount of star formation in the inter-arm regions of this galaxy.

Table 3.2

Results of aperture photometry of HII regions

ID	Aperture radii(")	<i>V</i>	(<i>B</i> − <i>V</i>)	(<i>V</i> − <i>R</i>)	$\log F_{H\alpha+[NII]}$	W($H\alpha+[NII]$)
k1	1.8	20.54	0.71	0.87	-13.64	618.6
k2	1.8	20.28	0.69	0.76	-13.61	585.0
k3	2.4	18.31	0.78	0.61	-13.44	163.0
k4	1.8	18.15	0.68	0.51	-13.64	96.5
k5	1.8	20.25	1.15	0.89	-13.87	274.4
k6	1.8	18.09	0.97	0.61	-13.97	38.9
k7	1.8	18.36	0.62	0.48	-13.59	134.8
k8	1.8	17.77	0.73	0.49	-13.64	68.3
k9	1.8	18.83	1.07	0.84	-13.82	89.2
k10	1.8	16.61	0.96	0.66	-12.98	93.6
k11	1.8	19.05	1.36	0.93	-13.67	138.2
k12	1.8	18.16	1.37	0.88	-13.67	65.2
k13	1.8	18.71	0.77	0.60	-13.70	128.9
k14	1.8	17.62	0.85	0.56	-13.85	34.4
k15	2.4	16.78	0.66	0.51	-12.79	194.5
k16	1.8	19.28	0.97	0.91	-13.42	310.4
k17	1.8	18.25	0.34	0.34	-13.52	163.4
k18	1.8	18.22	0.74	0.65	-13.29	201.4

3.4 Discussion

3.4.1 Revision of the morphological type of NGC 972

The absence of a bulge on the NIR images calls for a re-discussion of the adopted Sb morphological classification of NGC 972 (Mayya, Ravindranath & Carrasco 1998). In recent years, there have been reports of the absence of classical bulges in galaxies classified as early-type spirals (Carollo et al. 1997). These may either represent pure misclassifications, considering the subjective nature of the classification, or intrinsic limitations of the criteria used in classification. For example, one of the intrinsic limitations was recently demonstrated by Combes and Elmegreen (1993). Using numerical simulation, they found that bar morphology is more tightly related to the dynamical properties rather than the spiral morphology of the galaxy. Thus a bar with early-type properties can be present in a late-type spiral, as was found recently in NGC 6221 by Vega-Beltrán et al. (1998). Historically used classification criteria do not allow for such mixed characteristics in galaxies.

We compiled all the existing global properties on NGC 972 in an attempt to clarify its morphological type. In particular, we aim to establish whether it is a mis-classified galaxy or has mixed morphological characteristics. The compiled data are presented in Table 3.3. The parameters in the upper half of the table are related to the morphological type whereas those in the lower part are related to the starburst properties. The dependence of the listed parameters with morphological type is well established statistically (e.g. Roberts & Haynes 1994). The most likely morphological type for NGC 972, based on each of the observed quantities, is indicated in Col. 3. Principal morphological indicators, namely bulge-to-disk ratio and the pitch angle (of the north-west arm measured on the deprojected K -band image), are clearly inconsistent with the Sb classification. The dynamical mass, as inferred from the rotational speed, is also too small for the Sb classification. The size of the weak bar is almost equal to the exponential scale length — a condition found to be typical in late type galaxies (Combes & Elmegreen 1993).

Table 3.3

Morphological and Starburst properties of NGC 972

Property	Value	Comment	Reference to Col. 2
Bulge/Disk ratio	no bulge	Sd or later	This work
Pitch Angle ($^{\circ}$)	50–60	Sd or later	This work
$V_{\text{rot}}^{\text{max}}$ (km s $^{-1}$)	120	Sc or later	Burbidge et al. (1965)
Mass ($10^{10} M_{\odot}$)	1.2	Sc or later	Burbidge et al. (1965)
M(HI)/M(T)	0.21	Sd or later	Young et al. (1996)
EW(H $_{\alpha}$) (\AA)	36.4	Sc or later	RP98
$B - V$	0.64	Sb or later	RC3
$U - B$	0.07	Sb or later	RC3
Yerkes Type	F3	\sim Sc	Humason et al. (1956)
Mean Type	...	Sd	
L(FIR) ($10^{10} L_{\odot}$)	3.67	$1.15 \times M_{82}$	Young et al. (1996)
$L_{\text{H}\alpha}$ (10^{41} erg s $^{-1}$)	2.95	$0.85 \times M_{82}$	RP98, Young et al. (1996)
SFR (M_{\odot} yr $^{-1}$)	2.64	$0.85 \times M_{82}$	RP98
M(H2)/M(HI)	1.41	$1.70 \times M_{82}$	Young et al. (1996)
M(HI+H2)/M(T)	0.50	...	Young et al. (1996)

Secondary indicators of morphological type such as the neutral hydrogen content and the H $_{\alpha}$ equivalent width (a measure of present to past star formation rate — see Kennicutt & Kent 1983), also suggest a morphological type later than Sc for the galaxy. Observed colors are redder than those found in galaxies of Hubble types Sc and later. However the prominent stellar population, as indicated by the Yerkes type, is not consistent with the red colors, suggesting that the galaxy may have intrinsically blue color typical of late-type spirals, but is reddened by the heavy amount of dust in the galaxy. Thus all the global properties suggest a morphological type later than Sc. The galaxy however has several

peculiarities, the most striking one being the absence of a stellar arm accompanying the dusty arm on the southeast side. Thus the most appropriate morphological type for NGC 972 would be SABd pec.

3.4.2 Star formation history

Evolutionary population synthesis models aim at deriving the observable properties of a population of stars at different times of its evolution. Models for stellar atmospheres and stellar evolution are used to predict the emergent spectrum and other observable parameters for a chosen IMF. Hence, the age of the stellar population can be estimated by comparing the observed quantities with those predicted by the synthesis models.

Before comparing the observables with models, corrections have to be made for the interstellar reddening which arises from three sources — ISM of our Galaxy, ISM of the parent galaxy and the dust mixed with gas within the HII region. For NGC 972, the galactic extinction in the broad bands was obtained using $A_B = 0.37$ from RC3 and the extinction law from Cardelli *et al.* (1989) with $R_v = 3.1$. For the internal extinction within the parent galaxy, a value of $A_B^i = 0.36$ taken from RC3 was used; this also includes correction for the inclination. The spectroscopic ratio, H_α/H_β , gives an estimate of the Balmer decrement which is used to determine the visual extinction A_v within the HII regions. Ho *et al.* (1997) give H_α/H_β as 7.7 for the nucleus of NGC 972 which corresponds to A_v of 2.8 mag. A recent study of HII regions in the centers of nearby galaxies, carried out by Ho *et al.* (1997) yields a median internal reddening of $E(B - V) = 0.54$, using the Balmer decrement for early-type spiral galaxies (S0 to Sbc). Assuming the Galactic extinction law, ($R_v = 3.1$) this implies a visual extinction of $A_v = 1.67$. Thus the nuclear extinction in NGC 972 is higher than the median value of extinction for early-type spirals even after correcting for inclination effects, which account only for 0.4 magnitudes. The observed H_α fluxes are contaminated by the presence of strong [NII] lines at $\lambda 6548 \text{ \AA}$ and $\lambda 6583 \text{ \AA}$, which fall within the 100 \AA wide H_α filter. The pure H_α fluxes are obtained from the observed $H_\alpha + [\text{NII}]$ fluxes by assuming a value of $H_\alpha / (H_\alpha + [\text{NII}]) = 0.70$ based

on the spectroscopic data for the nucleus from Ho *et al.* (1997). This value agrees with the value of 0.72 given by Kennicutt (1983) for typical HII regions.

Table 3.4
Properties of individual HII regions

ID	R.A(hms)	Dec ($^{\circ}$ ' ")	V_0	$(B - V)_0$	$(V - R)_0$	$\log F_{H\alpha}$	$\log L_{H\alpha}$	$\log N_{lyc}$
k1	2 34 13.51	29 18 19.14	18.64	0.07	0.38	-13.33	39.40	51.26
k2	2 34 13.33	29 18 24.21	18.38	0.07	0.27	-13.29	39.43	51.30
k3	2 34 14.02	29 18 21.21	16.41	0.15	0.12	-13.12	39.61	51.47
k4	2 34 14.14	29 18 29.52	16.25	0.05	0.02	-13.32	39.41	51.27
k5	2 34 12.94	29 18 31.12	18.35	0.52	0.40	-13.55	39.17	51.04
k6	2 34 14.06	29 18 37.13	16.19	0.34	0.12	-13.66	39.07	50.93
k7	2 34 14.28	29 18 44.09	16.46	-0.01	-0.01	-13.33	39.40	51.26
k8	2 34 13.88	29 18 50.16	15.87	0.10	0.01	-13.33	39.40	51.26
k9	2 34 13.55	29 18 47.93	15.49	-0.02	-0.03	-13.06	39.66	51.53
k10	2 34 13.45	29 18 42.33	13.27	-0.13	-0.20	-12.23	40.50	52.37
k11	2 34 13.23	29 18 36.73	15.71	0.27	-0.07	-12.92	39.81	51.68
k12	2 34 13.13	29 18 39.77	14.83	0.27	-0.02	-12.91	39.81	51.68
k13	2 34 12.91	29 18 45.51	15.37	-0.32	-0.26	-12.95	39.78	51.64
k14	2 34 13.20	29 18 48.92	14.28	-0.25	-0.30	-13.10	39.62	51.49
k15	2 34 13.25	29 18 59.19	14.88	0.03	0.02	-12.47	40.26	52.12
k16	2 34 12.48	29 18 56.66	17.38	0.34	0.42	-13.11	39.62	51.48
k17	2 34 12.26	29 19 03.58	16.35	-0.29	-0.15	-13.20	39.52	51.39
k18	2 34 12.39	29 19 09.01	16.32	0.11	0.16	-12.98	39.75	51.62

The $H\alpha$ luminosities derived from the fluxes can be used to estimate the current star formation rate by computing the number of Lyman continuum photons that are being emitted by massive stars in the ionization-bounded HII regions. If all of the Lyman continuum photons are absorbed in the photoionization, then for a case B recombination with $T_e = 10,000\text{K}$, the number of Lyman continuum photons is related to the $H\alpha$ luminosity

by,

$$N_l = 7.34 \times 10^{11} L(H_\alpha) \text{ photons s}^{-1} \quad (3.1)$$

where $L(H_\alpha)$ is the luminosity in erg s^{-1} (Kennicutt, 1983).

Table 3.4 gives the extinction corrected colors and H_α fluxes (free from [NII] contamination), H_α luminosities and the number of Lyman continuum photons. The colors and fluxes given in the table were obtained by using the Balmer decrement estimate of $A_v = 2.8$ mag to obtain the internal reddening in the nuclear and circumnuclear regions and using $A_v = 1.3$ mag, which is the typical average extinction for optically selected giant HII regions in spiral galaxies (Kennicutt 1988), to estimate the internal reddening in the disk HII regions.

Table 3.5

<i>Star formation rates for the four brightest HII regions</i>			
ID	Aperture radius(pc)	SFR($\geq 10M_\odot$)	Total SFR
k3	250	0.0163	0.102
k10	190	0.0519	0.325
k15	250	0.0733	0.459
k18	190	0.0227	0.142

The number of Lyman continuum photons emitted by an O5 star is of the order of 10^{49} photons s^{-1} . Hence the number of ionizing O5 stars required in individual HII regions of NGC 972 correspond to 100 - 1000 stars. As seen from the table, most of the HII regions have H_α luminosities that are typical of GEHRs, being in the range of 10^{39} to 10^{40} erg s^{-1} . The nucleus and the most prominent HII region have luminosities comparable to starburst galaxies, with $\log L(H_\alpha)$ value of 40.50 and 40.26 respectively. The number of ionizing photons in the nucleus is given by $\log N_{lyc} = 52.4$ implying the presence of 1000 O5 stars. For comparison, in the case of the starburst region 30 Doradus in LMC, $\log N_{lyc}$ is about 52, for a $\log L(H_\alpha)$ value of 40.2 (Conti, 1991). Table 3.5 gives the estimates of star formation rates (SFR) for four of the brightest HII regions in NGC 972 calculated from

the H_α luminosities, following Kennicutt (1983). The SFR is given by the expression,

$$SFR(\geq 10 M_\odot) = \frac{L(H_\alpha)}{7.02 \times 10^{41} \text{ erg/s}} M_\odot/\text{yr} \quad (3.2)$$

$$SFR(\text{total}) = \frac{L(H_\alpha)}{1.12 \times 10^{41} \text{ erg/s}} M_\odot/\text{yr} \quad (3.3)$$

The observed parameters given in Table 3.4 have been compared to the parameters predicted from the evolutionary synthesis model of Mayya (1995; hereafter M95) for an instantaneous burst characterised by Salpeter IMF with $M_{up} = 100 M_\odot$, $M_{low} = 1 M_\odot$ and slope $\alpha = 2.35$, at solar metallicity. The large uncertainties in the internal reddening within the HII regions makes it difficult to infer the ages of these regions based on the colors. Hence, we have used two different approaches to estimate the ages. In one approach, we used a value of $A_v = 2.8$ obtained from the Balmer decrement seen in the nuclear spectra, for correcting for the internal extinction in the nuclear and circumnuclear star-forming knots. The disk regions were corrected by using a value of $A_v = 1.3$ mag corresponding to the typical extinction value of 1.1 mag at H_α given by Kennicutt (1988) for the HII regions in spiral galaxies. These extinction corrections resulted in colors (see Table 3.4) that were too blue compared to the model colors, and were inconsistent with the ages implied by the measured H_α equivalent widths. The extreme blue colors for the nucleus after correcting for reddening using the Balmer decrement obtained from nuclear spectroscopic ratios, probably implies a different extinction for the stellar and nebular component, as found in several other galaxies. There has been evidence for selective obscuration due to patchy dust distribution in HII regions. The extinction effects of such clumpy dust may be different for stars and ionized gas (Keel 1993, Calzetti *et al.* 1994, Mayya & Prabhu 1996). Mayya & Prabhu (1996) find that dereddening the stellar observed quantities by the extinction derived from Balmer decrement results in an over-correction for extinction towards the stellar component. They infer that the stellar continuum on an average experiences lesser extinction than the nebular continuum, which would be the case if the dust distribution is patchy and the radiation from the ionized gas is selectively absorbed by the dust. Calzetti *et al.* (1994), refer to the discrepancy between the value of extinction obtained from the UV continuum and Balmer line ratios

for their sample of starburst galaxies. In their attempt to derive an effective extinction law, they find that the difference between the optical depths of the continuum underlying the Balmer lines, is about one-half of the difference between the optical depths of the Balmer emission lines.

In our second approach, we grouped the HII regions into three classes based on their location amidst the complex dust lanes which cause non-uniform extinction. The (B/R) color map which reveals the dust morphology was used for this purpose, with the HII region apertures superposed on it. Assuming that the equivalent width is not much affected by the extinction we use the equivalent width of H_{α} versus $(B - V)$ diagrams to obtain an estimate of $E(B - V)$ which would give the color excess over that predicted by the model for the age implied by the equivalent width. It is found that the knots k1, k2, k5, k9, k11, k12, k16 and k18, all of which lie closely associated with dust lanes, have higher average extinction with $A_v = 3.1$. From their location on the dust map, it is evident that all these knots are on the nearside of the galaxy and are seen through the dust lanes. The knots belonging to group II, namely k3, k4, k6, k7, k8, k15 and k17 are located in regions relatively free of dust, on the farside of the galaxy and have lesser average extinction of $A_v = 1.63$. These knots lie in front of the outer dust ring as seen along the line of sight, unlike the knots belonging to group I which are seen through the outer dust ring. Group III consists of the nucleus k10 and two other circumnuclear knots k13 and k14, and they have an average extinction of $A_v = 2.16$. The (B/R) color map also shows that the reddening in these regions is intermediate between that of group I and group II. The colors of the star-forming knots were corrected for the average reddening obtained for the corresponding groups and then compared with model values.

For consistent values of colors and H_{α} equivalent widths, it is seen that the star-forming regions have ages less than 6.5 Myr, with the youngest of them being about 3.2 Myr. The nuclear starburst has an estimated age of 5.4 Myr. Also, the instantaneous star formation scenario can better accommodate the low H_{α} equivalent widths observed, as compared to the continuous star formation scenario, where the continuous availability of ionizing flux results in somewhat higher and nearly constant Balmer equivalent widths. The main

uncertainty in the age estimation comes from the non-uniform reddening over the entire galaxy.

3.4.3 Emission line diagnostics and the nature of activity

We have used the spectra of NGC 972 from the optical spectral atlas for the nuclei of nearby galaxies compiled by Ho *et al.* (1995). The spectra were recorded using the double spectrograph on the Hale 5m telescope which yielded simultaneous spectral coverage of the blue wavelength range 4230 - 5110 Å and the red wavelength range 6210 - 6860 Å . The spectral resolution obtained is 4Å in the blue and 2.5Å in the red. The blue and red spectra of NGC 972 are shown in figure 3.5. The slit was oriented along the minor axis of the galaxy and the slit width was 2 arcsec, and the spectra were extracted over apertures of 2×4 arcsec² which corresponds to about 210×420 pc² at the distance of NGC 972. The nuclear spectrum is typical of starburst galaxies with strong nebular emission lines arising from photoionization by massive stars.

In Table 3.6 we compare the emission-line ratios of NGC 972 with that of other well known starburst galaxies like M82, NGC 253, and NGC 1808 (Armus *et al.* 1989; Phillips 1993; Veron-Cetty & Veron 1986; Forbes *et al.* 1992). The table also contains emission-line ratios for the most prominent HII region in the starburst galaxy NGC 7552 (Forbes *et al.* 1994). From the table it is clear that the emission- line ratios for NGC 972 lie well within the range of values expected for starburst galaxies. The presence of low ionization lines like [OI]λ6300, indicates that there is some amount of shock ionization. The [OI]λ6300/H_α ratio lies within the range of values seen in starburst galaxies which exhibit superwinds (Heckman *et al.* 1990, Armus *et al.* 1989). In spite of its relatively high inclination ($i = 65^\circ$; Tully, 1988), we do not see any extended emission in the H_α emission line image of NGC 972, that is indicative of a superwind. Hence, it is probable that the SNRs present in the starburst region are responsible for the shock ionization giving rise to these low ionization lines.

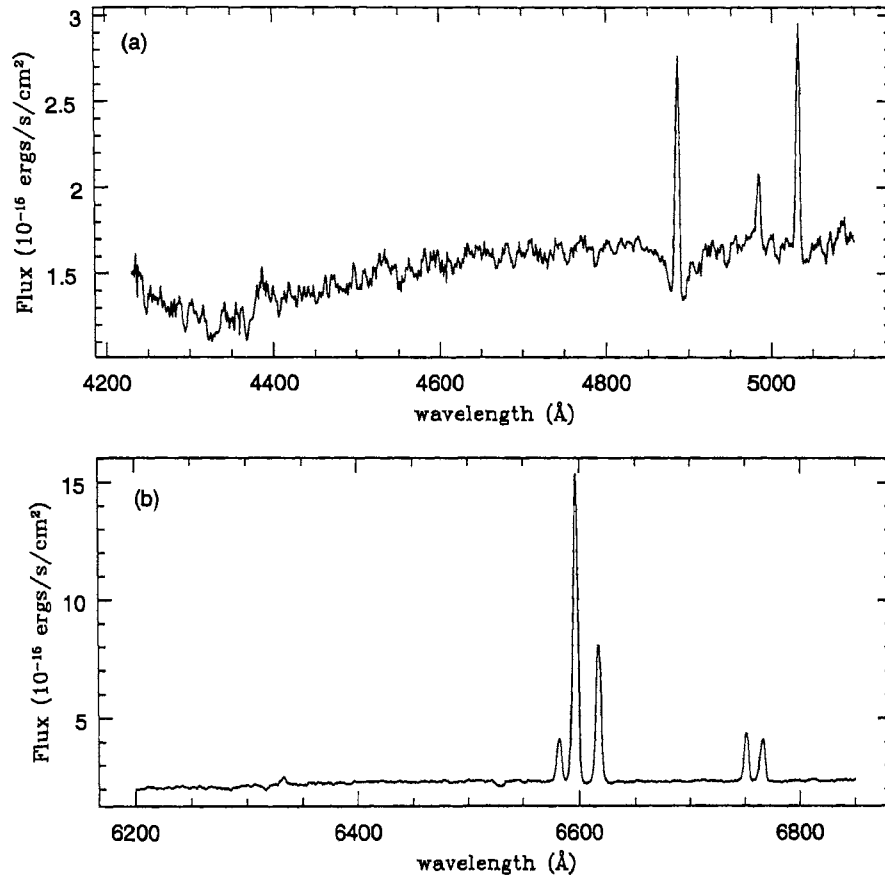


Figure 3.5: Spectra of NGC 972: (a) the blue spectrum (b) the red spectrum from Ho *et al* (1995).

Diagnostic diagrams based on emission-line ratios are very useful for identifying the nature of ionization and for estimating the physical properties of the gaseous nebular emission in galaxies exhibiting spectra with strong emission-lines. These diagrams help in classifying the nuclear spectra of galaxies as HII region-like or AGN-like. When the nuclear emission-line ratios of NGC 972 are plotted on the diagnostic diagrams of Veilleux & Osterbrock (1987), it is evident that the ratios are slightly higher than expected for normal disk HII regions of spiral galaxies and lie in the region occupied by the prototype starbursts.

HII nuclei including starbursts show stronger low-ionization forbidden line emission

compared to normal disk HII regions (Kennicutt *et al* 1989; Ho *et al* 1997). The possible explanations for the enhancement of low-ionization lines include (1) exceptionally hot stars which ionize the nebulae in the nuclear regions where the physical conditions are likely to be different compared to disk regions, (2) shock-ionization from SNRs (3) modification of the thermal properties of HII regions due to the presence of dust in high metallicity environments. We have examined all these likely possibilities in the case of NGC 972.

Table 3.6

Comparison of emission line ratios with other starburst galaxies

Measured ratio	NGC972	NGC1808	NGC3034	NGC253	NGC7552
$\log \frac{[\text{OIII}]\lambda 5007}{\text{H}\beta}$	-0.10	-0.60	-0.46	-	-0.45
$\log \frac{[\text{NII}]\lambda 6583}{\text{H}\alpha}$	-0.37	-0.07	-0.29	-0.11	-0.51
$\log \frac{[\text{SII}]\lambda 6717+6731}{\text{H}\alpha}$	-0.54	-0.66	-0.62	-0.40	-0.58
$\log \frac{[\text{OI}]\lambda 6300}{\text{H}\alpha}$	-1.59	-1.88	-1.77	-1.36	-1.47
$\frac{\text{H}\alpha}{\text{H}\beta}$	7.7	15.0	9.4	-	4.9

In figure 3.6 we indicate the positions occupied by the starburst regions given in Table 3.6, on the emission-line ratio diagrams provided by Rola *et al.* (1997) in which new photoionization models have been used to demarcate the region occupied by HII region nuclei that are powered by massive stars, from the AGNs which are powered by massive black holes. These are dust-free, ionization-bounded models, which give the maximum boundary for gas that is photoionized by OB stars; corresponding to a large range in metallicity ($Z = 0.25 - 2Z_{\odot}$) for $T_{eff} = 50000$ K (dashed line) and $T_{eff} = 60000$ K (solid line). The details of the model are given in Tresse *et al* (1996). Though it is difficult to make a clear distinction between the nuclear HII regions and starbursts, it is evident that both these classes tend to have slightly higher ratios compared to the normal disk HII regions and hence form an upper envelope of the position occupied by HII region-like objects. Knowing the $[\text{OIII}]/\text{H}\beta$ ratio for the nucleus, we estimated the metallicity using the empirical relation given by McCall, Rybski & Shields (1985). We find that O/H for the nucleus is 1.9 times the solar value.

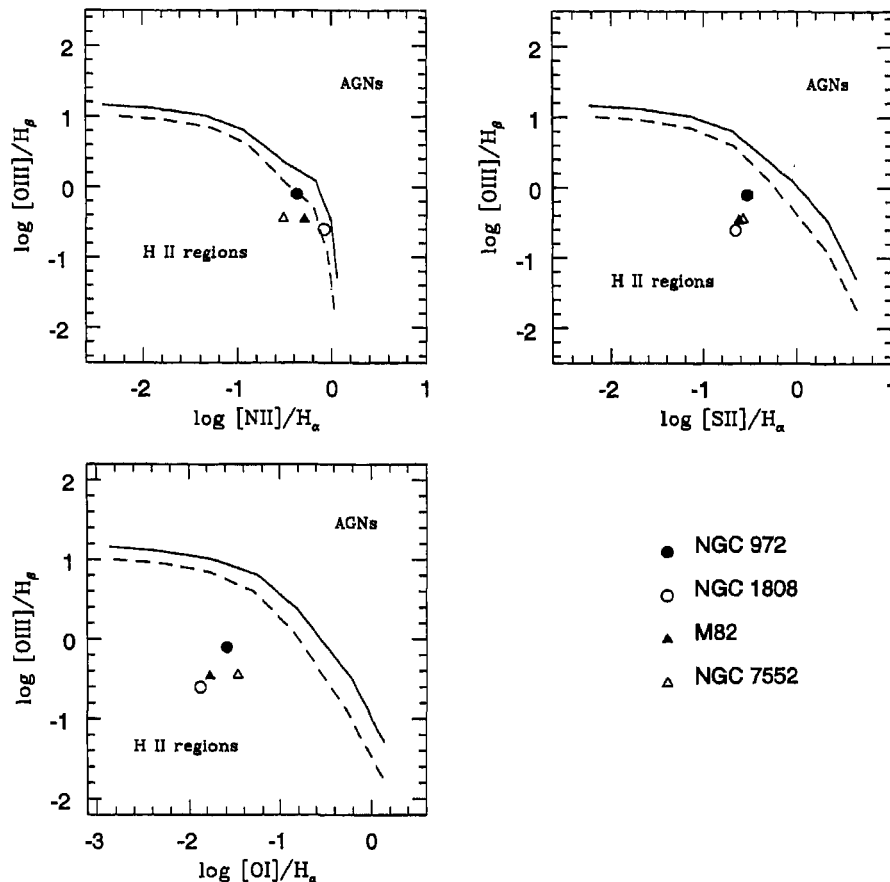


Figure 3.6: Diagnostic diagrams showing the positions occupied by starburst nuclei M82, NGC 1808, NGC 7552 (HII region), and NGC 972. The dashed and solid lines define the separation limits between AGNs and HII galaxies for $T_{eff} = 50,000$ and $60,000$ K, respectively, based on the photoionization models of C. Rola (private communication).

The nuclear spectroscopic data of NGC 972 reveals high metallicity ($Z = 2Z_{\odot}$) and high extinction due to dust ($A_v = 2.8$). Shields & Kennicutt (1995) have studied the consequence of dust on the thermal properties of metal-rich HII regions which are typical of starburst and HII nuclei. Their photoionization calculations show that in the presence of dust, the low-ionization lines are enhanced due to the increase in equilibrium electron temperature, mainly through depletion of gas phase coolants. Using the diagnostic diagrams predicted by the above models which include the effects of dust, we find that the

line ratios for NGC 972 lie well-within the region occupied by starbursts and HII nuclei, for the range of $T = 38000$ K to 45000 K. This does not require exceptionally hot stars as in the dust-free models. Thus it can be concluded that the nuclear emission line spectrum of NGC 972 is a low excitation spectrum produced by photoionization due to massive stars in high metallicity environment, and having low-ionization lines enhanced due to the influence of dust.

As discussed by Forbes *et al* (1994) in the case of NGC 7552, we examined the effects of shock from SNRs on the line ratios. About 20 – 25% contribution from supernova shocks also appear to be a likely alternative to explain the enhancement of low-ionization lines.

3.4.4 Evidence for starburst activity and possible triggering mechanisms

Most of the observational data available on NGC 972 are indicative of the presence of starburst activity in the nucleus. According to the classical definition (Balzano 1983), starburst nuclei have H_α luminosities in the range 10^{40} to 10^{42} erg s⁻¹. From our H_α photometry, we obtain $L_{H_\alpha} = 3.2 \times 10^{40}$ erg s⁻¹ which is in good agreement with a value of 3.6×10^{40} erg s⁻¹ obtained by Ho *et al.* from their spectroscopic data. For comparison, the prototype starburst galaxy M82 has a nuclear H_α luminosity of 1.6×10^{40} erg s⁻¹. Starburst galaxies are characterized by high FIR luminosities and emit most of their bolometric luminosity in the 40 – 1000 μ m range peaking at 60 μ m. The 40 – 120 μ m luminosity is directly related to the SFR and is equal to $2.7 \times 10^{10} L_\odot$ (Devereux & Hameed 1997) in the case of NGC 972, which compares well with the $L(42 - 122\mu m)$ for the starburst galaxies M82 and NGC 253, being $2.32 \times 10^{10} L_\odot$ and $3.04 \times 10^{10} L_\odot$ respectively (Rice *et al.* 1988). The star formation rate obtained from the FIR luminosity, using the conversion given by Devereux & Young (1991) amounts to $2.1 M_\odot \text{ yr}^{-1}$. From our H_α images we estimate an SFR of $2.7 M_\odot \text{ yr}^{-1}$ corresponding to the emission-line flux within an aperture of radius 36 arcsec which encloses all the HII regions. The infrared to blue luminosity L_{IR}/L_B represents the ratio of recent, massive star formation to the

average past star formation. The high value of $L_{IR}/L_B = 2.02$ in the case of NGC 972, is indicative of recent formation of massive stars. As discussed in the previous section, the emission-line ratios are also typical of starburst nuclei, with significant contribution from supernovae via shock heating.

One of the most interesting aspects of starburst phenomena has been the explanation of the triggering mechanisms which induce activity in these galaxies. Observations have shown that interacting galaxies have a higher rate of star formation compared to non-interacting galaxies (Lonsdale *et al.* 1984, Hummel *et al.* 1990). Also barred galaxies have a higher star formation rate than unbarred galaxies (Kennicutt *et al.* 1987, Hummel *et al.* 1990). Most ultraluminous IRAS galaxies show tidal tails, double nuclei and such other features that are evidences for recent merger activity (Sanders *et al.* 1988, Melnick & Mirabel 1990). Thus it appears that an interaction with another galaxy or the recent growth of a bar instability can act as a trigger for inducing activity in galaxies (see Phinney, E.S., 1994 for a review). But NGC 972 appears to be an isolated galaxy that has no obvious signatures of interaction, like tails or any other morphological distortions and there is no evidence for a bar in the optical broad band images. Although the inner regions show disturbed morphology, which is mainly due to the randomly distributed dust lanes, the outer isophotes appear undisturbed. In order to study the morphology in more detail and look for the presence of a bar, it would be necessary to rely on NIR images, which are relatively transparent to dust. Analysis of the NIR images that were obtained do not show very strong evidence for a dominant stellar bar (Mayya, Ravindranath & Carrasco 1997). However, the isophotal twists seen toward the central regions in the K-band are suggestive of a weak bar-like distortion.

Fig. 1 of Vennick & Richter (1994) shows the NGC 972 group of galaxies which contains 7 spirals and irregular galaxies. The group also contains many dwarf spheroidals. Taniguchi (1986), suggested that the starburst activity may have been triggered by merging with a dwarf companion galaxy and the dark dust lanes hold a key to the triggering mechanisms of the galaxy.

There is no galaxy visible on the Palomar Sky Survey prints within 10 times the optical

diameter with a velocity difference less than 1000 km s^{-1} of NGC 972 (Solomon & Sage 1988). The galaxy does not show any obvious signatures of a merger such as tidal tails or bridges. Thus it is safe to assume NGC 972 is an isolated galaxy. Among the isolated galaxies, starbursts are most commonly associated with a strong bar. Absence of a strong bar in NGC 972 calls for invoking alternative mechanisms for triggering the activity in this galaxy. One of such alternative mechanisms is a merger with a low-mass companion object, such as a dwarf galaxy (minor merger).

NGC 972 at present contains an unusually high amount of its mass (50%) in the gaseous form, with the molecular gas mass exceeding the atomic gas mass (Young et al. 1996). Such a high ratio of molecular to atomic gas mass is typical of that found in optically distorted and merging galaxies (Mirabel & Sanders 1989), which gives independent support for a possibly merger-induced starburst activity in this galaxy. NGC 972 group of galaxies contains many dwarf spheroidals (Vennick & Richter 1994) and hence a merger with one of those galaxies in the recent past cannot be ruled out. If that is the case, the merged dwarf spheroidal galaxy had to be gas-rich. However dwarf spheroidal galaxies are normally poor in gas content. On the other hand, small gas clouds (mass less than 10% of the primary galaxy) are known to exist around several galaxies (Schulman, Bregman & Roberts 1994), the most familiar example being the high velocity clouds around our own Milky Way. Accretion of such clouds can naturally enhance the gas mass in the galaxy. As the accreted gas flows to the center of the galaxy, it transforms to molecular form, triggering the intense burst seen in the galaxy. The accretion process is probably responsible for the off-planar nuclear ring. In such a scenario, the plane of the ring may represent the plane in which the gas is being accreted.

NGC 972 is very asymmetric with its northwest arm much stronger than the southeast arm in the stellar continuum. Such an asymmetry is common in late-type galaxies containing a companion (Odewahn 1994). In a recent study, Pisano, Wilcots & Elmegreen (1998) argue that the observed morphological and kinematical asymmetries in the late type galaxy NGC 925 are due to one or many interactions with a companion low-mass galaxy. They discovered an HI cloud of mass $10^7 M_{\odot}$ in the neighborhood of the galaxy,

which they believe is the residual gas cloud resulting from the interactions. Thus it is very likely that the observed asymmetry in NGC 972 is caused by the minor merger of a gas-rich companion, which as we discussed above, can also account for the observed starburst activity, high molecular gas fraction and the off-planar nuclear ring. It however remains to be seen whether gas clouds, such as that found in NGC 925, also surround NGC 972.

3.5 Conclusions

From the BVR and H_α photometry that was carried out on NGC 972, and the spectroscopic data available in the literature, we summarize the following:

The continuum subtracted H_α emission-line image of NGC 972 indicates that most of the activity in this galaxy is concentrated within a radius of 3.4 kpc. The emission line morphology reveals a circumnuclear ring of star-forming knots, with a break south-east of the nucleus. From the B/R and B/K color map a dust ring is found surrounding the nucleus, and this ring causes severe obscuration of the nucleus and circumnuclear star-forming regions.

The H_α luminosities of the individual HII regions are comparable to that of GEHRs. The nucleus and the brightest disk HII region which lies 16 arcsec to the north of the nucleus have luminosities which are typical of starbursts.

The emission line ratios of NGC 972 are typical of starburst galaxies and agree with the spectra produced by photoionization due to massive stars in high metallicity environments. The low-ionization emission-lines are enhanced compared to the normal disk HII regions in spiral galaxies. The enhancement can be explained to be a result of the modification of the thermal properties of the nuclear HII regions by the influence of dust in high metallicity environments. Some contribution from SNRs also appears to be a possible alternative to explain this enhancement of emission-lines.

Using the evolutionary synthesis models of M95, we estimate an age of less than 5.4 Myr for the nuclear starburst. The luminosities and colors are consistent with an instan-

taneous burst model using Salpeter IMF with $M_l=1M_\odot$ and $M_u=100M_\odot$ assuming solar metallicity. The disk star forming regions have colors and luminosities indicating age less than 6.5 Myr. From the H_α luminosity of the nucleus, we infer a star formation rate of $0.32 M_\odot \text{ yr}^{-1}$.

The H_α and IR luminosity over the inner 3.6 kpc radius indicate an SFR of 2.1 – 2.7 $M_\odot \text{ yr}^{-1}$. The high SFR along with the high value of L_{IR}/L_B show that NGC 972 is a starburst galaxy.

We carried out a detailed analysis of the morphological type of NGC 972 using a variety of physical parameters. We favor a morphological type as late as Sd based on the absence of a bulge, high pitch angle of the spiral arm, low dynamical mass and high mass fraction in gas. However, it was classified as Sb and I0 in major astronomical catalogs and atlases, which were mainly guided by the morphological appearance of dust lanes rather than a detailed quantitative analysis such as carried out in our work. The spiral arms are asymmetric with the northwest spiral arm brighter than the southeast spiral in the stellar continuum. The galactic nucleus is undergoing a starburst with a strength comparable to that in M 82. In addition there is active star formation in an off-planar nuclear ring, and the galaxy is extremely gas-rich, especially in molecular form. We propose that all these activities are a result of merger of NGC 972 with a gas-rich companion.

Bibliography

- [1] Andreasyan,N.K.,& Kachikyan,E.E., 1980, *Astrofizika*, 15, 577
- [2] Armus,L., Heckman,T.M, & Miley,G., 1989, *ApJ*, 347, 727
- [3] Balick,B., & Heckman,T.M., 1981, *A&A*, 96, 271
- [4] Balzano,V., 1983, *ApJ*, 268, 602
- [5] Burbidge,E.M., Burbidge,G.R., & Prendergast,K.H., 1965, *ApJ*, 142, 649
- [6] Calzetti,D., Kinney,A.L., & Storchi-Bergmann,T., 1994, *ApJ*, 429, 582
- [7] Cardelli *et al.*, 1989, *ApJ*, 345, 245
- [8] Carollo, C.M., Stiavelli, M., de Zeeuw, P.T., & Mack, J., 1997, *AJ*, 114, 2366
- [9] Casali, M.M., & Hawarden, T., 1992, *The JCMT-UKIRT Facility Newsl.*, 4, 33
- [10] Combes, F., & Elmegreen, B.G., 1993, *A&A*, 271, 391
- [11] Condon,J.J., & Broderick,J.J., 1988, *AJ*, 96, 30
- [12] Conti,P.S., 1991, in *Massive stars in starbursts* , STScI symposium series 5, Ed. Leitherer,C., Walborn,N.R., Heckman,T.M.,& Norman.C.A., Cambridge Univ. press, page 21
- [13] Cruz—Gonzalez, I., *et al*, 1994, *Rev. Mexicana Astron. Astrofis*, 29, 197
- [14] de Jong, R.S., 1996, *A&A*, 313, 377
- [15] Devereux,N., & Hameed,S., 1997, *AJ*, 113, 599

- [16] Devereux,N., & Young,J.S., 1991, ApJ, 371, 515
- [17] de Vaucouleurs,G.*et al.*, 1976,*Second reference catalogue of bright galaxies*, Univ. of Texas press
- [18] de Vaucouleurs,G.*et al.*, 1991,*Third reference catalogue of bright galaxies*, Springer Verlag, New York Inc.(RC3)
- [19] Forbes,D.A. *et al.*, 1994, AJ, 107, 984
- [20] Forbes,D.A., Boisson,C., & Ward,M.J., 1992, MNRAS, 259,293
- [21] Heckman,T.M., Armus,L., & Miley,G.K., 1990, ApJS, 74, 833
- [22] Ho,L., Filippenko,A.V., & Sargent,W.L.W, 1995, ApJS, 98, 477
- [23] Ho,L., 1997, *private communication*
- [24] Ho,L., Filippenko,A.V., & Sargent,W.L.W, 1997, ApJ, 487, 579
- [25] Hodge,P.W., & Kennicutt,R.C, 1983, AJ, 88, 296
- [26] Hummel,E., van der Hulst,J.M., Kennicutt,R.C., & Keel.W.C., 1990, A&A, 236,333
- [27] Keel,W.C., 1993 in *Massive stars: Their lives in the Interstellar Medium*, Ed. Cassinelli,J.P., & Churchwell,E.B. (ASP conf.series, 35), 498
- [28] Kennicutt,R.C., 1983, ApJ, 272, 54
- [29] Kennicutt, R.C., & Kent, S.M., 1983, AJ, 88, 1094
- [30] Kennicutt,R.C.*et al.*, 1987, AJ, 93, 1011
- [31] Kennicutt,R.C., 1988, ApJ, 334, 144
- [32] Kennicutt,R.C., Keel,W.C., & Blaha,C.A., 1989, AJ, 97, 1022
- [33] Knapen, J.H., Beckman, J.E., Heller, C.H., Shlosman, I., & de Jong, R.S., 1995, ApJ, 454, 623
- [34] Krienke, O.K., & Hodge, P.W., 1974, AJ, 79, 1242

- [35] Landolt, A.U., 1992, AJ, 104, 340
- [36] Longo,G., & de Vaucouleurs,A., 1983, *Univ. of Texas Monographs in Astronomy, No.3*, UBV galaxy catalogue.
- [37] Lonsdale,C.J., Persson, S.E., Matthews, K., 1984, ApJ, 287, 95
- [38] Massey,P., *et al.*, 1988, ApJ, 328, 315
- [39] Mayya, Y.D., 1995, AJ, 109, 2503 (M95)
- [40] Mayya, Y.D., & Prabhu, T.P., 1996, AJ, 111, 1252
- [41] Mayya, Y.D., Ravindranath,S., & Carrasco, L., 1998, AJ, 116, 1671
- [42] McCall,M.L., Rybski,P.M., & Shields,G.A., 1985, ApJS, 57, 1
- [43] Melnick,J & Mirabel, I.F., 1990, A&A, 231, L19
- [44] Mirabel, I.F., & Sanders, D.B., 1989, ApJ, 340, L53
- [45] Odewahn, S., 1994, AJ, 107, 1320
- [46] Phillips, A., 1993, AJ, 105, 486
- [47] Phinney, E.S., 1994,in *Mass-transfer induced activity in galaxies*, Ed. Shlosman.I, Cambridge Univ. press, page 1
- [48] Pisano, D.J., Wilcots, W.M.,& Elmegreen, B.G., 1998, AJ, 115, 975
- [49] Ravindranath, S., & Prabhu, T.P., 1998, AJ, 115, 2320
- [50] Rice,W. *et al.*, 1988, ApJS, 68, 91
- [51] Roberts, M.S., 1969, AJ, 74, 859
- [52] Roberts, M.S., & Haynes, M.P., 1994, ARA&A, 32, 115
- [53] Rola, C. *et al.*, 1997 (*Private communication*)
- [54] Sandage, A. & Tammann, G.A., 1981,*A Revised Shapely-Ames Catalogue of Bright Galaxies* , Carnegie Institution of Washington Publ. 635, Washington, DC (RSA)

- [55] Sanders, D.B. *et al.*, 1988, ApJ, 325, 74
- [56] Schulman, E., Bregman, J.B., & Roberts, M.S., 1994, ApJ, 423, 180
- [57] Shields, J.C. & Kennicutt, R.C., 1995, ApJ, 454, 807
- [58] Solomon, P.M., & Sage, L.J., 1988, ApJ, 334, 613
- [59] Spinoglio, L., & Malkan, M.A., 1989, ApJ, 342, 83
- [60] Taniguchi, Y., 1986, PASJ, 38, 571
- [61] Tresse, L. *et al.*, 1996, MNRAS, 281, 847
- [62] Tully, B., 1988, *Nearby Galaxy Catalogue*, Cambridge University Press.
- [63] Vega-Beltran, J.C., *et al* 1998, A&AS, 131, 105
- [64] Vennick, J. & Richter, G.M., 1994, Astron. Nachr., 315, 245
- [65] Veilleux, S & Osterbrock, D.E., 1987, ApJS, 63, 295
- [66] Veron-cetty, M.P., & Veron, P., 1986, A&AS, 66, 335
- [67] Waller, W.H., 1990, PASP, 102, 1217
- [68] Young, J.S. *et al*, 1989, ApJS, 70, 699
- [69] Young, J.S., Allen, L., Kenny, J.D., Lesser, A., & Rownd, B., 1996, AJ, 112, 1903
- [70] Zaritsky, D., Rix, H.-W., & Rieke, M., 1993, Nature, 364, 313

Chapter 4

Properties of the HII regions in NGC 1365 – The luminosity function and size distribution

4.1 Introduction

HII regions are formed in galaxies when the neutral gas surrounding a region of massive star formation is photoionized by the young stars embedded in it. The absorbed radiation is re-emitted during the recombinations which follow the photoionizations, and the H_α line of the Balmer series is the brightest recombination line emitted in the optical. HII regions are very luminous ($L_{H_\alpha} \geq 10^{36} \text{ erg s}^{-1}$), and serve as good probes of star-forming sites in our Galaxy as well as in external galaxies. HII regions provide a wealth of information about the global, current star formation properties in individual galaxies, as well as the physical conditions in the ISM of the host galaxy in regions near its massive star population.

Stars with masses $> 10 M_\odot$ and lifetimes less than 20 Myr are the main source of ionizing flux in young starbursts. The nebular recombination lines effectively re-emit the integrated stellar UV luminosity and provide a direct measure of the star formation rate (SFR). The H_α luminosities of star-forming regions span a large range covering at least

five orders of magnitude. Most of the HII regions in galaxies have H_α luminosities in the range 10^{37} to 10^{39} erg s $^{-1}$, with the faint limit representing HII regions which are ionized by a single star. But Giant Extragalactic HII Regions (GEHRs) and starburst regions like 30 Doradus in LMC, have luminosities in excess of 10^{39} erg s $^{-1}$, while the most luminous starbursts have H_α luminosities in the range 10^{40} to 10^{41} erg s $^{-1}$. These are believed to be ionized by composite radiation from stellar associations containing a large number of massive OB stars. Assuming that the HII regions are ionization-bounded, the H_α flux will be proportional to the number of ionizing stars, and the H_α luminosity function will directly trace the masses of the underlying ionizing stellar cluster, if the initial mass function is similar for the sample regions.

The luminosity function of HII regions provides information on the luminosity and mass distribution of the embedded stellar associations. Kennicutt, Edgar & Hodge (1989; KEH89) studied the HII region populations in 30 galaxies ranging from early Hubble type to late Hubble type in morphology (S – Irr), with an aim to determine the HII region luminosity function, and how the properties of star-forming regions are influenced by the global properties of the galaxies. One of the main conclusions that followed was, the nebular luminosity functions (LFs) in most galaxies are well-represented by a power law of the form;

$$N(L) \propto L^\alpha, \quad (4.1)$$

with $\alpha = -2.0 \pm 0.5$, where $N(L)$ is the number of HII regions with luminosity L . The slope α was also found to be correlated with the Hubble type and ranges from -2.2 for early-type spirals to -1.7 for irregulars. Another feature of the LF, mainly for early-type galaxies, was the turnover around $L_{H_\alpha} = 10^{39}$ erg s $^{-1}$, which roughly marks the transition between normal *Giant* HII regions and *starburst* regions. At luminosities $< 10^{37}$ erg s $^{-1}$ the LFs become shallower, indicating the transition to HII regions ionized by single massive stars. The steeper LF for high luminosity side in the case of early type galaxies indicate that “supergiant” HII regions or “starburst” regions are very rare or absent in these galaxies.

Other studies based on HII region luminosity function include Rand (1992; for M51),

Cepa & Beckman (1990; for NGC 3992), Knapen *et al.*, (1993; for NGC 6814), and Rozas *et al.*, (1996a,b for NGC 157, NGC 3631, NGC 6764, and NGC 6951). Recent studies on HII region LF include Wyder *et al* (1997), Bresolin & Kennicutt (1997), Knapen (1998), Rozas *et al* (1999). Gonzalez Delgado *et al.*, (1997) studied 27 galaxies which host Seyfert/LINER nuclei, in order to study the properties of HII regions and their relation to the Hubble type and the kind of nuclear activity. They find that the LF is well-fitted by a power law with a mean index -2 , and there is no dependence of the slope on the Hubble type. However, according to the level of activity, they find mean slopes of -2.0 , -1.8 , and -2.1 for Seyfert1, Seyfert2 and LINER host galaxies respectively.

Earlier studies have shown that the HII LFs for interarm regions of spiral galaxies show a steeper slope, compared to the HII LFs for the arm regions (KEH89, Rand 1992, Banfi *et al.*, 1993). However, Rozas *et al.*, (1996a,b) and Knapen (1998) do not find such differences between the arm and interarm regions.

Oey & Clarke (1998) carried out Monte Carlo simulations of the HII LF in order to investigate the evolution of the HII LF, through its dependence on the stellar main - sequence lifetimes and ionizing luminosities, in the case of single burst and continuous star formation scenarios. According to their simulations, both evolution and the upper cut-off in the number of ionizing stars N_* can affect the shape of the HII LF. The steeper slope in the earlier Hubble types is attributed to the lower cut-off in maximum N_* . Also, the steeper slope in the case of HII LF for interarm regions is explained in terms of the interarm HII regions being more evolved than those in the spiral arms. This would imply that the interarm is made up of older HII regions whose luminosities have decreased, while most of the newly formed HII regions occupy the spiral arm regions.

Van den Bergh (1981) showed that the size distribution of HII regions in galaxies can be well approximated by an exponential law of the form ;

$$N(> D) = N_0 e^{-D/D_0} \quad (4.2)$$

Where D is the diameter, D_0 and N_0 are constants and N is the number of HII regions with diameter greater than D . KEH89 and Wyder *et al.* (1997) find that such an

exponential form does not really fit the observed size distribution satisfactorily. From their study of HII region sizes for 27 galaxies, Gonzalez Delgado *et al* (1997) find that the size distribution in most cases follows an exponential law. However, for three galaxies in their sample, a broken exponential law was required. Knapen (1998) find that an exponential law fits the size distribution of HII regions in the galaxy M100, very well. Rozas *et al* (1999) have studied the properties of HII regions in NGC 7479, and find that the size distribution of HII regions can be well approximated by the above form.

In this chapter, we discuss the statistical properties of the HII regions in NGC 1365. The HII region identification and preparation of the catalogue is described in section 4.2. The absolute V magnitudes and H_α equivalent widths, the luminosity function, and size distribution of the HII regions, are presented in section 4.3. A discussion of the results is provided in section 4.4 while the main points are summarized in section 4.5.

4.2 The HII region catalogue for NGC 1365

NGC 1365 is one of the most spectacular barred galaxies in the nearby Universe, and belongs to the Fornax cluster of galaxies. It has been classified as SB(s)b I–II by de Vaucouleurs *et al.*, (1991) and has a heliocentric systemic radial velocity of about 1640 km s⁻¹ (Jörsäter & van Moorsel; 1995). Based on the nuclear activity, this galaxy has been classified as Seyfert 1.5 and there are bright HII regions or “hotspots” surrounding the nucleus. (Sersic & Pastoriza 1965; Veron *et al* 1980). Using the Cepheid distance indicator, recent studies with the *Hubble Space Telescope* have determined a distance of 18 ± 2 Mpc to NGC 1365 (Madore *et al*, 1996). At this distance, the image scale corresponds to 88 parsecs per arcsecond.

4.2.1 Observations and reductions

Broad band BVR and narrow band H_α imaging of NGC 1365 was carried out at the prime focus of the Vainu Bappu Telescope on 24 January 1996 and 29 January 1998. The 1024×1024 Tektronix CCD covers a field of 10 arcmin × 10 arcmin at the prime

focus, with an image scale corresponding to 0.6 arcsec per pixel. This field of view covers the entire optical disk of NGC 1365, making it well-suited for the study of global star-formation, and the HII region luminosity function. The spectrophotometric standard star LTT 1788 (Hamuy *et al*, 1996) was observed in the broad band R filter as well as H_α narrow band filter for flux calibration.

Bias subtraction and flat-fielding were done using the procedure *ccdproc* in the standard Image Reduction and Analysis Facility (IRAF) software package. Cosmic-rays were then removed using the task *cosmicrays* available under IRAF. The R band image and H_α image were aligned using the *geotran* and *geomap* tasks available in the reduction software. The alignment was checked using the positions of foreground stars and was found to be better than 0.2 pixels. After cleaning and aligning the images, the continuum R image was subtracted from the H_α image which is contaminated by the continuum. Since the two filters have different bandwidths, it is necessary to scale the R band image before the subtraction, and the scale factor was determined using the foreground stars in the field. The sky subtraction was done and the continuum was subtracted from the H_α image using the method described by Waller (1990). See Chapter 2 for further details of reduction procedure and calibration.

4.2.2 Measurement of H_α fluxes and HII region diameters

We identified 98 HII regions on the continuum subtracted emission line image and performed aperture photometry on them. Isophotal contours were plotted for the individual HII regions and these were used to measure the diameters. The sizes of the individual HII regions were measured as the diameter of the isophote corresponding to a flux level of 2.0×10^{-16} erg cm $^{-2}$ s $^{-1}$ arcsec 2 . This flux level implies a luminosity of 7.0×10^{36} erg s $^{-1}$, adopting a distance of 18.2 Mpc to NGC 1365. According to KEH89, this flux level would correspond to the “Halo” diameters for HII regions or roughly the sizes that one would estimate from a well-exposed photograph. The apertures required for doing photometry were also decided from these measured isophotal diameters. No correction

was applied for the inclination of the host galaxy.

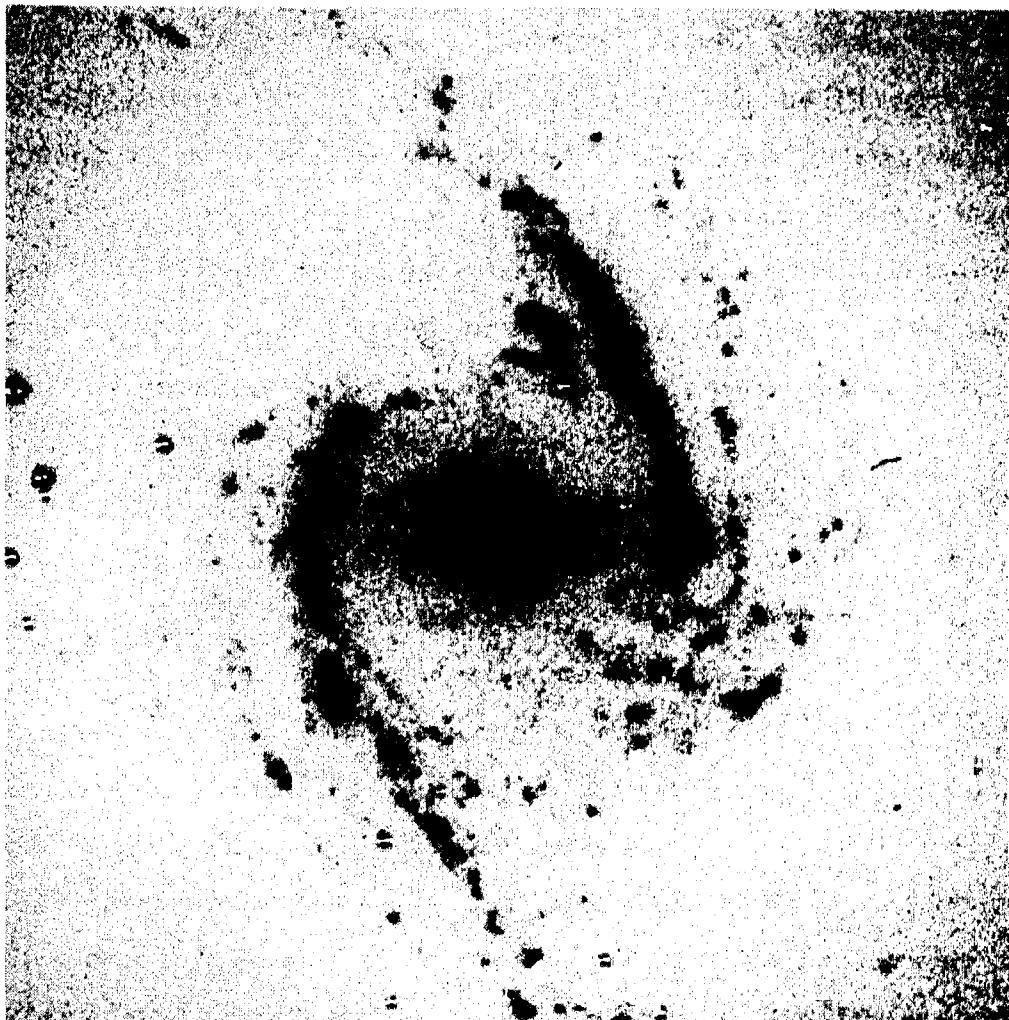


Figure 4.1: The continuum subtracted H_{α} image of NGC 1365. The field shown here covers $8' \times 8'$. North is up and east is left. The residuals of the bright stars can be seen with the intensity peaks subtracted.

The measurement of diameters becomes very difficult, because the effects of poor seeing results in considerable overlap between the "haloes" of adjacent HII regions. We corrected for the effects of seeing by performing a Weiner deconvolution using the Weiner image restoration algorithm available in the *STSDAS* software package. The Weiner algorithm requires a best estimate PSF image to be provided. The PSF was determined from the field stars using the *psf* task in *DAOPHOT*. Before producing the HII region catalogue, the foreground stars were identified and rejected. The stars can be easily identified because they appear as residual peaks in the pure emission line image, due to incomplete subtraction. Strictly, the foreground stars should not appear in the continuum subtracted H_α image, but in cases where the point spread functions are different for the continuum image and the H_α image, or if there are saturated stars, or slight misalignment between the frames, the foreground stars show up as residuals.

We have measured the H_α fluxes and angular diameters of 98 HII regions in NGC 1365. Thereafter, the luminosities and linear isophotal diameters in parsecs were obtained by adopting the Cepheid distance to the galaxy. The H_α luminosities were corrected for Galactic extinction, but not for internal extinction within the host galaxy. The observed H_α fluxes are contaminated by the presence of strong [NII] lines at $\lambda 6548 \text{ \AA}$ and $\lambda 6583 \text{ \AA}$, which fall within the 100 \AA passband of the H_α filter. The [NII] contamination was removed by using $H_\alpha / (H_\alpha + [\text{NII}]) = 0.75 \pm 0.12$ (Kennicutt, 1983), which is the average ratio for disk HII regions in spiral galaxies. The measured quantities like, H_α luminosities, equivalent widths, diameters of HII regions, and absolute magnitudes are given in Table 4.1 along with a representation of the positions of HII regions (figure 4.5), as an appendix to this chapter.

Identifying HII regions and deriving their properties is often complicated due to two reasons. Firstly, the haloes of adjacent HII regions overlap, making it difficult to define the individual HII regions. In such cases, we have identified the peaks and used the contour level which offers the best separation between the regions, as the boundary. Secondly, HII regions are very rarely circular, and mostly have ill-defined edges. Hence, in some cases we may be under-sampling the flux from an HII region by using circular apertures. Also,

the HII region catalogue may not be complete towards the low-luminosity end, mainly due to the detection limit. The faintest HII region detected has $L_\alpha \approx 10^{37}$ erg s⁻¹. However, this should not matter for determining the luminosity function, since the power law fit is performed using the high luminosity end.

4.3 Properties of the HII regions

4.3.1 Absolute magnitudes and H $_\alpha$ equivalent widths

The general properties of the observed HII regions is summarised in figure 4.2. Bresolin & Kennicutt (1997) studied the correlations between various properties of the HII regions in different Hubble types in an attempt to study the variation of the initial mass function (IMF). The various correlations were explained in terms of the evolution of the embedded stellar cluster, the role of the assumed IMF and dependence of the star-formation properties on the Hubble type of the parent galaxy. We have studied these correlations using all the 98 HII regions located in NGC 1365. The maximum H $_\alpha$ equivalent width in the distribution is around $\log \text{EW}(\text{H}_\alpha) = 3.2$ and the maximum luminosity is $\approx 10^{40}$ erg s⁻¹. As the most massive stars evolve off the main sequence, there is a decrease in the total ionizing flux and an increase in the stellar red continuum, as a result of which the equivalent width and the H $_\alpha$ luminosity should decrease. Unlike the results of Bresolin & Kennicutt, we do not see a correlation between the equivalent width, $\text{EW}(\text{H}_\alpha)$ and the H $_\alpha$ luminosity. The large scatter in the plots makes it appear that the correlation is weak, and our luminosity range is also very small to bring out the correlation. The $\text{EW}(\text{H}_\alpha)$ appears to show a weak trend with the absolute V magnitude of the HII regions, and we do see a similar trend in the study by Bresolin & Kennicutt (1997). This trend is rather surprising, with the HII regions of higher absolute V magnitudes having lesser H $_\alpha$ equivalent widths. However, we do not consider this trend as very significant owing to the large scatter in the plot. NGC 1365 is an early-type spiral of the Sb type, and as pointed out by KEH89, it has not many HII regions with luminosities larger than 10^{40} erg

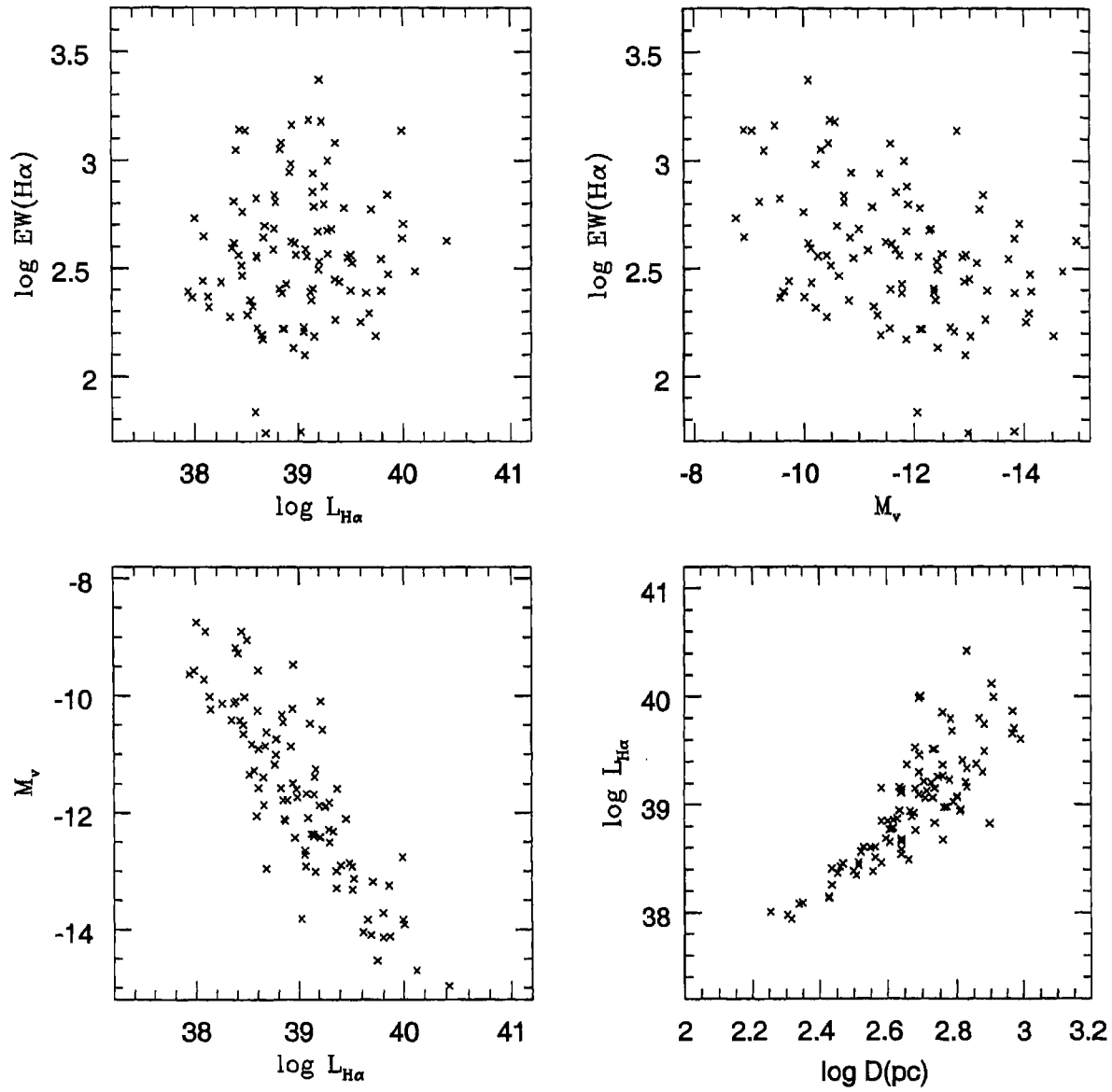


Figure 4.2: Correlations between the observed properties of HII regions

s^{-1} . There is good correlation between the absolute V magnitude and the H_α luminosity. This is likely due to the fact that larger HII regions represent the Strömgren sphere of a larger stellar cluster, containing a larger number of stars distributed according to the IMF. But the brightest regions in our sample have $M_v = -14$, unlike the conclusion by Bresolin & Kennicutt, that the brightest regions are of $M_v = -12.5$.

The diameters of HII regions also show a trend with luminosity like that shown by the absolute magnitude, with the larger HII regions having higher luminosities. In the case of a constant density, ionization–bounded HII region, the strömgren radius scales as the cube root of the ionizing luminosity which is responsible for the observed trend (Osterbrock 1989, Kennicutt 1988). A linear least square fit to the H_α luminosity versus diameter, in logarithmic units, provides a slope of 2.7 ± 0.15 which is close to 3. Thus the correlation between the diameters and Balmer line luminosities are almost consistent with what one would expect for ionization–bounded HII regions.

4.3.2 The HII region luminosity function

The HII region luminosity function for our sample regions in NGC 1365, is shown in figure 4.3. The LFs were constructed by plotting the number of HII regions in each logarithmic bin of 0.2 dex as a function of the H_α luminosity. The faintest regions detected correspond to luminosities of few times 10^{37} erg s^{-1} , and the peak of the LF occurs at $L \approx 10^{38.6}$ erg s^{-1} . The HII region luminosities range from 10^{37} to $10^{40.6}$ erg s^{-1} . We fitted the power law function of the form ;

$$dN(L) = AL^\alpha dL, \quad (4.3)$$

where, $dN(L)$ is the number of HII regions with H_α luminosity between L and $L + dL$ and A is a constant. We obtain $\alpha = -2.29 \pm 0.11$ for the slope of the luminosity function.

This slope is consistent with the LF slopes found for other galaxies of the same Hubble type, namely Sb. NGC 1365 has been assigned the morphological type SB(s)b I–II by de Vaucouleurs *et al.* (1991). For comparison, KEH89 obtained a slope of -2.3 ± 0.2 for M 31 which is of morphological type Sb. This steep slope is explained by the absence

of “supergiant HII regions” or starbursts like 30 Dor in these galaxies. There are lesser number of high luminosity HII regions in early-type galaxies compared to the late systems like Sc–Irr galaxies.

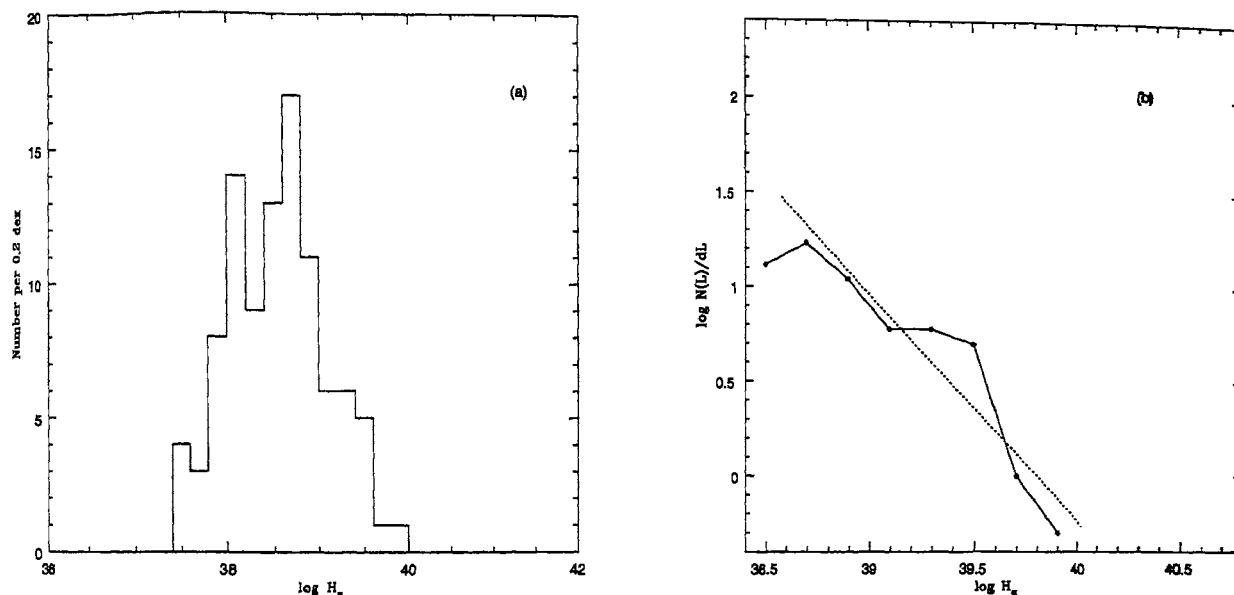


Figure 4.3: HII region luminosity function for NGC 1365. The dotted line in the figure (b) shows the power law fit.

4.3.3 Size distribution of HII regions

The size distribution of HII regions in spiral galaxies have been observed to follow an exponential law of the form ;

$$N(> D) = N_0 e^{-D/D_0} \quad (4.4)$$

Where D is the diameter, D_0 and N_0 are constants and N is the number of HII regions with diameter greater than D (Van den Bergh 1981; Hodge 1987). Earlier studies by KEH89, and Wyder *et al.*(1997), concluded that the above exponential form did not satisfactorily fit the observed diameter distribution. However, we find that our data can be approximated by an exponential law of the above form (see figure 4.4). We obtain $D_0 = 158$ pc, similar to the values obtained by other authors; Cepa & Beckman (1990)

obtained $D_o \approx 128$ pc for NGC 3992 and NGC 4321, and Banfi *et al* (1993) obtained mean $D_o = 165$ pc for their sample of 22 spiral galaxies in the Virgo cluster. We obtain $N_o = 500$, and the constants we derive from the fit may well be affected by our HII region detection limits. However, from the very small scatter in our figure, it appears that the above exponential form does really represent the data sample very well.

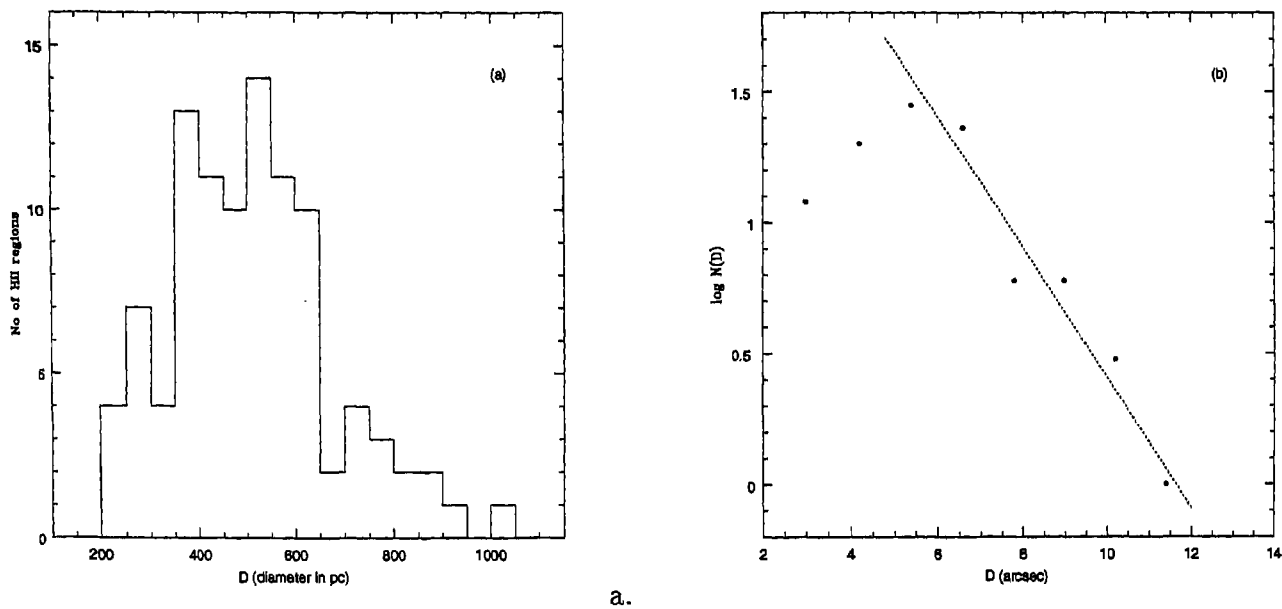


Figure 4.4: Size distribution of HII regions in NGC 1365. Figure (b) shows the exponential function fit, for the larger diameter side of the distribution.

The size distribution is shown in figure 4.4b, along with the best linear least square fit. The peak of the diameter distribution occurs at $\approx 450 - 500$ parsecs. The smallest sizes we see in our sample are $2''$ which corresponds to 176 parsecs. We have corrected for the seeing using the Weiner algorithm, but there is a need to study the effects of seeing and the completeness of our sample at the small size limits. In the case of some of the largest HII regions, the inner contours show multiple cores, which could be resolved in some cases. These were considered as separate regions. But where the overlap is too large, we may have over-estimated the diameters.

4.4 Discussion

A study of the HII region luminosity function in NGC 1365 has shown that the slope of the HII region luminosity function is consistent with that expected for early-type spirals. As seen from figure 4.3, the peak of the luminosity function occurs at $\log L_{H\alpha} = 38.6$ erg s^{-1} . A number of spiral galaxies are known to have a break, or a change of slope at this luminosity, and this has often been interpreted as the turnover from ionization–bounded HII regions to density–bounded HII regions (Rozas *et al* 1996a,b; Rozas *et al* 1998). In cases where such a break is seen, it has been possible to fit the luminosity function with two segments of different slopes – a shallow slope for $\log L_{H\alpha} < 38.6$ and a steeper slope for $\log L_{H\alpha} > 38.6$. KEH89 found that six galaxies in their sample required such composite power laws to fit the luminosity function, and these were termed as “type II” LFs. The break in the HII LFs for these galaxies occurred mostly around the luminosity $\log L_{H\alpha} = 38.6$, which corresponds to the peak luminosity for most early–type galaxies. Thus, KEH89 concluded that this value of the peak luminosity represents a transition from normal “giant” HII regions like those in our Galaxy to “Supergiant” HII regions or Starbursts like 30 Doradus in LMC. The steeper slopes in early–type galaxies seemed to indicate that some physical mechanism prevents the formation of supergiant HII regions in these galaxies.

Oey & Clarke (1998) have tried to explain the observed variations of HII LFs with the Hubble type based on evolutionary effects and the maximum number of ionizing stars per cluster. The HII regions we have detected in NGC 1365 have luminosities ranging from 10^{37} to 10^{40} erg s^{-1} , which corresponds to Lyman continuum luminosities of $\approx 10^{49}$ to 10^{52} ionizing photons per second. A single star of the most luminous O5V type, produces about 5×10^{49} Lyman α photons per second. This implies that most of the HII regions are ionized by a few to few hundreds of massive stars. As the embedded stellar cluster evolves, the most massive stars leave the main sequence, which results in a decrease in the number of ionizing photons and hence a decrease in the $H\alpha$ luminosity. Such evolutionary effects have been successful in accounting for the steeper slopes often reported for HII LFs in the

interarm regions compared to arm regions in a particular galaxy. A clear interpretation of the HII LF would certainly require more parameters, in order to confirm whether the behaviour of HII LFs in different Hubble types, or different regions of a spiral galaxy are the result of evolutionary effects or due to lower cutoffs in the number of ionizing stars. A study of the ages of the clusters based on more observables like colors, equivalent widths etc would be required to confirm the effects of evolution.

The steeper slopes seen in early-type galaxies, as in the case of NGC 1365, however, are better understood in terms of the lower cutoffs in the number of ionizing stars in the clusters. KEH89 have shown that early-type galaxies have fewer stars per cluster, since the mean nebular luminosities in these galaxies are substantially lower than for late-type galaxies, even though they have a large number of HII regions. The large differences in the HII region population along the Hubble sequence, seem to reflect the mass distributions of the interstellar atomic and molecular clouds in the host galaxies. KEH89 have also emphasised the similarity between the form of the HII LFs and luminosity functions of Galactic open clusters and mass functions of giant molecular clouds.

The quantity D_o derived from an exponential fit to the diameter distribution (see equation 4.4), is referred to as the “characteristic” diameter and is related to the properties of the host galaxy. Hodge (1987) found an excellent correlation between the absolute magnitude of galaxies and the size scales D_o , and a least square fit yielded the relation;

$$\log D_o = -1.20 - 0.163 M_B \quad (4.5)$$

In the case of NGC 1365, D_o has a value close to that predicted by the above D_o versus luminosity relation provided by Hodge. With $M_B = -21.20$ (from RC2), the above relation predicts $D_o = 180$ for this galaxy which is close to the value $D_o = 158$ which we obtain from the exponential fit. It has been observed that irregular galaxies have larger values of D_o , for a given M_B , compared to spiral galaxies. This has been interpreted as the result of different gas dynamics in the disks of these galaxies of different Hubble types. Spiral density waves may be instrumental in preventing the formation of large scale gas condensations, which can easily form in dynamically quiescent irregular galaxies.

From figure 4.2, we find that the luminosity versus radius of HII regions (in logarithmic units), has a slope close to 3 when a simple linear least square fit is performed, implying that these regions are ionization-bounded. Even though the figure shows large scatter at higher luminosities, it is clear that there is an upward trend and an increasing slope at higher luminosities. This is what would be expected if the higher luminosity HII regions are density-bounded. Such a trend has been noticed earlier, in the studies by Rozas *et al* (1996) and Rozas *et al* (1999). The large scatter in figure 4.2 at high luminosities is probably due to regions which have multiple cores, or have contribution from neighbouring HII regions whose haloes overlap.

4.5 Conclusions

In this chapter we have presented the results of a statistical study of the HII regions of NGC 1365. The main points are summarized below;

- We have catalogued 98 HII regions and obtained the HII region luminosity function. The slope $\alpha = -2.29 \pm 0.11$, obtained for the LF, is consistent with what is expected for galaxies of similar Hubble type. The steeper slope can be explained by the lack of “supergiant” HII regions or starburst regions in galaxies of early Hubble type. In other words, this implies a lower number of ionizing stars in the embedded stellar clusters.
- We find that the size distribution can be well fitted by an exponential law. The “characteristic” diameter D_0 derived from the fit, agrees well with the values derived for other galaxies of similar Hubble type by other studies. Also, the value of D_0 is close to that predicted from the correlation between “characteristic” diameter versus luminosity of the host galaxy, suggested by Hodge (1987).
- A simple linear least square fit to the luminosity versus radius of the HII regions, in logarithmic units, yields a slope close to 3, which is what is expected for ionization-bounded HII regions. However, at higher luminosities, there is an upward trend

indicating a deviation from this relation. This probably indicates that the higher luminosity HII regions are density-bounded.

- From the steep slopes of the HII LF and the small “characteristic” diameters for the early-type spirals, it appears that some dynamical phenomena (like spiral density waves) are responsible for inhibiting the formation of large star-forming complexes in these galaxies.

Even though the HII regions serve as good probes for studying the global star formation in galaxies, it has a few limitations. The H_α emission samples only the massive star population, and hence the information obtained is mostly about the upper IMF. Observations down to the low mass limit will be necessary to sample the whole mass range implied by the IMF. Also, HII regions have dust associated with them, which is responsible for internal extinction in these regions. Hence, some of the systematic trends that are seen could also be an effect of the differing extinction. A more complete understanding of the differences in the star-forming properties along the Hubble sequence would require the atomic and molecular gas distributions to be studied in addition to the ionized gas sampled by H_α emission.

Bibliography

- [1] Banfi, M., et al., 1993, A&A, 280, 373
- [2] Bresolin, F., & Kennicutt, R.C., 1997, AJ, 113, 975
- [3] Cepa, J., & Beckman, J.E., 1990, Ap&SS, 170, 297
- [4] de Vaucouleurs, G., de Vaucouleurs, A., Corwin, H.G., *et al.*, 1991, Third Reference Catalogue of Bright Galaxies, Springer, New York
- [5] Gonzalez - Delgado, Rosa. M., et al., 1997, ApJS, 108, 199
- [6] Hamuy et al., 1994, PASP, 106, 566
- [7] Hodge, P.W., 1987, PASP, 99, 915
- [8] Jörsäter, S., & Moorsel, G.A., 1995, AJ, 110, 2037
- [9] Kennicutt, R.C., 1983, ApJ, 272, 54
- [10] Kennicutt, R.C., 1988, ApJ, 334, 144
- [11] Kennicutt, R.C., Edgar, B.K., & Hodge, P.W., 1989, ApJ, 337, 761 (KEH89)
- [12] Knapen, J.H., Arnth-Jensen, N., Cepa, J., Beckman, J.E., 1993, AJ, 106, 56
- [13] Knapen, J.H., 1998, MNRAS, 297, 255
- [14] Madore, B.F., et al, 1998, Nature, 395, 47
- [15] Oey, M.S., & Clarke, C.J., 1998, AJ, 115, 1543

- [16] Osterbrock, D.E., 1989, *The Astrophysics of Gaseous Nebulae and Active Galactic Nuclei* (Mill Valley, CA: University Science Books)
- [17] Rand, R.J., 1992, *AJ*, 103, 815
- [18] Roy, J.-R., & Walsh, J.R., 1997, *MNRAS*, 288, 715
- [19] Rozas, M., Beckman, J.E., & Knapen, J.H., 1996a, *A&A*, 307, 735
- [20] Rozas, M., Knapen, J.H., & Beckman, J.E., 1996b, *A&A*, 312, 275
- [21] Rozas, M., Zurita, A., Heller, C.H., & Beckman, J.E., 1999, *A&A Suppl. Series*, 135, 145
- [22] Sersic, J.L., & Pastoriza, M., 1965, *PASP*, 77, 287
- [23] van den Bergh, S., 1981, *AJ*, 86, 1464
- [24] Veron, P., Lindblad, P.O., Zuiderwijk, E.J., Veron, M.P., & Adam, G., 1980, *A&A*, 87, 245
- [25] Waller, W.H., 1990, *PASP*, 102, 1217
- [26] Wyder, T.K, Hodge, P.W., & Skelton, B.P, 1997, *PASP*, 109, 927

Appendix A:

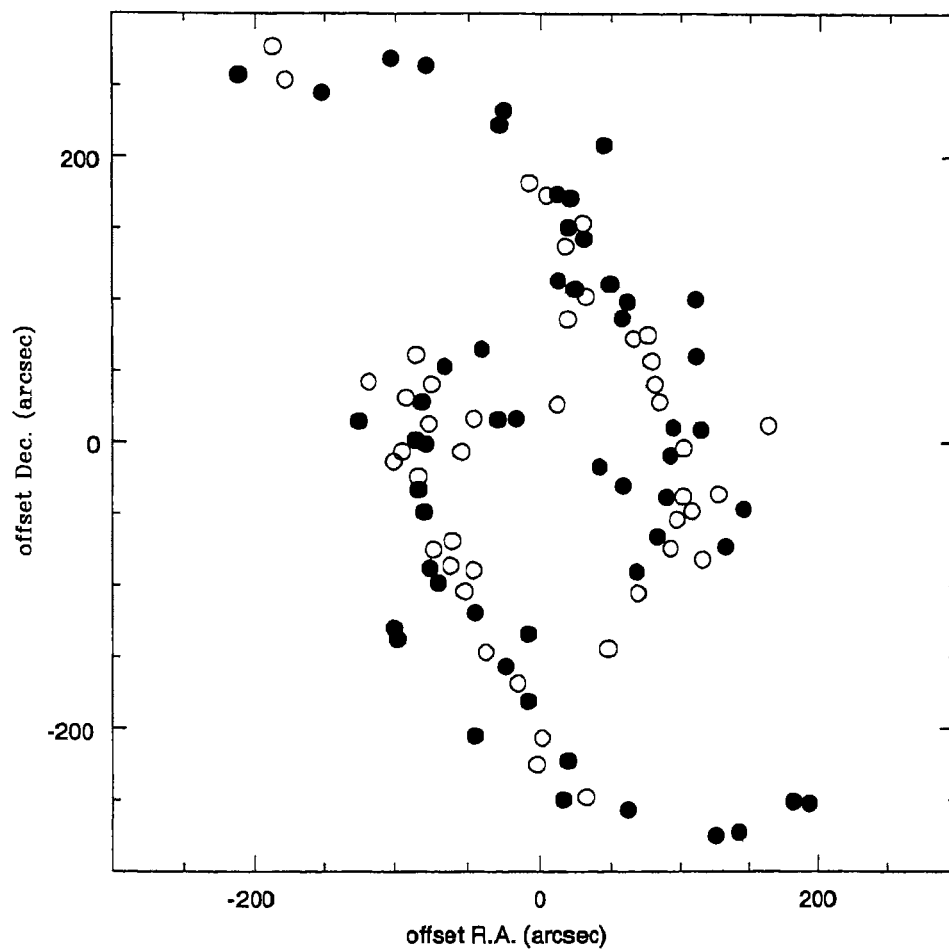


Figure 4.5: Representation of the positions of the HII regions. The filled circles show the HII regions identified by Roy & Walsh (1997) for a spectroscopic study. The open circles are the additional HII regions identified in the present work. Coordinates of the centre of the image are $RA = 03^h33^m36.6^s$ and $Dec = -36^\circ08'17.0''$ (J2000).

Appendix A:

Table 4.1

Properties of the HII regions in NGC 1365

ID	X''	Y''	H α Eq.wds	logL H_{α}	D(parsecs)	M V
1	211.3	257.4	440.29	38.67	572.88	-10.847
2	152.4	245.1	254.05	38.82	791.12	-11.573
3	103.4	268.7	412.80	38.97	578.33	-11.596
4	79.3	263.5	233.99	38.13	267.34	-10.015
5	25.5	232.5	483.00	38.77	403.74	-11.000
6	28.4	222.5	420.07	38.93	643.80	-11.493
7	-12.3	174.1	468.90	39.20	534.68	-11.870
8	-21.4	171.4	125.53	39.06	632.89	-12.910
9	-19.8	150.9	161.51	39.06	512.86	-12.713
10	-30.1	142.8	255.62	39.14	480.12	-12.360
11	-49.0	111.1	306.16	40.11	802.03	-14.703
12	-12.9	113.4	281.62	39.37	452.84	-12.993
13	-24.4	107.6	691.36	39.85	572.88	-13.247
14	-60.6	98.5	248.06	39.79	736.56	-14.137
15	-44.4	208.4	1110.16	38.40	272.80	-9.271
16	-109.3	100.2	364.26	38.42	289.16	-10.414
17	-56.5	87.1	153.97	39.74	763.84	-14.529
18	-109.7	60.1	641.92	38.78	414.65	-10.732
19	-113.3	8.7	626.16	39.26	556.51	-11.892
20	-93.5	10.1	350.35	39.79	605.61	-13.713
21	-91.3	-9.0	249.72	39.51	540.14	-13.318
22	-41.5	-16.7	1511.48	39.23	600.16	-10.575
23	-57.3	-30.2	362.07	38.59	354.64	-10.259
24	-88.6	-38.2	1453.36	38.94	431.02	-9.469
25	-145.2	-46.6	883.30	38.92	474.67	-10.865

Appendix A:

Table 4.1 (continued)

Properties of the HII regions in NGC 1365

ID	X''	Y''	H $_{\alpha}$ Eq.wds	logL $_{H_{\alpha}}$	D(parsecs)	M $_V$
26	-132.2	-72.5	474.61	39.29	491.04	-12.284
27	-67.5	-90.3	1204.78	39.37	720.19	-11.582
28	-81.7	-65.7	167.30	38.60	338.27	-11.564
29	16.5	16.7	424.66	40.42	676.54	-14.968
30	29.2	15.8	997.19	39.29	491.04	-11.822
31	40.5	65.4	341.17	39.20	671.08	-12.411
32	66.2	53.3	508.98	40.00	496.49	-13.914
33	82.2	28.5	357.48	39.49	763.84	-12.862
34	125.9	14.6	266.95	38.88	469.21	-11.785
35	79.5	-1.0	873.28	39.15	381.92	-11.379
36	86.7	1.9	226.07	39.14	436.48	-12.399
37	84.5	-32.9	435.69	39.99	812.94	-13.830
38	80.2	-48.5	609.84	39.16	431.02	-11.250
39	76.8	-87.9	334.88	39.52	480.12	-13.126
40	70.7	-98.1	365.73	39.51	545.60	-12.920
41	45.1	-118.9	1370.68	39.98	491.04	-12.761
42	101.0	-129.6	370.76	39.30	752.92	-12.503
43	98.6	-137.4	757.97	39.26	572.88	-11.878
44	8.3	-133.8	360.73	39.09	491.04	-12.082
45	23.7	-156.5	178.42	39.61	982.08	-14.048
46	7.8	-180.6	243.24	38.84	398.28	-11.784
47	44.9	-204.7	386.25	38.76	480.12	-11.173
48	-20.2	-222.5	210.96	38.56	332.81	-11.274
49	-16.9	-249.7	593.89	39.70	938.43	-13.180
50	-62.1	-256.9	245.03	39.65	927.52	-13.826

Appendix A:

Table 4.1 (continued)

Properties of HII regions in NGC 1365

ID	X''	Y''	H α Eq.wds	logL $_{H\alpha}$	D(parsecs)	M $_V$
51	-125.0	-274.8	148.25	38.65	436.48	-11.864
52	-142.3	-272.4	497.31	38.68	392.83	-10.610
53	-181.8	-250.9	247.62	37.93	207.32	-9.634
54	-193.3	-252.2	292.40	38.46	381.92	-10.648
55	178.6	253.8	414.69	38.38	360.09	-10.086
56	187.2	277.0	1371.07	38.49	458.30	-9.044
57	7.8	181.8	326.94	38.45	294.62	-10.492
58	-4.2	173.3	246.44	39.12	518.32	-12.357
59	-29.6	153.7	168.87	39.06	540.14	-12.643
60	-19.0	86.4	2350.89	39.21	507.40	-10.087
61	-65.4	72.8	55.49	39.02	616.52	-13.810
62	-75.5	75.4	165.88	38.85	414.65	-12.105
63	-78.2	57.0	54.80	38.68	436.48	-12.952
64	-80.2	40.8	274.85	39.41	654.72	-12.898
65	-83.3	28.4	296.68	39.86	927.52	-14.116
66	-101.1	-4.1	312.52	39.20	534.68	-12.429
67	-162.9	12.1	1200.53	38.84	381.92	-10.451
68	-126.2	-36.2	365.14	38.98	589.24	-11.735
69	-107.0	-48.0	389.07	39.07	632.89	-11.666
70	-96.3	-53.9	1121.82	38.83	545.60	-10.325
71	-91.7	-74.0	689.58	38.77	409.2	-10.736
72	-114.7	-81.8	481.77	39.33	676.54	-12.319
73	-68.6	-105.1	579.38	38.46	327.36	-10.008
74	-12.4	26.7	68.36	38.58	436.48	-12.054
75	46.4	16.5	192.57	38.51	365.55	-11.339

Appendix A:

Table 4.1 (continued)

Properties of HII regions in NGC 1365

ID	X''	Y''	H $_{\alpha}$ Eq.wds	logL $_{H_{\alpha}}$	D(parsecs)	M $_V$
76	54.5	-6.4	188.53	38.34	321.90	-10.418
77	86.5	61.5	541.41	38.00	180.04	-8.750
78	118.7	42.4	354.80	38.60	365.55	-10.903
79	92.8	31.4	959.66	38.93	463.76	-10.224
80	95.4	-6.2	155.86	38.65	403.74	-11.391
81	101.4	-13.2	135.79	38.95	649.26	-12.424
82	61.0	-68.8	1383.95	38.43	327.36	-8.894
83	74.2	-74.9	182.72	39.37	572.88	-13.290
84	62.1	-86.0	666.86	38.60	354.64	-9.567
85	52.3	-103.9	225.62	38.53	436.48	-10.824
86	37.4	-146.5	165.99	38.86	425.56	-12.139
87	14.9	-168.2	153.69	39.16	676.54	-13.005
88	-1.6	-206.1	645.34	38.38	316.44	-9.176
89	1.7	-224.8	442.40	38.08	223.69	-8.908
90	-32.3	-247.8	272.38	38.25	272.8	-10.133
91	-47.9	-143.9	276.06	38.07	218.24	-9.727
92	-17.8	-136.5	393.07	38.36	283.71	-10.125
93	46.4	-89.0	232.51	37.97	201.87	-9.576
94	-100.9	-37.8	208.41	38.14	267.34	-10.228
95	75.7	40.8	1538.86	39.11	436.48	-10.477
96	77.5	12.9	196.46	39.68	611.07	-14.093
97	84.6	-23.7	604.22	39.45	491.04	-12.105
98	-31.6	102.3	716.16	39.15	545.6	-11.681

Chapter 5

The nebular properties and stellar populations of starburst nuclei

5.1 Introduction

A starburst galaxy is characterized by a very bright nucleus which emits strong, narrow emission lines similar to low-ionization HII region spectra. The emission line spectrum is a result of the photoionization of the surrounding gas by ultraviolet radiation from hot, young massive OB stars. The radiation emitted by a gaseous nebula depends on the local ionization, density and temperature, and the nature of the radiation field. The most prominent spectral features are the emission lines of various ionization species of different elements, which are essentially either recombination lines or collisionally excited lines. The latter arise from levels which differ from the ground level only by a few volts, and can therefore be excited by collisions with thermal electrons. These collisionally excited lines, specially those seen in the optical region are also called forbidden lines, because, for any given ion, all the excited levels which are within a few volts above the ground level, have the same electronic configuration as the ground level itself, and thus radiative transitions are forbidden by the parity selection rules. The most important emission lines seen in the optical spectra of HII regions include, [OII] $\lambda\lambda$ 3726,3729, [OIII] $\lambda\lambda$ 4959,5007,

[OI] $\lambda\lambda$ 6300,6363, [NII] $\lambda\lambda$ 6548,6583, and [SII] $\lambda\lambda$ 6717,6731.

Apart from these collisionally excited lines, the spectra of HII regions are characterized by the recombination lines of H I, He I, and He II. These are produced when the electrons which are captured to the excited states of an atom cascade down to the ground level through downward radiative transitions to different lower excitation levels. Therefore, these line radiations are essentially the result of bound-bound transitions in the atom. The emergent line intensities depend on whether the HII region nebulae are optically thin, or optically thick. Thus, there are two assumptions that follow; and are referred to as Case A and Case B in the theory of recombination line radiation. In Case A, it is assumed that all the line photons that are emitted in the nebula escape without absorption and therefore without causing further upward transitions. This would require that the nebula is optically thin in all H I resonance lines, and contain only a small amount of gas making them too weak to be observed. In Case B, it is assumed that every Lyman-line photon is scattered many times and is converted into lower series photons (like, the Balmer series) and a Lyman- α photon. Thus during the cascade, every Lyman continuum photon produces a Balmer-line photon, and a Lyman- α photon along with other photons coming from lower series. The Balmer line thus emitted can escape the HII regions, while the Lyman- α photon gets resonantly scattered within the nebula, which is optically thick to this resonance line. Thus, the total number of Balmer-line photons produced in the recombination process is a measure of the ionizing stellar ultraviolet flux, and thereby the number of ionizing stars.

The generation of continuum emission in HII regions results mainly from three processes;

- 1) Recombination of free electron with ionized Hydrogen, singly and doubly ionized Helium (free-bound transitions)
- 2) Free-free continuum emitted by free electrons which are accelerated in Coulomb collisions with positive ions (thermal bremsstrahlung)
- 3) Two-photon continuum emission from Hydrogen, during transitions from the 2^2S to 1^2S level

Starburst nuclei have H_α luminosities in the range 10^{40} to 10^{42} erg s $^{-1}$ and are powered by hundreds to thousands of ionizing stars, in contrast to normal and giant HII regions (like Orion, W49, NGC 3603 in the Milky way) which have luminosities of 10^{37} to 10^{39} and are ionized by a single or few tens of massive stars. The H_α luminosities serve as a good measure of the number of ionizing stars, and can be used to estimate the star formation rates. The H_α equivalent width essentially measures the ratio of the ionizing flux (produced by massive stars having 10–100 M_\odot) to the red continuum which is dominated by giants (typical masses 0.7– 3 M_\odot), and is sensitive to the IMF slope. The nature of the young, ionizing massive stars and their ages can be estimated from the Balmer line (H_α , H_β , etc) luminosities. But when one studies star– forming regions one intends to sample the entire population in order to understand the star– formation history of the region. The older population can be studied using the stellar absorption features in the spectra. Some of the important stellar absorption features seen in the spectra of galaxies include, Mg II $\lambda\lambda 5172, 5183\text{\AA}$, Na I $\lambda 5896\text{\AA}$, in the optical, and Ca II triplet lines $\lambda\lambda 8498, 8542, 8662\text{\AA}$ and Mg I $\lambda 8807\text{\AA}$ in the NIR region. Most of these absorption lines are produced by the late-type stars, red giants and red supergiants.

In this chapter, we present and discuss the results obtained from optical–NIR spectroscopy of a sample of nearby starburst galaxies. For most of the discussion on emission lines, we follow Osterbrock (1989), which provides a clear understanding of the physics of emission line spectra. The details regarding the observations and reductions, and the sample used are given in section 5.2. The physical properties of the nebular gas is discussed in section 5.3, while the stellar populations are discussed in section 5.4. A comparison between the properties of starburst nuclei, and other related objects is presented in section 5.5 followed by a discussion of the star formation related parameters and the ages of the star formation episodes in sections 5.6 and 5.7. A summary of the results is provided in section 5.8.

5.2 Sample selection, observations and reductions

The sample of starburst galaxies defined by Devereux (1989) were chosen for our spectroscopic studies, along with few other well-known starburst candidates NGC 972, NGC 1808 and NGC 3310. The properties of the sample galaxies like morphological type, co-ordinates, velocity and distance (assuming $H_0 = 75 \text{ km s}^{-1} \text{ Mpc}^{-1}$) are given in Table 5.1.

Table 5.1
Starburst galaxy sample

Galaxy name	Type	R.A.(J2000)	Dec(J2000)	V_0 km s ⁻¹	Distance Mpc	Scale (1" in pc)
N470	Sbc(s)II.3	01 19 45.6	+03 24 37	2374	31.65	153.4
N972*	Sbpec	02 34 13.3	+29 18 42	1543	20.57	99.72
N1808*	Sbcpec	05 07 42.8	-37 30 51	1005	13.40	64.96
N2273	SBa(r)	06 50 08.6	+60 50 45	1840	24.53	118.92
N2750	SABc	09 05 48.1	+25 26 09	2674	35.65	172.83
N2782	Sa(s)pec	09 14 05.5	+40 06 52	2562	34.16	165.60
N3310*	Sbc(r)pec	10 38 46.1	+53 30 08	980	13.06	63.314
N3504	SBb(s)I-II	11 03 10.8	+27 58 25	1539	20.52	99.48
N4102	Sb(r)II	12 06 23.4	+52 42 41	837	11.16	54.10
N4984	Sa(s)	13 08 57.2	-15 30 58	1206	16.08	77.95

* do not belong to the Devereux (1989) sample

Devereux (1989) defined the starburst galaxy sample such that it includes all nearby [$15 < D(\text{Mpc}) < 40$], non-Seyfert 1 galaxies with central $10 \mu\text{m}$ luminosities $\geq 6 \times 10^8 L_\odot$, declinations $> -20^\circ$, right ascensions between 22 and 16 hours and galactic latitudes $\geq 20^\circ$. The inner one kiloparsec region of these galaxies show high levels of star formation activity which are comparable to prototype starburst galaxies like M82 and NGC 253. The galaxies in our sample which do not belong to the Devereux sample are known to

be starbursts from various other studies (Ravindranath & Prabhu 1998 for N972; Forbes, Boisson & Ward 1992 for N1808; Terelevich et al 1990 for N3310).

The spectra of the nuclear regions of the sample starburst galaxies were obtained using the 2.34-m Vainu Bappu Telescope (VBT) at the Vainu Bappu Observatory (VBO) located at Kavalur, India. The Opto-Mechanics Research (OMR) spectrograph was used with a 600 lines mm^{-1} grating blazed at $\lambda 7500\text{\AA}$ and the spectra were acquired on a Tektronix CCD of $24\mu\text{m}$ square pixels of 1024×1024 format. Most of the blue spectra covering the wavelength range $\lambda 4500\text{\AA}$ to $\lambda 7000\text{\AA}$ were obtained during the observing runs in March and December, 1997 and also in April, 1998 while the red spectra covering $\lambda 6400\text{\AA}$ to $\lambda 9100\text{\AA}$ were obtained during January – March, 1998 and May 1998. The detailed observation log is given in Chapter 2. The typical exposure times for individual spectra were 1800s and 2400s. Most of the nights were spectroscopic and the seeing usually varied between $2.0''$ and $2.3''$. The slit width used was $300\mu\text{m}$ for all the observations and this yields a spectral resolution of 5.2\AA . The image scale along the spatial direction is $1.06 \text{ arcsec pixel}^{-1}$.

The projected slit width on the image plane corresponds to $2''$ and the one-dimensional spectra were extracted by adding up 6 pixels or in other words the extraction was done using an aperture of dimension $2'' \times 6''$. This fixed aperture when projected onto the sky corresponds to varying physical dimensions depending on the distance to the galaxy. From Table 5.1, taking the average scale of $1'' = 100 \text{ pc}$, the above aperture would sample the inner $200 \times 600 \text{ pc}^2$ for typical distances of the galaxies. Thus the spectra we present would in most cases correspond to the integrated spectra of the nuclear and circumnuclear star-forming regions and can however be used to estimate the physical conditions in the inner few hundred parsecs of starburst galaxies.

The reductions were done using the *specred* package in IRAF and the measurements of line intensities, and equivalent widths were made using the *splot* task. The details of the reduction procedure are given in Chapter 2. The flux calibration of the spectra were done using the spectra of spectrophotometric standard stars from Hamuy *et al* (1994) and Massey *et al* (1988). The Near-IR spectra are severely affected by atmospheric bands,

mostly due to water vapour. Our interest in the NIR spectra is mainly centered around the Calcium triplet lines at $\lambda\lambda 8498, 8542, 8662 \text{ \AA}$, which are more affected by the TiO absorption bands and other metal lines. Hence, the continuum-fitting in these regions, for the measurement of the equivalent widths of Ca T lines becomes very difficult. The method adopted for measuring the Ca T equivalent widths with respect to a defined pseudo-continuum will be discussed in section 4.4.

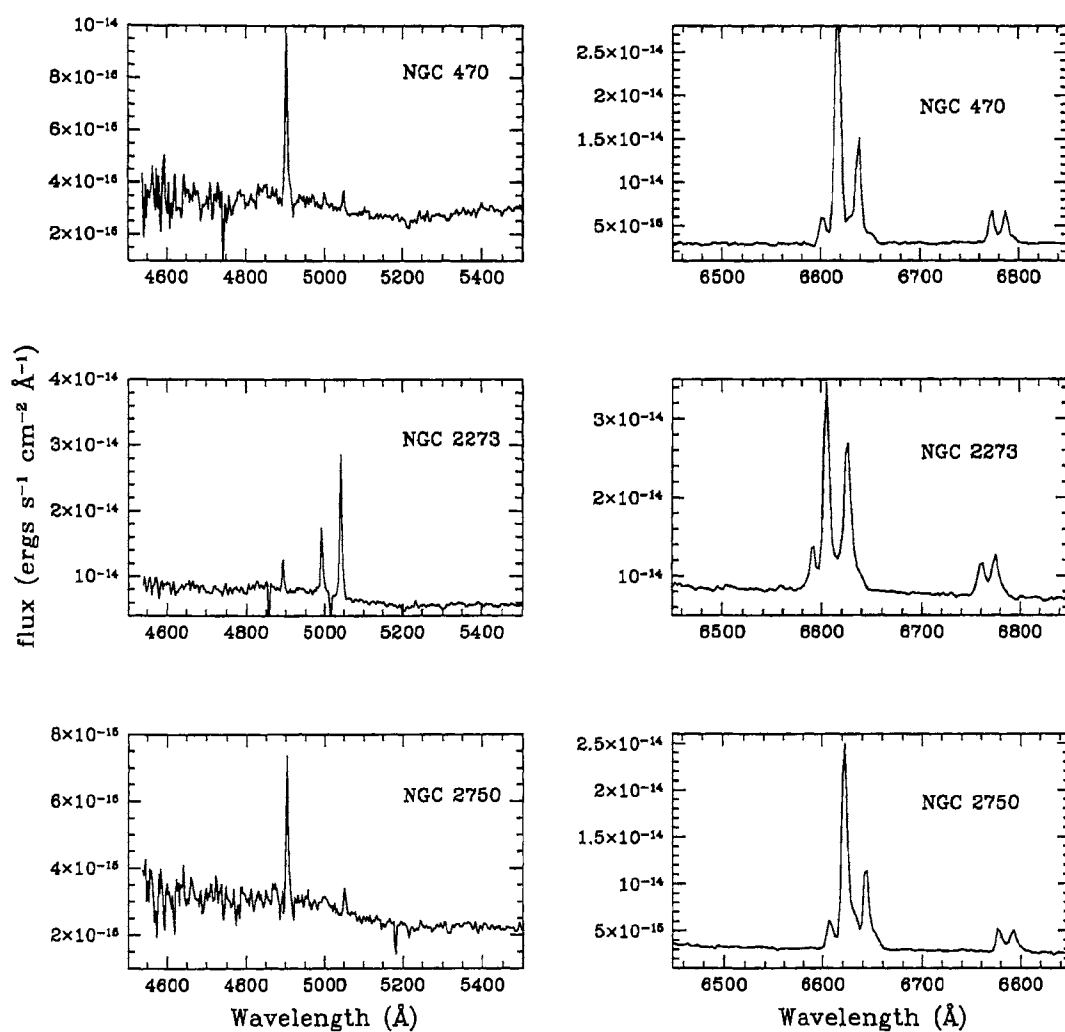


Figure 5.1: Optical spectra of the sample galaxies around H_α and H_β .

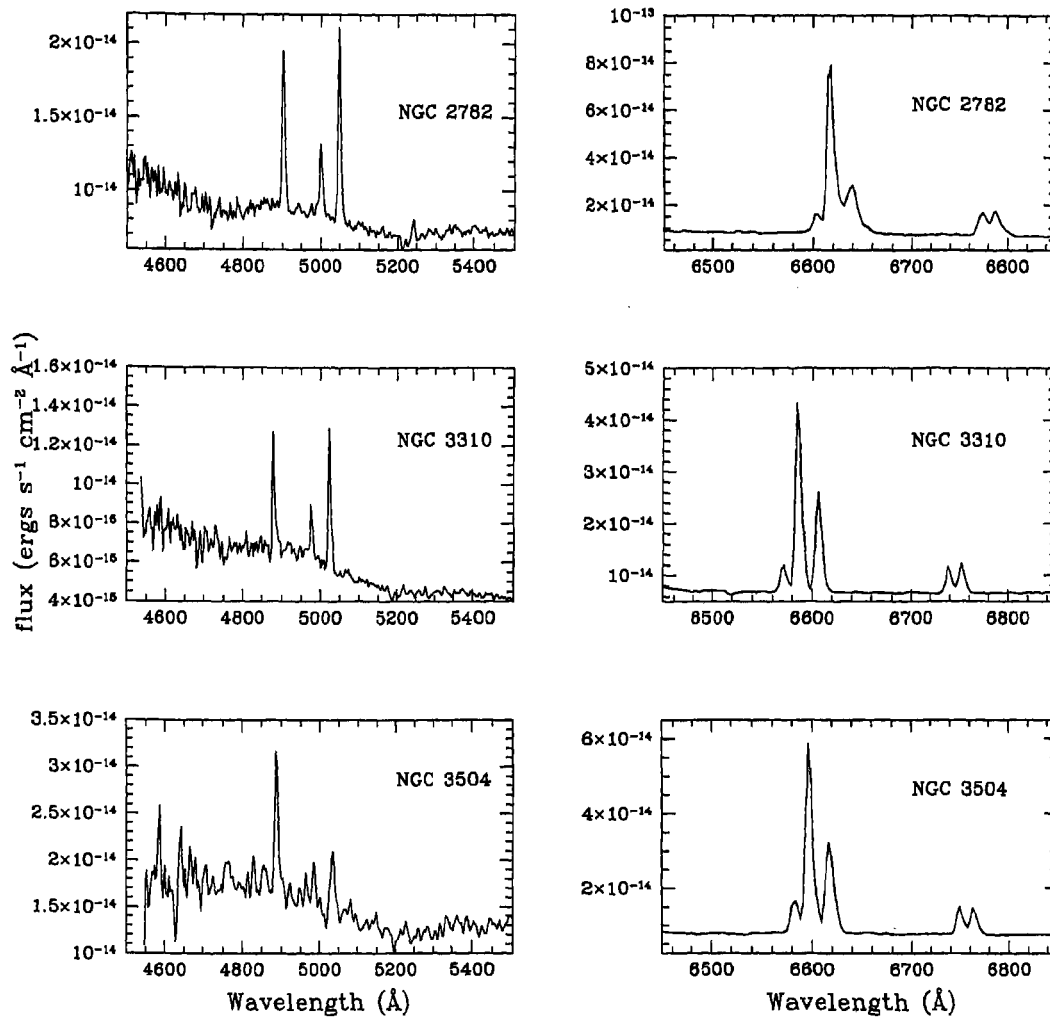


Figure 5.2: Optical spectra of the sample galaxies around H α and H β .

5.3 Emission line spectra – electron densities, ionization parameter, internal reddening and oxygen abundances

The nebular spectra emitted by star-forming regions serve as powerful tools to study the physical properties of HII regions; like electron densities and temperatures, ionization parameter and nebular abundances (McCall, Rybski and Shields 1985; Zaritsky, Kennicutt and Huchra 1994). McCall, Rybski and Shields (Hereafter, MRS85) carried out spectrophotometric observations of 99 HII regions in 20 spiral and irregular galaxies in order to study the physical properties of HII regions, the Balmer line equivalent widths, metal abundances and the effects of internal extinction by dust. They found that most of the HII regions are ionization-bounded and that the nature of the emergent spectrum can be parametrised using the oxygen abundance. Zaritsky, Kennicutt and Huchra (Hereafter, ZKH94) used a sample of 39 spiral galaxies, each with at least five HII regions for which $([\text{OII}]+[\text{OIII}])/H_{\beta}$ has been measured, to examine the relationships between abundances and macroscopic properties of the galaxies. They inferred the temperatures of the ionizing stars using the radiation softness parameter η and found that the hardness of the radiation increased with increase in radius along the disk. The metallicity dependence of the parameter η which is responsible for this behaviour has been further confirmed by Bresolin, Kennicutt and Garnett (1999). ZKH94 also find that the nebular abundances are well correlated with the luminosities of the host spiral galaxies and their Hubble types.

Kennicutt, Keel and Blaha (1989; KKB89) have compared the properties of disk HII regions, and circumnuclear hotspots with nuclear starbursts and HII nuclei. They found that hotspot HII regions are comparable in luminosity to the brightest disk HII regions, but the stellar continua are stronger. The stellar continua are also very strong in HII nuclei as judged from the low Balmer line equivalent widths and is consistent with a scenario of continuous star formation over the age of the disk. KKB89 noticed that the

low-ionization lines like [NII] and [SII] are stronger in the HII nuclei compared to disk HII regions and attributed this to the presence of a weak Seyfert or LINER nucleus. In a more recent study Ho, Filippenko and Sargent (1997; HFS97) have identified a large sample of HII nuclei and discussed their observational characteristics, variations with Hubble type, and how they differ from disk HII regions. HFS97 confirmed that the equivalent widths of the Balmer lines are higher for the disk HII regions compared to HII nuclei. Their studies also show that the excitation level of starbursts as judged from the [OIII]/H β ratio, is much higher than for their sample of HII nuclei. This led them to suggest that starbursts have lower metal abundances and may evolve towards high metallicity HII nuclei.

Table 5.2

Emission line intensities and diagnostic ratios

Galaxy	$\frac{[OIII]5007}{H\beta}$	$\frac{[OI]6300}{H\alpha}$	$\frac{[NII]6583}{H\alpha}$	$\frac{[SII]6717}{H\alpha}$	$\frac{[SII]6731}{H\alpha}$	$\frac{[SII]6717,6731}{H\alpha}$	R[S II]*	$\frac{H\alpha}{H\beta}$
N470	0.10	0.019	0.40	0.12	0.11	0.23	1.10	6.18
N972	0.78	(0.026)	0.46	0.17	0.16	0.33	1.09	7.70
N1808	0.28	0.038	0.64	0.09	0.11	0.20	0.99	12.67
N2273	5.93	0.100	0.84	0.24	0.23	0.47	1.01	5.59
N2750	0.18	0.019	0.43	0.13	0.11	0.24	1.14	3.87
N2782	0.94	0.063	0.47	0.26	0.21	0.47	1.04	3.28
N3310	0.96	0.046	0.47	0.13	0.14	0.27	0.95	3.65
N3504	0.57	0.027	0.58	0.15	0.13	0.28	1.11	5.81
N4102	0.83	0.044	0.89	0.16	0.16	0.32	1.00	8.25
N4984	0.66	...	0.78	0.37	0.31	0.68	1.19	3.26

* $R[S II] =$ ratio of the two [S II] line intensities

We have used the diagnostic emission line ratios to infer the physical properties of our sample of starburst nuclei. In Table 5.2, we present the line intensities for few strong emission lines and some important diagnostic line ratios. We have not corrected the line ratios for Galactic extinction and internal reddening. However, this should not affect the

results discussed here since the diagnostic line ratios are formed using lines which are very close in wavelengths. The H_β line is affected by the underlying stellar absorption in the case of NGC 972, NGC 3310, NGC 4102 and NGC 4984. We corrected the H_β emission line fluxes for this absorption by adding an equivalent width of 2\AA , which is the normal procedure adopted in the study of GEHRs (ZKH94, KKB89, Gonzalez - Delgado et al 1995).

In figure 5.3, we compare our measured emission line ratios with those of Ho *et al* (1997) for all the galaxies that are common to both samples. We find that the ratio of their measurements to ours have a mean value close to 1, implying that there is a good agreement between the two measurements.

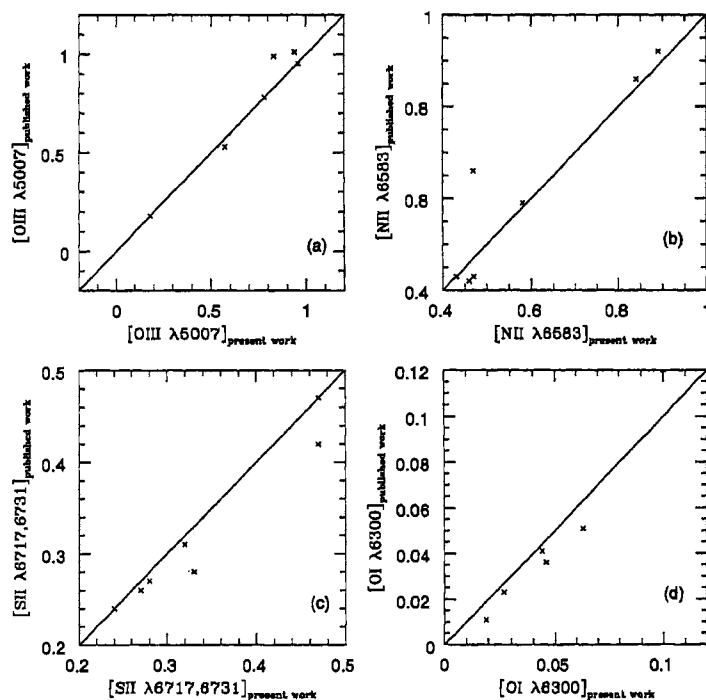


Figure 5.3: A comparison of our measured emission line ratios with those of Ho *et al.* 1997. The [OIII] intensity ratio is relative to H_β , while other line intensities are relative to H_α . The straight lines represent a line of slope 1. The mean ratios are 1.04 ± 0.34 , 0.96 ± 0.12 , 0.96 ± 0.07 , 0.87 ± 0.10 for the quantities in *a*, *b*, *c*, and *d* respectively

The [SIII] λ 9069 \AA line could be measured only for four galaxies in the sample, namely, NGC 2750, NGC 2782, NGC 3310, and NGC 3504. In other cases, the [SIII] λ 9069 \AA line fell close to the edge of the detector or were redshifted out of the wavelength range covered. Also, the region around the [SIII] λ 9069 \AA line is severely affected by the atmospheric water vapor absorption bands. The intensity of the [SIII] λ 9532 \AA line was obtained from the observed [SIII] λ 9069 \AA line, using the theoretical ratio of 2.48 between the two lines (ZKH94). For NGC 1808, we have used the [SIII] $\lambda\lambda$ 9069,9532 \AA line intensities from Forbes et al (1992).

5.3.1 Electron densities

The average density in a nebula can be measured by comparing the intensities of two lines of the same ion emitted by different levels with nearly the same excitation energy and the same lower level, so that the relative excitation rates at the two levels depend only on the ratio of collision strengths. The relative population of these two levels depend on the density, and hence, the ratio of intensities of the lines they emit will also depend on the density. The [SII] λ 6717/[SII] λ 6731 ratio (R[SII]), serves as a very useful diagnostic of the electron densities in nebular regions. At densities below the critical density $N_e = 3 \times 10^3 \text{ cm}^{-3}$, these lines are produced by the radiative de-excitation of the collisionally excited [SII] ion, and the ratio of the emission line intensities depends only on the electron density. R[SII] varies linearly with electron density for a range of values, and within this range the ratio of the [SII] lines can be used as an electron density diagnostic. The lower end of this range is marked by R[SII] = 0.44, which corresponds to the high density limit of $N_e \approx 30,000 \text{ cm}^{-3}$ while the upper end is marked by R[SII] = 1.42 which corresponds to the low density limit of $N_e \approx 30 \text{ cm}^{-3}$ (Czyzak *et al.*, 1986). Figure 5.4 shows the density sensitive ratio between [SII] lines, plotted against the oxygen abundance diagnostic. The horizontal line corresponds to the low density limit of $N_e = 30.5 \text{ cm}^{-3}$ for R[SII] = 1.42. The ratio for starbursts lies well below this limit and the average value of this ratio for our sample nuclei (Table 5.3) is equal to 1.05 ± 0.08 , which corresponds to

electron densities of $N_e = 500 \pm 170 \text{ cm}^{-3}$. This is an order of magnitude higher than the mean $N_e = 70 - 80 \text{ cm}^{-3}$ obtained for disk HII regions which have $R[\text{SII}] = 1.37 \pm 0.02$.

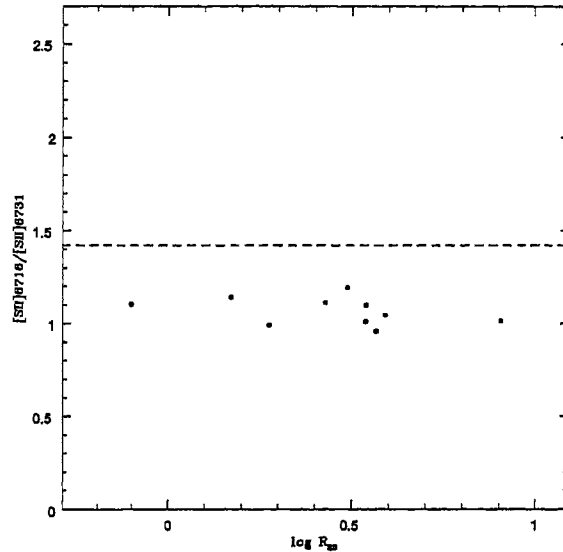


Figure 5.4: The density sensitive ratio of [S II] lines plotted against the oxygen abundance diagnostic $R_{23} = \log(([\text{OII}] + [\text{OIII}])/H\beta)$. The dashed line is the upper limit for $R[\text{SII}]$ which implies the low density limit.

5.3.2 Ionization parameter

The overall structure of a nebula can be characterized by the ionization parameter, which is a combination of the density, filling factor and the ionizing flux. The degree of ionization in a nebula depends on the ionization parameter U , defined as the ratio of the ionizing photon flux to the gas density. In the case of galaxies for which [SIII] $\lambda\lambda$ 9069,9532 line fluxes were available, we calculated the ionization parameter using the relation (from ZKH94);

$$\log U = -1.69 \log([SII]/[SIII]) - 2.99 \quad (5.1)$$

We find that the value of U in our starburst nuclei sample ranges from $10^{-3.1}$ to $10^{-2.3}$ (Table 5.3). The emission line spectra of AGNs – LINERS and Seyferts is known to be powered by a power-law ionizing continuum and the ionization parameter in these nuclei range from $10^{-3.5}$ to $10^{-2.5}$. It is interesting to note that the ionization parameter for starburst nuclei is similar to the range found in Seyfert 2 nuclei and LINERS (Ho *et al.*, 1993).

Table 5.3

Properties of ionized gas

Galaxy name	$C_{H\beta}$	$E(B - V)$	$n_e(\text{cm}^{-3})$	$\log U$	$\log \eta$	$12 + \log(\text{O}/\text{H})$
N470	1.01	0.68	718.2	9.297
N972	1.20	0.81	555.1	8.983
N1808	1.97	1.34	1138.9	-2.43	1.37	9.158
N2273	0.79	0.53	811.3	8.403
N2750	0.36	0.24	463.5	-2.90	1.16	9.219
N2782	0.18	0.12	421.6	-3.01	0.75	8.937
N3310	0.33	0.22	758.3	-3.07	0.70	8.943
N3504	0.95	0.64	465.6	-2.34	1.28	9.042
N4102	1.42	0.96	521.0	8.972
N4984	0.15	0.12	459.8	9.015

5.3.3 Oxygen abundances

The emission lines produced by HII regions can be used to determine their chemical abundances. The metallicities and temperatures of the photoionized nebula go hand-in-hand, because the metal ions are the most important coolants in the nebula. The source of cooling is the radiative de-excitation of collisionally excited metal ions like; O^+ , O^{++} , and N^+ . These ions play a significant role in the cooling process in spite of their low abundances, because they possess energy levels whose excitation potentials are of the order of kT and can be easily excited by collisions. Taking the case of oxygen ions, the cooling of nebulae takes place mainly via the transitions in the far-infrared (at 52 and

88 μm) when the electron temperature is low. At high electron temperatures, the cooling is mostly through forbidden transitions at optical wavelengths (at $\lambda\lambda$ 3727, 4959 and 5007 \AA). Thus a high intensity in the optical forbidden lines implies a higher electron temperature. Since high temperatures result from lack of sufficient metal ions to produce the cooling, this also implies low metallicities. Thus the intensities in the oxygen forbidden lines and the oxygen abundances are anti-correlated.

The oxygen abundances in HII regions can be derived using [OII] $\lambda\lambda$ 3726, 3729 lines and [OIII] $\lambda\lambda$ 4959, 5007 lines based on empirical calibrations. For ionization-bounded nebulae, there exists a strong correlation between [OII]/ H_β and [OIII]/ H_β , over a large range of excitation (McCall, Rybski & Shields, 1985). Since our spectra do not cover wavelengths less than 4500 \AA , we used the empirical relations given by MRS85 to obtain the ([OII] $\lambda\lambda$ 3726, 3729)/ H_β ratios from our observed ratios of ([OIII] $\lambda\lambda$ 4959, 5007)/ H_β . We calculated the ratio $R_{23} = ([\text{OII}] + [\text{OIII}])/H_\beta$, which is a good oxygen abundance diagnostic in the absence of temperature sensitive lines like [OIII] λ 4363. The oxygen abundance, expressed as $12 + \log(\text{O}/\text{H})$ was then obtained using the following calibration provided by ZKH94;

$$12 + \log(O/H) = 9.265 - 0.33x - 0.202x^2 - 0.207x^3 - 0.333x^4 \quad (5.2)$$

where, $x = \log R_{23}$. The oxygen abundance in the nuclear regions of our sample starburst galaxies range from 1.2 to 2.8 solar, for a solar abundance of $12 + \log(\text{O}/\text{H}) = 8.84$ (Table 5.3). In the case of NGC 2273 the [O III] λ 5007 line intensities are very high, which is likely due to excitation by a non-thermal ionizing source with hard ionizing spectrum. This galaxy has often been classified as a Seyfert and we discuss this further in the section on diagnostic line ratios. Excluding the case of NGC 2273, the mean abundance for our sample starburst nuclei is 1.742 ± 0.53 , relative to solar.

5.3.4 Temperatures of ionizing stars

Vilchez & Pagel (1988) have described how the temperatures of ionizing stars in HII regions can be estimated through the use of the radiation softness parameter, η , defined by

$(O^+/O^{++})(S^{++}/S^+)$. The parameter η serves as a good criterion to study the effective temperature of the ionizing stars whenever the near-IR [SIII] lines are available, because it is insensitive to chemical composition, ionization conditions and is also reddening independent. For most of the commonly used reddening laws, the relative correction for S^+/S^{++} coincides with that for O^+/O^{++} , within a few per cent. The parameter η can be obtained from the line intensity ratios by defining the observed quantity;

$$\eta' = \frac{[\text{OII}]\lambda\lambda 3726, 3729}{[\text{OIII}]\lambda\lambda 4959, 5007} / \frac{[\text{SII}]\lambda\lambda 6717, 6731}{[\text{SIII}]\lambda\lambda 9069, 9532} \quad (5.3)$$

and,

$$\log \eta = \log \eta' + \frac{0.14}{t} + 0.16$$

where, t is the electron temperature in units of 10,000 K. We do not have an estimate of the electron temperature and hence we calculated $\log \eta$ values for an assumed T_e of 10,000 K. At lower electron temperatures, the second term in the equation becomes significant compared to the other two terms. For $T_e = 8000\text{K}$, η values increase by 0.035, while for 12000K it decreases by 0.024. However, this does not have much influence on the estimated value of T_* , nor does it affect the behaviour with metallicity. The value of T_* mainly depends on the first term, which is derived from the line ratios. The radiation softness parameter is very useful to study the behaviour of the temperatures of ionizing stars with abundance, but, the actual determination of the temperatures has to be based on photoionization models. From the derived $\log \eta'$ values and oxygen abundances, we estimate $T_* < 40,000$ K for the ionizing stars, using the models of Bresolin, Kennicutt & Garnett (1998). Even within our small sample of starbursts for which [SIII] line could be measured, we do see a tendency for $\log \eta$ to increase with increase in metallicity (see Table 5.3). This implies a decrease in the effective temperatures of the ionizing stars with increase in metallicities.

5.3.5 Internal reddening in nuclear regions

The spectra of HII regions are affected by the extinction due to dust associated with them, and this is referred to as internal extinction. Internal extinction has been found to

be very high in starburst systems, as inferred from the intensities of the emission lines as well as from the high far-infrared fluxes emitted by these regions. In HII regions, dust causes the ratio of two nebular emission lines to differ from the actual ratio with which these lines were emitted. Thus the observed line intensity ratio is given by

$$\frac{I_{\lambda_1}}{I_{\lambda_2}} = \frac{I_{\lambda_1}(0)}{I_{\lambda_2}(0)} e^{-(\tau_1 - \tau_2)} \quad (5.4)$$

where, $I_{\lambda_{1,2}}(0)$ are the actual intensities emitted, and $\tau_{1,2}$ are the optical depths at the two wavelengths. The above equation can be written in a different way, by using ratios involving H_β which is conventionally used as the standard nebular line.

$$\frac{I_{\lambda_1}}{I_{H\beta}} = \frac{I_{\lambda_1}(0)}{I_{H\beta}(0)} 10^{-C[f(\lambda) - f(H\beta)]} \quad (5.5)$$

where, C is a measure of the amount of extinction and $f(\lambda)$ is the extinction curve. The common method adopted to determine internal reddening is the use of the Balmer decrement which is estimated by comparing the observed ratios of the HI balmer lines (H_α/H_β , H_β/H_γ) with what is predicted by theory. These Balmer line ratios are used to estimate the constant C from the above equation, which is referred to as the logarithmic extinction at H_β and is designated by $C_{H\beta}$. Thus, the reddening corrected line intensity for any nebular line is given by;

$$I_\lambda = I_{\lambda(0)} 10^{-C_{H\beta} f(\lambda)} \quad (5.6)$$

Using the extinction curve of Seaton (1979), the above equation can also be written as;

$$I_\lambda = I_{\lambda(0)} 10^{-A_v E(\lambda)} \quad (5.7)$$

where, $E(\lambda)$ is the shape of the extinction curve, and A_v is the extinction in magnitudes in the V band. Equating the exponents allows the determination of A_v once $C_{H\beta}$ is known. From the visual extinction, the internal reddening $E(B - V)$ can be obtained using;

$$E(B - V) = A_v / R_v \quad (5.8)$$

The values of the logarithmic extinction at H_β , $C_{H\beta}$, and corresponding values of $E(B - V)$ are given in Table 5.3. The mean $E(B - V)$ for the starburst nuclei is 0.569 ± 0.38 , with a

median value of 0.589. This is similar to the values for HII nuclei residing in early-type galaxies studied by Ho *et al*, (1997).

5.4 Stellar populations in the nuclear regions – the implications for star formation scenarios

One of the most interesting issues in the study of starbursts is the star formation history of these nuclei. The stellar content of galaxies comprise of many distinct populations resulting from different star-formation episodes. Hence the observed galaxy spectrum is a result of the contribution from stars of low mass and high mass, cool and hot temperatures and those in their early and late stages of evolution. Three different star formation laws are usually considered in the study of the stellar content of galaxies – the instantaneous burst scenario (IB), continuous star formation (CSF) and a scenario of exponentially decaying star formation. In general, the star formation rate can be expressed as;

$$\psi(t) = \psi(t = 0)e^{-t/\tau}, \quad (5.9)$$

where, t and τ are the age and duration of the burst, respectively. If the duration of the burst is very small compared to the age of the cluster, then all the stars can be considered to have formed co-evally and this is referred to as the instantaneous burst scenario. In constant star formation scenario, it is assumed that the star formation rate is constant with time. This can also be considered as a series of instantaneous bursts with ages roughly equal to the burst duration. In the case of exponentially decaying star formation there is a burst of star formation going on from $t = 0$ to $t = T_0$ and the star formation process decays thereafter.

In the case of a very young burst of star formation which is less than about 3 Myr old, the Balmer recombination lines, especially the H_α line, can be used to study the properties of the embedded ionizing stellar cluster containing hot, massive OB stars. But as the cluster evolves the massive stars leave the main sequence and the ionizing photons begin to decrease in the case of an instantaneous burst (IB) scenario. Thus the H_α line

is no longer a good tracer of the age of the stellar cluster. In the case of a continuous star formation (CSF) scenario, the nebular spectrum reflects only the properties of the youngest population. Thus the age determination of an instantaneous burst that has evolved beyond the early nebular phase, or of a composite population consisting of a young, ionizing cluster co-existing with a slightly older population around 10 Myr old, would require the study of stellar features that are indicative of an evolved population. The presence of such an evolved population can be revealed by the detection of strong near-infrared Ca II Triplet (Ca T) lines in absorption.

The Ca T ($\lambda\lambda$ 8498, 8542, 8662 Å) absorption lines are produced by red giant and red supergiant stars and are the most prominent features in the Near - IR spectra of galaxies. The equivalent width of these absorption lines show biparametrical behaviour with surface gravity and metallicity - the strength increasing with decreasing gravity and increasing metallicity (Jones, Alloin & Jones 1984; Mallik 1994). However, at high metallicities ($Z > 0.5 Z_{\odot}$), the equivalent width of the Ca II triplet is only a function of the surface gravity of the stars and the EW (Ca T) values are higher than 7 Å only when red supergiant stars are present. Thus the presence of red supergiant stars (RSGs) or in other words the presence of a stellar population which is about 10 Myr old can be inferred from the strength of the Ca T feature (Diaz, Terlevich & Terlevich 1989; Garcia-Vargas et al 1997). The importance of the Ca T feature in studying the role of starbursts in Active Galactic Nuclei (AGNs) has been emphasized by Terlevich, Diaz and Terlevich (1990). They found that while other stellar absorption features like Mg II λ 5172 Å lines are diluted by the non-thermal continuum of the AGN, the Ca T was seen at full strength implying the presence of the RSGs and hence a young starburst which is only 10 Myr old.

5.4.1 H_{α} luminosities and equivalent widths

The Balmer recombination lines at optical wavelengths have been the most important probes to study the properties of young star - forming regions. As mentioned in section

5.2, the apertures over which our spectra are extracted would correspond to an area of $\approx 200 \times 600 \text{ pc}^2$. This would mean that we are sampling both the nuclear and circum-nuclear regions. The star formation related parameters are given in Table 5.4, and the H_α measurements are essentially for within the inner one kiloparsec of the galaxies. We have corrected the emission line intensities for the internal reddening, and used these for obtaining the H_α luminosities given in the table. However, the fluxes given in column 2 of Table 5.4 are the observed fluxes, without correcting for Galactic extinction or internal reddening. The molecular gas mass $M(H_2)$ within the radius $R(H_2)$ are taken from Jogee (1998) and Devereux *et al*, (1994).

Table 5.4

Star formation related parameters

Galaxy	$\log F_{H_\alpha}$	$\log L_{H_\alpha}$	$\log L_{FIR}$ ($10^{10} L_\odot$)	$M(H_2)$ $10^8 M_\odot$	$R(H_2)$ kpc	SFR ¹ ($M_\odot \text{y}^{-1}$)	SFR ² ($M_\odot \text{y}^{-1}$)	ratio
N470	-12.60	41.12	9.97	5.0	1.10	1.04	1.71	0.608
N972	-13.07	40.54	10.43	0.27	4.86	0.056
N1808	-12.13	41.34	10.18	1.73	2.77	0.62
N2273	-12.73	40.83	9.88	0.53	1.37	0.387
N2750	-12.78	40.71	10.12	4.4	1.29	0.41	2.41	0.170
N2782	-12.54	40.77	10.32	23.0	2.55	0.46	3.78	0.12
N3310	-12.58	40.23	10.20	0.38	1.88	0.13	2.88	0.04
N3504	-12.11	41.43	10.39	12.0	1.30	2.13	4.50	0.47
N4102	-12.52	40.95	10.30	14.0	1.27	0.713	3.60	0.198
N4984	-12.95	39.87	9.86	0.059	1.31	0.045

All the sample galaxies have H_α luminosities $\geq 10^{40} L_\odot$, which is the defining characteristic of starbursts (Balzano 1983). Stars with masses $> 10 M_\odot$ and lifetimes less than 20 Myr are the main source of ionizing flux in young starbursts. The nebular recombination lines effectively re-emit the integrated stellar UV luminosity and provide a direct measure of the star formation rate (SFR). We use the calibration given by Kennicutt (1998) for

deriving the star formation rates from the H_α luminosities. Assuming a Salpeter IMF and using solar abundances;

$$SFR(M_\odot yr^{-1}) = 7.9 \times 10^{-42} L(H_\alpha)(ergs^{-1}) \quad (5.10)$$

The mean star formation rate for starbursts is found to be $0.75 \pm 0.64 M_\odot yr^{-1}$. This is slightly higher than the SFRs of HII nuclei studied by Ho *et al.*, (1997) but is still only a moderate star formation rate compared to starbursts found in Ultraluminous Infrared Galaxies, where the SFR can be as high as few hundred solar masses per year. The average star formation density of our sample starburst nuclei is $\Sigma_{SFR} = 8.79 M_\odot yr^{-1} kpc^{-2}$ and ranges from 1–35 $M_\odot yr^{-1} kpc^{-2}$. This in good agreement with the star formation densities expected for circumnuclear regions (≈ 1 -1000 $M_\odot yr^{-1} kpc^{-2}$). In contrast, the SFR densities for normal spiral disks is much lower ~ 0 -0.1 $M_\odot yr^{-1} kpc^{-2}$ (Kennicutt 1998).

The H_α emission line equivalent width is proportional to the ratio of the ionizing flux to the continuum from the underlying stellar population. The measured H_α EWs for our sample of starburst nuclei are presented in Table 5.5. The average H_α EW is $44 \pm 20 \text{ \AA}$ and this is much lower than the EWs of disk HII regions which are usually of the order of a few hundred angstroms. Extremely low values of H_α EWs are also found in HII nuclei and have been explained in terms of evolved stellar populations present in nuclear regions (KKB89; HFS97). The contribution from evolved bulge stars can dominate the continuum in nuclear regions, thereby diluting the EWs significantly in comparison to disk HII regions. This would be the case if the star formation in nuclear regions is taking place at a constant rate. As mentioned earlier, our spectra include both the nuclear and circumnuclear regions. The circumnuclear regions are known to contain pure H_α emission knots and continuum knots whose positions often do not coincide. The continuum knots probably belong to earlier episodes of star formation and contain evolved massive star populations, which increases the continuum contribution and results in low H_α EWs. Another factor that can contribute to the reduction of EWs in nuclear regions is the internal extinction. The EWs can be considerably low if the young, ionizing stars and gas

(with associated dust) belonging to the sites of most recent star formation episode, suffer more extinction compared to the continuum-emitting regions. Such differential extinction for the line-emitting gas and continuum-emitting stars, have been seen in star-forming regions (Calzetti et al, 1995; Mayya & Prabhu, 1996).

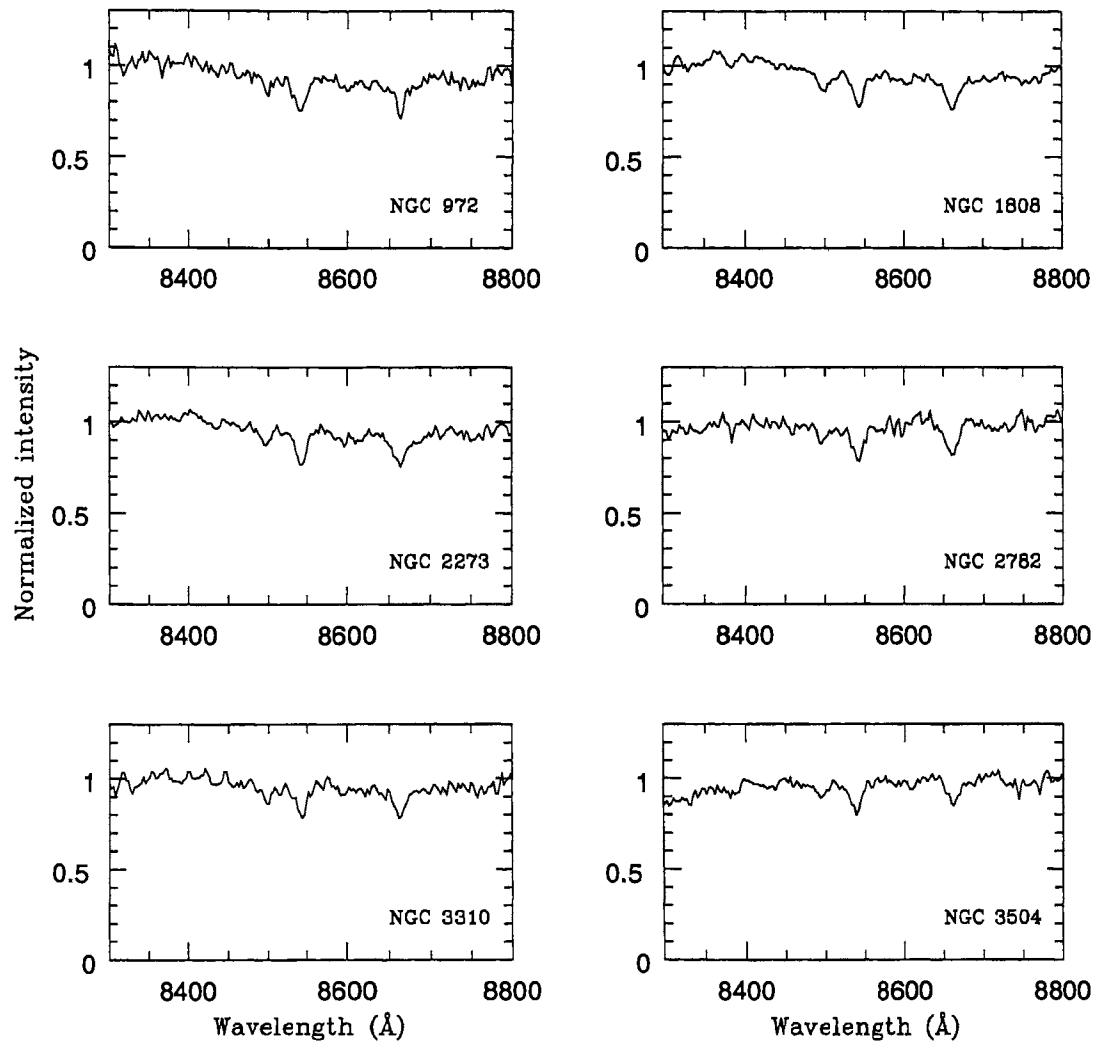


Figure 5.5: NIR spectra of the sample galaxies showing the region of CaT lines after fitting the pseudo-continuum.

5.4.2 Ca T absorption equivalent widths

The equivalent widths of the Ca II triplet lines defined using the two strongest lines of the triplet, is only a function of the surface gravity of the stars for high metallicities. Diaz, Terlevich & Terlevich (1989; DTT) and Terlevich, Diaz and Terlevich (1990; TDT) have shown that strong Ca T lines (equivalent widths $> 7\text{\AA}$ at solar or above solar metallicities) in star-forming regions, indicates the presence of red supergiant stars (RSGs). We measured the EW(Ca T) lines by adopting the procedure described in DTT89. The spectral region around the Ca T ($\lambda\lambda$ 8542,8662 \AA) line is contaminated by TiO absorption bands and other metal lines and hence choosing the continuum for measurement of equivalent widths becomes difficult. DTT89 found that the continuum is remarkably flat between $\lambda 8440\text{\AA}$ and $\lambda 8800\text{\AA}$ for a large sample of stellar spectra covering a wide range in surface gravity and metallicity. They define a pseudo-continuum by doing a linear fit to the median value of two chosen side-bands, centered at $\lambda 8455\text{\AA}$ and $\lambda 8850\text{\AA}$, with a width of 15\AA . The normalized spectra after performing the pseudo-continuum fit are shown in figure 5.5 for some of our sample starburst nuclei. The measured values of EW(Ca T) for our sample galaxies are given in Table 5.5. From data obtained during different observing runs, we estimate errors of $0.3\text{\AA} - 0.9\text{\AA}$ in our measurement of the Ca T equivalent widths. No corrections were made for the contamination by the Paschen lines Pa15 $\lambda 4545$ and Pa13 $\lambda 8665$ which is negligible. Within the errors, our equivalent widths are in good agreement with those of TDT90 for galaxies which we have in common with their sample. The measured EW(Ca T) are greater than 7\AA for all the starburst nuclei, except NGC 4984, and implies the presence of RSGs.

Thus from the H_α luminosities and equivalent widths, and the Ca T equivalent widths, it appears that most of the starburst nuclei have composite population of young, ionizing stellar population co-existing with evolved, non-ionizing RSG populations produced by previous bursts.

Table 5.5*Measured equivalent widths*

Galaxy name	EW(Ca T)	EW(H α)	(O/H)/(O/H $_{\odot}$)
N470	9.728	81.68	2.864
N972	7.733	21.48	1.390
N1808	8.576	51.16	2.079
N2273	8.205	29.06	0.365
N2750	7.688	58.66	2.393
N2782	7.288	67.88	1.250
N3310	7.033	42.00	1.267
N3504	7.173	57.3	1.592
N4102	8.458	30.01	1.355
N4984	6.357	10.60	1.496

5.5 Properties of the photoionized gas in starburst regions

Having obtained the physical parameters that characterize the photoionized gas in starburst nuclei, it is of interest to see how these properties compare with those of disk H II regions and other related objects like, H II nuclei and low-luminosity AGNs (like, LINERs & Seyfert nuclei).

5.5.1 A comparison of starburst nuclei and HII nuclei

In this section, we proceed to compare the physical conditions derived for starburst nuclei, with those of HII nuclei and disk HII regions. We find that starburst nuclei have higher electron densities ($N_e \approx 500 \text{ cm}^{-3}$) compared to HII nuclei and disk HII regions. Majority of the HII nuclei are known to have $n_e \approx 180 \text{ cm}^{-3}$ (HFS97; KKB89) while the disk HII regions lie at the low density limits with mean $N_e \approx 70 \text{ cm}^{-3}$ (ZKH94). So it appears that HII nuclei have intermediate electron densities, bounded by starbursts

on the high density side and disk HII regions on the low density side. All the starburst nuclei in our sample reside in early -type host galaxies, while HII nuclei mostly occur in late-type galaxies (Ho *et al.*, 1997). Ho *et al.*, find that within their sample of HII nuclei, those which reside in early-type hosts have higher electron densities compared to those which reside in late-type hosts. Thus it seems logical that the high densities seen in nuclear starbursts and H II nuclei belonging to early-type galaxy hosts, result from the deeper gravitational potential provided by the dominant bulge in these galaxies.

From the derived oxygen abundances we find that starburst nuclei have metallicities in the range 1.2 to 2.8 times solar and the mean [OIII]/H β ratio equals 0.6 or log[OIII]/H β = -0.22 (excluding NGC 2273). Thus, the starburst nuclei show slightly higher excitations and lower mean metallicities (\sim 1:7) compared to HII nuclei. Ho *et al.*,(1997) found that the excitation level of starburst nuclei chosen from Balzano (1983) are very high, implying lower metallicities. HII nuclei on the other hand, exhibit [OIII]/H β similar to disk HII regions with lower excitation and higher metallicities. The oxygen abundances derived for HII nuclei imply that their mean metallicities are twice solar (HFS97). The low ionization lines like [NII] and [SII] are considerably enhanced in starburst nuclei compared to HII nuclei. The mean [NII]/H α and [SII]/H α ratios are 0.635 ± 0.17 and 0.371 ± 0.15 respectively.

5.5.2 Diagnostic emission line ratios - the enhancement of low ionization lines

Diagnostic diagrams based on emission line intensity ratios are very useful for identifying the nature of ionization. These diagrams help in classifying the nuclear spectra of galaxies as H II region-like (powered by ionizing radiation from hot, massive stars) or AGN-like (powered by accretion on to a supermassive black hole). Photoionization is the main energy-input mechanism in the case of AGNs, Starbursts, and H II nuclei. However, the ionization in AGNs shows a wide range, comprising of low ionization lines, like [O I] and

[S II], as well as high ionization lines, like [Ne V] and [Fe VII] which cannot be produced by radiation from hot, massive stars. The production of such very high excitation lines require a harder spectrum (more high-energy photons with energies of the order of few 100 eV). Also, in AGNs there exists a partially-ionized “transition zone” where H° , H^+ , O° , S^+ all coexist, and strong [O I] and [S II] lines are collisionally excited. The diagnostic line ratios used to identify the type of activity in nuclei of galaxies, whether AGN or starbursts, are those which are best suited to differentiate between the two class of objects. The ratios are formed using emission lines which are close in wavelengths, in order to minimize the effect of extinction. The diagnostic line ratios are given in Table 5.2, while the diagnostic diagrams are presented in figure 5.6. The [O III]/ H_{β} ratio is mainly an indicator of the level of ionization as well as temperature, while the [O I]/ H_{α} and [S II]/ H_{α} ratios indicate the importance of the partially-ionized zone produced by the high-energy photons. On the diagnostic diagrams, the Seyfert nuclei tend to occupy the upper right corner indicating higher excitations, while the LINERs tend to be located at the lower right, showing the presence of strong, low-ionization lines. Starbursts usually lie at the transition between normal HII regions and LINERs. From the diagnostic ratios given in Table 5.2, it is clear that most of the nuclei have [NII]/ H_{α} close to or greater than 0.6. Normal disk HII regions never exhibit [NII]/ H_{α} > 0.6, and hence this is usually adopted as the dividing line between regions that are photoionized by massive stars and regions that are powered by non-stellar sources, like in the case of AGNs. From figure 5.6, it is clear that the low-ionization lines are enhanced relative to the disk HII regions.

Shields & Kennicutt (1995) have shown that the modification of the thermal properties of nebular gas by dust within star forming regions can result in enhancement of low ionization lines. The depletion of heavy elements, which are the main coolants in HII regions, from the gas phase onto dust grains can modify the thermal properties of the HII regions. The opacity of dust is a decreasing function of photon frequency and hence, the low frequencies are effectively absorbed by dust from the incident radiation. This tends to harden the ionizing spectrum seen by gas. In other words, the effect of dust is to increase the electron temperatures in a nebula leading to enhanced optical line emission.

From figure 5.6, it is evident that all our starburst nuclei have line ratios lying above the dividing line between AGN and H II regions for dust-free models (shown by solid lines). The models which include the effects of dust (dotted lines) represent the sample nuclei fairly well.

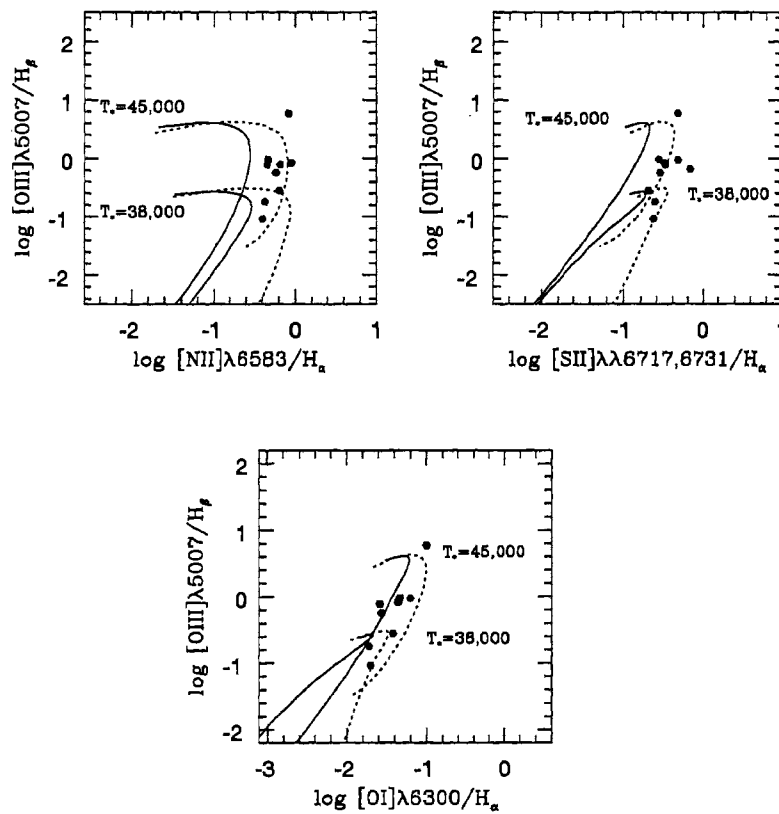


Figure 5.6: Diagnostic diagrams showing the regions occupied by AGNs and H II regions nuclei. The photoionization models results from Shields & Kennicutt (1995) are shown for temperatures $T_* = 38,000\text{K}$ and $45,000\text{K}$. The solid lines indicate models without dust, while the dotted lines are the results when the effect of dust is incorporated.

However, the observed enhancement of the low ionization lines in starbursts can also be attributed to shock ionization or the presence of weak AGN activity. In figure 5.6, the

point which clearly lies in the region of AGNs, represents NGC 2273, which has often been classified as a Seyfert nuclei. However, distinguishing between starbursts and LINERS can be very difficult, since both of them show strong shock–ionization lines like [O I] λ 6300Å.

5.5.3 The nature of the ionizing stars

We have measured the radiation softness parameter η for five galaxies in our sample for which the [SIII] $\lambda\lambda$ 9069,9532 line intensities were available. This parameter is a useful diagnostic of the temperatures (T_*) of the ionizing stars. Even though our sample is very small, it is interesting to note that there is a tendency for the radiation to get softer at higher metallicities. In other words, the temperatures of the ionizing stars decreases with metallicity. This trend is consistent with the results obtained by Bresolin, Kennicutt and Garnett (1998), for a large sample of giant HII regions. They conclude that the decrease of T_* with increasing metallicity can be due to a decrease in the upper mass limit of the IMF with increasing metal abundance, or because the current stellar models do not correctly estimate the decrease in stellar temperature with increasing abundance, at a given mass. Using the models presented by Bresolin, Kennicutt and Garnett, we estimate $T_* < 40,000\text{K}$ for the ionizing stars in starburst nuclei. This would place the upper mass limit of the IMF at $M_* \approx 25 M_\odot$ for these regions.

5.6 Star formation properties in nuclear regions

Using the H_α recombination line luminosities we have estimated the star formation rates within the inner one kiloparsec regions of our sample starburst galaxies. These regions have H_α luminosities in the range of 10^{40} to 10^{41} erg s^{-1} and mean star formation rate (SFR) of $0.75 M_\odot \text{ yr}^{-1}$. This is similar to the SFRs derived from the H_α sample of Ho *et al.*, (1997) and the FIR sample of Devereux & Hameed (1997). In Table 5.4, we have tabulated the H_α luminosities in the $\approx 200 \times 600 \text{ pc}^2$ for the sample starbursts and the corresponding star formation rates (SFR¹). The global FIR luminosities have also been used to estimate the global star formation rates (SFR²). The ratio of these

two star formation rates have also been given in the table, to compare the star formation activity confined to the inner 1 kpc with the global star formation. We find that this ratio is high (almost 40%) for NGC 470, NGC 1808, NGC 2273, and NGC 3504; indicating that most of the star formation activity in these galaxies is confined to the inner few hundred parsec radius. However, in the case of NGC 1808 and NGC 2273, a part of the H_α luminosity maybe due to weak AGN activity, since these galaxy nuclei are known to exhibit composite behaviour. The estimation of SFRs from the global FIR luminosities have always been a topic of debate, since the FIR luminosity can have contributions from dust heated by sources other than massive stars; like the stellar radiation from older populations. However, this would mean that the global FIR luminosity that probes only the massive star population is lesser and will cause the ratio of SFRs to increase.

It is interesting to note that the $^{12}\text{CO}(1-0)$ line measurements of the central $15''$ regions of the starburst galaxies NGC 470, NGC 2782, NGC 3504 and NGC 4102, show that huge amounts of molecular hydrogen gas ($> 10^9 M_\odot$) is contained in the inner regions within 1.2 to 2.8 kpc (Jogee, 1998). In the case of NGC 2750, Devereux et al (1994) have shown that most of the molecular gas ($>10^8 M_\odot$) is confined to the inner 1.2 kpc. These galaxies also show high degree of compactness in their $10\mu\text{m}$ emission and observations provide additional support to the fact that in these galaxies most of the star formation is concentrated in the inner few kiloparsecs.

5.7 Age determination of starbursts using Ca II triplet line equivalent widths

The Ca II triplet ($\lambda\lambda$ 8498, 8542, 8662 Å), is a prominent feature in the near-IR spectrum of red giant and red supergiant stars (RSGs), its strength increasing with decreasing gravity. From stellar evolutionary models it is known that massive stars in the mass range $25 - 15 M_\odot$ evolve to RSGs after 5 Myr; and hence the detection of strong Ca T lines can be used to infer the presence of massive stars in a young cluster that has evolved

beyond the early nebular phase. Terlevich, Diaz & Terlevich (1990) studied the Ca T lines in normal and active galaxies and emphasized the role of starbursts in AGN activity. The detection and measurement of Ca T absorption triplet in the giant HII region of NGC 3310, was used by Terlevich *et al.*, (1990) to reveal the presence of RSGs and estimate the age of the stellar population. Bica, Alloin and Santos (1990) have measured the EW(Ca T) of blue clusters in LMC, whose turn – off ages were already known. They found that only clusters which are ≈ 10 Myr old, have EW(Ca T) greater than 6 \AA , while the older clusters have EW(Ca T) values around 4 \AA . Evolutionary synthesis models of Mayya (1997), Garcia – Vargas *et al* (1998) and Leitherer *et al.*, (1999; Starburst 99) predict the time evolution of equivalent widths of Ca II ($\lambda\lambda 8542, 8662 \text{ \AA}$) defined using the two strong lines, for different metallicities, different IMFs and different star formation scenarios (Instantaneous Burst, IB or Continuous Star Formation, CSF). According to these models, the EW(Ca T) shows a clear maximum with values around 8 \AA at ages of about 10 Myr both for solar and higher metallicities, due to the presence of RSGs. Garcia – Vargas *et al* (1998) have computed theoretical EW(Ca T) for single stellar populations as well as for a composite of young and old populations at different ages and metallicities. They also provide a diagnostic diagram of EW (Ca T) versus the EW(H_β) (in emission) to infer the age of an evolved population. Mayya (1997) describes the use of diagnostic diagrams with EW(Ca T) versus EW(H_α) (in emission) for determining the ages of starbursts. The observed values of EW(Ca T) and EW(H_α) for our sample nuclei are given in Table 5.5.

Since the H_β line is detected with very low S/N in our spectra, we have made use of the diagnostic diagrams which use EW (H_α) for age determination (see figure 5.7). We formed similar diagnostic diagram using the Starburst99 models and this is presented in figure 5.8. We attempt to understand the star–formation history of the starburst regions based on three observables – H_α luminosities, the H_α equivalent widths and Ca T equivalent widths.

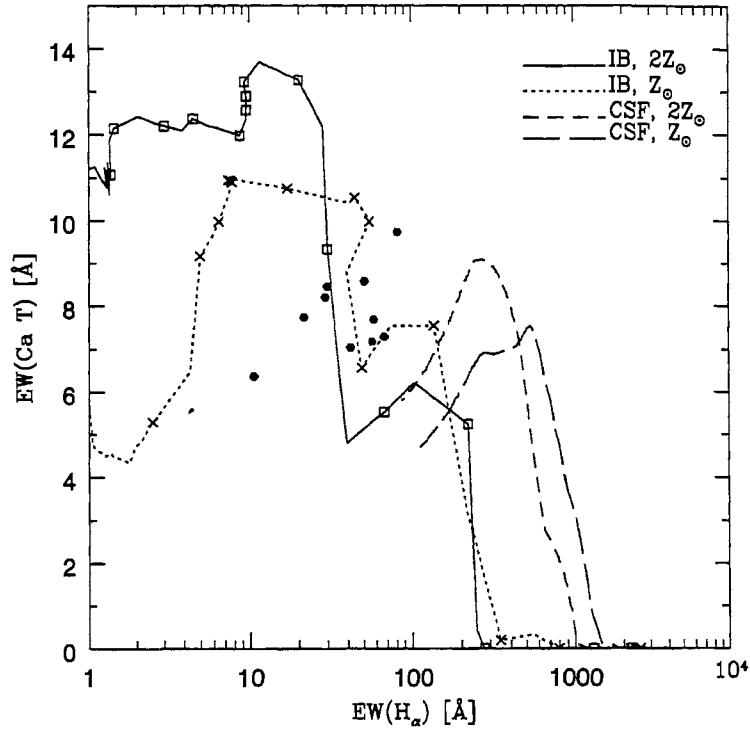


Figure 5.7: The diagnostic diagram for determining the age of the evolved population in starburst nuclei from Mayya (1997). The filled hexagons represent the sample starburst nuclei of this study. Crosses and boxes represent age marks at intervals of 1 Myr

As seen from the figures 5.7 and 5.8, the H_α equivalent widths reach a saturation value of about 100 \AA for ages beyond 3 Myrs in the case of continuous star formation (CSF) scenario. This is because, in the case of CSF, after few million years, an equilibrium is set up between the massive stars entering and evolving off the main sequence. The continuous availability of ionizing photons maintains the value of $L(H_\alpha) \geq 10^{41} \text{ erg s}^{-1}$. Hence, the hydrogen recombination lines do not indicate age of the star forming regions,

in the CSF models.

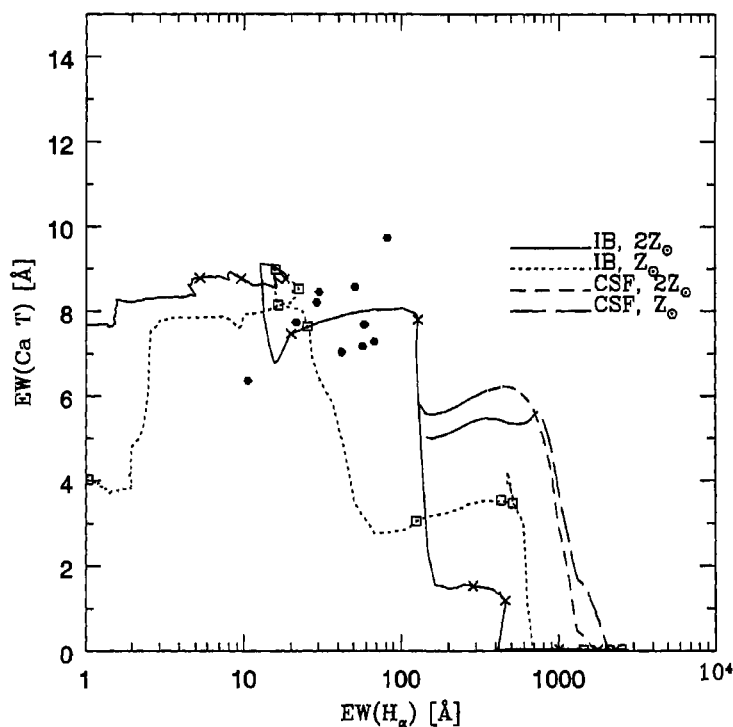


Figure 5.8: The age diagnostic diagram similar to fig 5.7 using the Starburst99 models. The open squares and crosses mark the age intervals of 1 Myr on the evolutionary tracks.

The Starburst99 models and the models from Mayya (1997) differ in the predictions of the strength of Ca T equivalent widths. In Mayya (1997) models, the $EW(\text{Ca T})$ reaches higher peak values — greater than 7 \AA for the CSF scenario and greater than 10 \AA for IB scenario, unlike in the case of Starburst99 models. These differences may be due to the different stellar atmosphere models and evolutionary tracks adopted in the two synthesis models. As mentioned earlier, the low values of $EW(\text{H}\alpha)$ found in the nuclear

regions can be due to the contribution of the underlying population to the continuum. The effects of dust in these star-forming regions can also lower the H_α luminosities and equivalent widths. However, this should not affect the Ca T equivalent widths. Since for our sample starburst nuclei, $L(H_\alpha) < 10^{41}$ erg s $^{-1}$ and EW(Ca T) values are greater than 7 Å in most cases, we mainly concentrate on the instantaneous burst models. In the case of a single stellar population, resulting from an instantaneous burst (IB) which is about 10 Myr old, the ionizing flux would decrease to $L(H_\alpha) \leq 10^{39}$ erg s $^{-1}$, for solar metallicities and assuming a Salpeter IMF (Leitherer & Heckman, 1995). The decrease in the emission line flux would also result in the decrease of EW(H_α). If we introduce the effects of dust, the H_α luminosities and equivalent widths would be lowered further. However, the Calcium triplet line equivalent widths would be high due to the presence of Red Supergiant stars in a stellar cluster which is around 10 Myr old.

The high H_α luminosities, $L(H_\alpha) \geq 10^{40}$ erg s $^{-1}$, measured for our sample of starbursts, implies that there is considerable amount of ionizing flux ($Q(H_\alpha) \geq 10^{51}$ photon s $^{-1}$) available in these regions. This would mean that a young starburst of age less than 3 Myr is present, which contains a population of ionizing, massive OB stars. In the absence of contributions from the underlying population, and differential extinction, the observed EW(H_α) would also have been higher due to the presence of this young population. The high values of EW(Ca T) ($> 7\text{Å}$) indicates the presence of evolved massive stars which are in the RSG phase. From the diagnostic diagram using Starburst99 models, we infer that almost all of the starbursts in our sample (except NGC 4984), contain RSGs which have ages of about 6 – 9 Myr. Using the models of Mayya (1997) gives an age of 5–7 Myr for the evolved population. Based on our observations, it appears that most of the starburst nuclei show evidence of a young, ionizing stellar cluster (about 3 Myr old), co-existing with an evolved non-ionizing population (about 6 – 8 Myr old) which results from a previous burst episode.

5.8 Conclusion

In this chapter, we have presented the results obtained from optical to Near – IR spectroscopy of a sample of starburst galaxies. From the optical emission line diagnostics we infer higher electron densities, and higher excitations in starburst nuclei compared to low luminosity HII nuclei. We find through the use of the radiation softness parameter, that the temperatures of ionizing stars decrease with increasing metallicities and is less than 40,000K for all our sample starburst regions. This would place the upper mass limit of the IMF in these regions at $M_u \leq 25 M_\odot$. We find that the low ionization lines are considerably enhanced in these nuclei, which could possibly indicate the presence of shocks or a modification of the thermal properties of the photoionized nebula by dust.

The starburst regions show moderate star formation rates of $0.747 M_\odot \text{ y}^{-1}$ and from a comparison of the SFR in the inner regions with that for the whole galaxy, most of the star formation activity appears to be concentrated in the inner few kiloparsec radius. From $^{12}\text{CO}(1-0)$ measurements available in the literature, it is known that most of these galaxies have huge reservoirs of molecular hydrogen gas concentrated towards the nuclear region, within few hundred parsec radius.

From the observed H_α luminosity, H_α equivalent widths and Ca T equivalent widths, it appears that the nuclear starbursts have a composite population, consisting of young, massive stars which are less than 3 Myr old, co-existing with an evolved population. We have measured the EW(Ca T) in the nuclear regions of starburst galaxies and used these to infer the presence of evolved massive stars which are in the non-ionizing, RSG phase. We use diagnostic diagrams involving EW(Ca T) and EW(H_α), to infer ages of 6–8 Myr for the evolved population.

Bibliography

- [1] Balzano, V.A., 1983, ApJ, 268, 602
- [2] Bica, E., Alloin, D., & Santos Jr., J.F.C., 1990, A&A, 235, 103
- [3] Bresolin, F., Kennicutt, R.C., & Garnett, D.R., 1999, ApJ, 510, 104
- [4] Calzetti, D., Kinney, A.L., & Storchi-Bergmann, T., 1994, ApJ, 429, 582
- [5] Czyzak, S.J., Keyes, C.D., & Aller, L.H., 1986, ApJS, 61, 159
- [6] Devereux, N.A., 1989, ApJ, 346, 126
- [7] Devereux, N.A., & Hameed, S., 1997, AJ, 113, 599
- [8] Devereux, N.A., Taniguchi, Y., Sanders, D.B., Nakai, N., & Young, J. S., 1994, AJ, 107, 2006
- [9] Diaz, A.I., Terlevich, E., & Terlevich, R., 1989, MNRAS, 239, 325
- [10] Forbes, D.A., Boisson, C., & Ward, M.J., 1992, MNRAS, 259, 293
- [11] Garcia - Vargas, M.L., Gonzalez -Delgado, R.M., Perez, E., Alloin, D.M., Diaz, A.I., & Terlevich, E., 1997, ApJ, 478, 112
- [12] Garcia - Vargas, M.L., Molla, M., Bressan, A., 1998, A&AS, 130, 513
- [13] Gonzalez -Delgado, R.M., Perez, E., Diaz, A.I., Garcia - Vargas, M. L., Terlevich, E., & Vilchez, J.M., 1995, ApJ, 439, 604
- [14] Hamuy, M.A., Walker, A.R., Suntzeff, N.B., Gigoux, P., Heathcote, S.R., & Phillips, M.M., 1992, PASP, 104, 533

- [15] Ho, L.C., Filippenko, A.V., & Sargent, W.L.W., 1993, ApJ, 417, 63
- [16] Ho, L.C., Filippenko, A.V., & Sargent, W.L.W., 1997, ApJ, 487, 579
- [17] Jogee, S., 1998, Ph. D Thesis, Yale University
- [18] Jones, J.E., Alloin, D.M., & Jones, B.J.T., 1984, ApJ, 283,457
- [19] Kennicutt, R.C., Keel, W.C., & Blaha, C.C., 1989, AJ, 97, 1022
- [20] Kennicutt, R.C., 1998, ARAA, 36, 189
- [21] Leitherer, C., & Heckman, T.M., 1995, ApJS, 96, 9
- [22] Leitherer, et al., 1999, to appear in ApJS
- [23] Mallik, S.V., 1994, A&AS, 103, 279
- [24] McCall, M.L., Rybski, P.M., & Shields, G.A., 1985, ApJS, 57,1
- [25] Massey, P., Strobel, K., Barnes, J.V., & Anderson, E., 1988, ApJ, 32 8, 315
- [26] Mayya, Y.D., & Prabhu, T.P., 1996, AJ, 111, 1252
- [27] Mayya, Y.D., 1997, ApJ.lett, 482, L149
- [28] Osterbrock, D.E., 1989, The Astrophysics of Gaseous Nebulae and Active Galactic Nuclei (Mill Valley, CA: University Science Books)
- [29] Ravindranath, S., & Prabhu, T.P., 1998, AJ, 115, 2320
- [30] Shields, J.C., & Kennicutt, R.C., 1995, ApJ, 454, 807
- [31] Terlevich, E., Diaz, A.I., & Terlevich, R., 1990, MNRAS, 242, 271
- [32] Terlevich, E., Diaz, A.I., Pastoriza, M.G., Terlevich, R., & Dottori, H., 1990, MNRAS, 242, 48p
- [33] Vilchez, J.M., & Pagel, B.E.J., 1988, MNRAS, 231, 257
- [34] Zaritsky, D., Kennicutt, R.C., & Huchra, J. P., 1994, ApJ, 420, 87

Chapter 6

Summary and prospects

6.1 Overview of results

The results from the present study of a sample of starburst galaxies are summarized in this section. Most of the imaging observations were obtained under non-photometric conditions, and the aperture magnitudes and colors could not be calibrated. Hence, the statistical study of the physical properties of the entire sample of starbursts could not be carried out. Detailed analysis was carried out for NGC 972 and NGC 1365, for which good quality data was available. The spectroscopic data deals generally with emission line ratios and equivalent widths, which are not affected by the non-photometric sky. The spectroscopic data could thus be used for a study of the properties of the entire sample.

6.1.1 Properties of HII regions

A statistical study of HII regions in NGC 1365 was carried out, and the HII region luminosity function (HII LF) and size distribution were obtained (chapter 4). The steep slope of the HII LF and the small “characteristic” diameters for the HII regions in early-type galaxies like NGC 1365, shows that the formation of large star-forming complexes is inhibited in these galaxies. **From the change in slope of the $\log L_{H\alpha}$ versus $\log(D)$ relation, the high luminosity HII regions appear to be density-bounded while**

the low luminosity HII regions are ionization–bounded.

Comparing the physical conditions of the photoionized gas in starbursts and HII nuclei, we find that the electron densities and excitation levels are higher in starbursts (chapter 5). The mean metallicity of starbursts is slightly lower than that of HII nuclei with the mean oxygen abundances being ≈ 1.7 times solar, while in HII nuclei it is twice solar. The ionization parameters derived for starburst nuclei are similar to the values for Seyfert 2 nuclei. We have used the radiation softness parameter to estimate the temperatures of the ionizing stars in five of the sample galaxies, where the NIR [SIII] λ 9069 line could be measured. The absolute values of the temperatures depend on the photoionization models. Through the use of the radiation softness parameter, we find that there is a tendency for the temperatures of ionizing stars to decrease with increasing metallicities and is less than 40,000K for all our starburst nuclei. This would imply an upper mass limit of $M_* \leq 25 M_\odot$ for the IMF in these regions. However, the sample is too small and studies involving larger samples would be required to confirm the trend seen with metallicity and establish the upper mass limit of the IMF in starbursts.

6.1.2 Effects of dust in star–forming regions

Dust associated with star–forming regions can modify the radiation emerging from HII regions significantly. The effects of dust extinction include the reddening of continuum colors, reduction of continuum and emission line luminosities and removal of gas phase coolants from the gas thereby increasing the electron temperatures in the nebula. In chapter 3, we have discussed how the non–uniform dust distribution and the variable dust extinction across the galaxy NGC 972 makes it difficult to correct for the internal reddening. Dereddening the colors using the correction derived from the Balmer decrement over–corrects the colors, making them too blue. Thus it appears that the stellar continuum and the gaseous nebula are not affected by dust to the same extent and the differential extinction depends on the dust geometry. Using photoionization models,

we find that the enhancement in the low-ionization lines in starburst spectra can be explained when the effects of dust are included (chapter 5).

6.1.3 Star formation rates in starbursts

From the H_α luminosities, we derive a mean star formation rate of $0.75 M_\odot \text{ yr}^{-1}$ within the inner 1 kpc radii of starburst galaxies (chapter 5). The star formation rate densities are very high with a mean value of $8.79 M_\odot \text{ yr}^{-1} \text{ kpc}^{-2}$, while for normal spiral disks the SFR densities are $\sim 0.1 M_\odot \text{ yr}^{-1} \text{ kpc}^{-2}$. The SFR mainly depends on the gas density, and CO observations available in literature for some of the galaxies in our sample, do show the presence of high molecular gas densities ~ 1000 to $3500 M_\odot \text{ pc}^{-2}$ within the central 1–2 kpc radii required for such high SFRs.

6.1.4 Stellar populations in starbursts and their ages

From the optical colors and H_α luminosities of the HII regions in NGC 972, we found that the star-formation over the disk of the galaxy is less than 6.5 Myr old (chapter 3). Using the equivalent widths of the H_α emission line and the Ca II triplet absorption lines, we have attempted to study the stellar populations in starburst nuclei and to estimate their ages (chapter 5). The use of the equivalent widths of Ca II triplet lines (Ca T) as a diagnostic for the red supergiant (RSG) stars is discussed. The high H_α luminosities require the presence of a population of young, ionizing stars while the high equivalent widths of the Ca T lines indicate the presence of RSG stars. **Based on the H_α equivalent widths, Ca T absorption line equivalent widths and H_α luminosities, we present evidence for the co-existence of a young population less than 3 Myr old, and an evolved population of red supergiants which are about 6–8 Myr old, in starburst nuclei. The observations seem to agree better with a scenario of successive bursts of star formation rather than continuous star formation.**

6.1.5 Triggers of star formation

In chapter 3, we have presented the H_α image of the IR bright galaxy NGC 972 which shows evidence for a current episode of massive star formation in the disk, and a nucleus that has starburst properties. NGC 972 appears to be an isolated galaxy without any obvious signatures of interaction like tidal tails, or any other morphological distortions and there is no evidence for a bar in the optical images. This prompted us to look at the NIR images which sample the late-type stars better. The K-band image did show a weak bar which lies within the circumnuclear ring. Among isolated galaxies, starbursts are usually associated with strong bars. **Based on the absence of a strong bar, the unusually high molecular gas content, and asymmetry of the spiral arms seen in the NIR images, we suggest that the star formation in NGC 972 may have been triggered by merger with a gas-rich dwarf galaxy.**

6.2 Suggestions for future study

The study of starburst galaxies is one of the most active area of research in extragalactic astronomy. Starburst phenomenon has been found to be very frequent at high redshifts. Hence, it is necessary to understand the nearby starbursts fully in order to be able to interpret the integrated properties of starbursts at high redshifts. Starbursts play an important role in the formation and evolution of galaxies. In this thesis, I have attempted to study the physical conditions of gas in starburst regions, and the star formation histories. In this section a few projects for future work have been suggested which should be carried out using a larger sample of starbursts.

6.2.1 IMF in starburst regions

Even though most of the observations of star-forming regions in the disks of galaxies point towards a universal Salpeter IMF, there have been evidences for a different “top-heavy” IMF in starbursts. Attempts to arrive at the correct IMF by comparing the observed

quantities with that predicted by models, are often affected by the uncertainties in age, metallicities, and the effects of extinction. Hence, while using integrated properties of star-forming regions it is necessary to first identify a parameter that is very sensitive to the IMF. The H_α line equivalent widths are quite sensitive to the upper mass of the IMF (Bresolin & Kennicutt, 1997). Recently Bresolin, Kennicutt and Garnett (1999) have shown that the radiation softness parameter which is not affected by the interstellar reddening, can be used as an indicator of the effective temperatures of the ionizing stars. They find that the mean stellar temperatures of the ionizing stars decrease with increasing metallicity. The determination of the radiation softness parameter through optical-NIR spectroscopy for a large sample of starbursts would help to understand the metallicity dependence of the stellar effective temperatures. In other words, this probes the dependence of the upper mass limit of the IMF on metallicity. The actual values of the temperatures and the corresponding masses can be determined using photoionization models, and stellar atmosphere and evolution models. In chapter 5, we have presented the radiation softness parameters measured for five of our sample starbursts and a larger sample needs to be studied to ascertain the trends with metallicity.

6.2.2 Determination of SFRs

In this thesis, we have mainly relied on the use of the H_α emission line luminosity as an indicator of the SFR in star-forming regions. The main disadvantage of using the H_α line is that it is severely affected by extinction and also provides the SFR only for stars with masses $\geq 10M_\odot$. The SFR for the low mass stars needs to be determined by some other method. Another problem with using the recombination lines to determine the SFR, is the inability to account for the ionizing photons that escape from the HII regions. However, the effects of dust extinction can be reduced considerably by using the recombination lines in the NIR. Thus, for starburst regions which are known to suffer heavy extinction, the $Br\gamma$ ($2.16 \mu\text{m}$) recombination line would give a better estimate of the SFR.

6.2.3 Triggers of nuclear activity

Observations show that nuclear activity (starbursts and AGNs) is more common in interacting galaxies and barred galaxies. However, there are many cases where isolated, non-barred galaxies show nuclear activity. Another related problem is the role of starbursts in fueling active galactic nuclei (AGNs). In recent years, there has been increasing observational evidence for the co-existence of circumnuclear starbursts and low-luminosity AGNs like Seyferts and LINERS in the nuclear regions of galaxies. Since gas is efficiently converted to stars in starbursts, and massive stars return most of their material back into the ISM through stellar winds and supernovae in a short time, they can act as very good gas reservoirs to sustain AGN activity. Theoretical models have shown that gas from the outer regions of the galaxy, can be brought to the inner regions, if it loses angular momentum via shocks at the bar ends, galaxy interactions or cloud-cloud collisions. This gas tends to accumulate at the Inner Lindblad Resonances (ILRs), and it often coincides with the observed location of circumnuclear star forming rings. These rings usually occur at a radius of few hundred parsecs to about 1 kiloparsec. But nuclear starbursts and AGN activity require that the gas be brought to the central few parsecs. Bars and spirals originating within the ILRs can transport gas right into the nuclear regions (Shlosman 1994). Interestingly, recent studies involving optical and NIR imaging of the central regions of galaxies, have revealed bars originating within the circumnuclear regions and extending all the way to the inner few parsecs (Colina *et al.*, 1997; Knapen *et al.* 1995; Ryder & Knapen 1999). NIR images sample the underlying population consisting of late-type stars, red giant and supergiant populations much better, and are very useful for revealing the actual morphological type of the galaxy, presence of bars, evolved stages of starbursts, etc (chapter 3). Thus NIR imaging of a sample of galaxies showing circumnuclear star formation, with and without a nuclear activity would hold a clue to the mass-transfer induced activity at galaxy centers.

Bibliography

- [1] Bresolin, F., & Kennicutt, R.C., 1997, *AJ*, 113, 975
- [2] Bresolin, F., Kennicutt, R.C., & Garnett, D.R., 1999, *ApJ*, 510, 104
- [3] *Mass-transfer induced activity in galaxies*, 1994, edited by Issac Shlosman, Cambridge University press.
- [4] Colina, L., *et al.*, 1997, *ApJ. lett*, 484, L41
- [5] Knapen, J.H., *et al.*, 1995, *ApJ. lett*, 443, L73
- [6] Ryder, S.D., & Knapen, J.H., 1999, *MNRAS*, 302, L7

List of publications

- Massive star formation in the Infrared–bright galaxy NGC 972
Swara Ravindranath and Tushar P. Prabhu, *Astronomical Journal*, 1998, 115, 2320-2330.
- Near Infrared and Optical morphology of the dusty galaxy NGC 972
Y. D. Mayya, Swara Ravindranath and L. Carrasco, *Astronomical Journal*, 1998, 116, 1671-1678.
- Properties of HII regions in NGC 1365 – The luminosity function and size distribution
Swara Ravindranath and Tushar P. Prabhu, 1999, (*To appear in "The Evolution of Galaxies on Cosmological Timescales", Euroconference proceedings, Nov. 30 - Dec5, 1998, Puerto de la Cruz (Spain)*)
- The emission line spectra and stellar populations of Starburst galaxies
Swara Ravindranath and Tushar P. Prabhu, 1999, (*To appear in "The Evolution of Galaxies on Cosmological Timescales", Euroconference proceedings, Nov. 30 - Dec5, 1998, Puerto de la Cruz (Spain)*)